Application of Phase Imaging at High Field MR Thermometry at 7 Tesla

Von der Fakultät für Physik und Geowissenschaften

der Universität Leipzig

genehmigte

DISSERTATION

zur Erlangung des akademischen Grades

doctor rerum naturalium

Dr. rer. nat.

vorgelegt

von Diplom-Physiker Markus Nikola Oliver Streicher

geboren am 25. Februar 1980 in Ravensburg

Gutachter: Prof. Dr. Robert Turner
Prof. Dr. Andrew G. Webb

Tag der Verleihung 26. Februar 2018

Universität Leipzig

Fakultät für Physik und Geowissenschaften

Max-Planck-Institut

für

Kognitions- und Neurowissenschaften

MAX-PLANCK-GESELLSCHAFT

To my parents
for all their love and support

Bibliographische Beschreibung:

Streicher, Markus
Application of Phase Imaging at High Field - MR Thermometry at 7 Tesla
Universität Leipzig, Dissertation
152 Seiten, 260 Literaturangaben, 58 Abbildungen, 9 Tabellen

Referat:

The main purpose of this research was to develop improved methods for RF coil characterisation, and for non-invasive spatio-temporal mapping of temperature in the living body, in order to utilise the full potential of magnetic resonance imaging (MRI) at high magnetic fields by ensuring radiofrequency (RF) safety. Current RF power limits are often overly conservative, unnecessarily limiting the full potential of MRI, especially at high field. Thus it is useful to monitor tissue temperature while running MR imaging sequences which may deposit high RF power.

Proton resonance frequency (PRF) MR thermometry can employ the phase of the complex MR signal to estimate temperature change over time. However, the shift of the water PRF with temperature is relatively small, making phase-based MR thermometry inherently sensitive to any extraneously caused changes of local frequency or MR phase. A potential source of error to PRF MR thermometry is a change in surround air susceptibility.

The considerable impact of air susceptibility changes on PRF MR thermometry was demonstrated and quantified in experiments and magnetic field simulations. One way of correcting MR thermometry is to use a chemically shifted reference substance, in combination with a phase-sensitive chemical shift-selective MR thermometry sequence. The requirement of having a reliable separation of substances based on their resonance frequency was met by a novel frequency-selective phase-sensitive spin-echo (SE) MR thermometry sequence. This sequence was thoroughly tested in phantom and in-vivo experiments as well as in extensive Bloch simulations. The sequence limitations and advantages are discussed in detail. This technique acquires unsaturated water and fat images in rapid succession at the same position in space. The acquisition of a water and fat slice in less than 100 ms allows the correction of rapid field fluctuations in the brain caused by breathing and heartbeat, while still ensuring the correction of long term drift. With no assumptions required regarding temperature distribution in the tissue, this novel MR thermometry technique can measure brain temperature within a single $(1.5\ \mathrm{mm})^3$ voxel with a very low standard deviation (SD) of 0.3 K. Using an MRI phantom with a dimethyl sulfoxide reference, heating experiments achieved a MR temperature measurement with an SD of approximately 0.1 K in a single $(1.5\ \mathrm{mm})^3$ voxel. In conclusion, the work presented in this thesis assists the development of a real-time in-vivo temperature monitoring system that guarantees patient RF safety at high field.

Contents

List of Figures

List of Tables

Glossary

Abbreviation	Name
AFI	actual flip angle imaging
ASE	asymmetric spin-echo
ASL	arterial spin labeling
BOLD	blood oxygen level dependent
BW	bandwidth
CNR	contrast-to-noise ratio
CSF	cerebrospinal fluid
DMSO	dimethyl sulfoxide
EPI	echo planar imaging
FA	flip angle
FLASH	fast low-angle shot
FOV	field of view
FWHM	full width half maximum
fMRI	functional magnetic resonance imaging
GE	gradient-echo
GLM	general linear model
GM	gray matter
GR SE	gradient reversal frequency-selective spin-echo technique
GRE	gradient-recalled echo
GRAPPA	generalized autocalibrating partially parallel acquisitions
IV SE	Ivanov method, frequency-selective spin-echo technique
k	wave vector
MR	magnetic resonance
MRI	magnetic resonance imaging
NMR	nuclear magnetic resonance
P	bandwidth-time product
PET	positron emission tomography
PRF	proton resonance frequency
PSF	point spread function
RF	radiofrequency
ROI	region of interest
SAR	specific absorption rate
SE	spin-echo
SNR	signal-to-noise ratio
SD	standard deviation
TE	echo time
TE_{eff}	effective echo time
TR	repetition time
WM	white matter

Chapter 1

Introduction

During the last decades, magnetic resonance imaging (MRI) has rapidly become a valuable tool in medical imaging. MRI is non-invasive, does not involve ionizing radiation and has excellent soft-tissue contrast. Particularly impressive, MRI can generate a multitude of different contrasts ranging from various anatomical contrasts to functional imaging, metabolic studies and even temperature measurements. However, a main drawback of MRI are the long scan times and associated with this the relative poor signal-to-noise ratio (SNR). The relative poor SNR is because only a tiny part of the nuclei contribute to the measured MR signal. At 7 Tesla and body temperature, it is only 46 in one million hydrogen nuclei that do contribute.

SNR increases approximately linearly with the magnetic field,[1] therefore, the drive to higher magnetic fields of 7 T, 9.4 T or even higher (Budinger and Bird, 2017; Fiedler et al., 2017; Haacke et al., 1999).[2] Despite these and other potential advantages of scanning at high magnetic fields, there are a number of challenges that have to be overcome to utilise the full potential of 7 T and higher, e.g. the design of the superconducting magnet or B_0 field inhomogeneities.

Probably the most serious safety risk in human MRI is related to the increase in power of the radiofrequency (RF) pulses at high field. The time-varying magnetic field B_1^+, at or very close to the Larmor frequency of the nuclei of interest, is needed to manipulate the nuclear spin magnetisation. This desired time-varying B_1^+ field, however, is accompanied by induced electric fields which lead to power absorption in conductive tissue.[3] The deposited RF energy leads to tissue heating and, if not controlled, can result in tissue damage. The power absorption increases quite rapidly with frequency and, therefore, B_0 field strength. By Faraday's law, the induced E-fields increase linearly with frequency for a given B_1^+ field and according to

[1] SNR can also be increased by lowering the temperature of the sample and the receive RF-coils and electronics.

[2] There are also additional advantages of higher magnetic fields, for example functional MRI (fMRI) where signal contrast increases more than linear or in blood-oxygen-level dependent (BOLD) fMRI where spatial specificity with respect to neural activity improves or in arterial spin labelling (ASL) techniques which profit from a longer T_1 of blood (Gardener et al., 2009; Ivanov et al., 2017; Turner et al., 1993; Uludağ et al., 2009; Yacoub et al., 2003).

[3] For more details on RF Heating and SAR see Section 2.6.

Ohm's law, the absorbed power, therefore, increases quadratically with field strength, assuming a constant conductivity.[4] However, the conductivity of human tissue is not constant and increases with frequency,[5] additionally elevating the absorbed power.[6] Accompanying the frequency increase is the decrease in RF wavelength, reaching approximately 12-15 cm at 7 T. This leads to stronger interferences and therefore to a more inhomogeneous B_1 and E-fields, further increasing the absorbed power in some parts of the imaged tissue and decreasing it in others.[7]

Regulations require that the increase in temperature of tissue exposed to RF fields should remain below 1 K in the head (International Electrotechnical Commission, 2008). Since for many MRI sequences the allowed transmitted power is already reached at 3 T, it is evident that it presents a significant challenge at 7 T and higher. The corresponding power limit is set for each RF coil based on RF simulations, neglecting realistic blood perfusion and including a considerable safety margin (Collins et al., 2004b; Vaughan, 2006). It is, therefore, likely that current RF power limits are often overly conservative, unnecessarily limiting the full potential of MRI especially at high field. Thus, it would be very helpful to be able to monitor the tissue temperature while running the high RF power MR sequence of interest. This work attempts a step towards real-time tissue temperature monitoring by MR thermometry to optimise power deposition and thus SNR (described in Chapter 5).[8]

It has often been remarked that water is a highly unusual liquid (Turner and Streicher, 2012). Apart from being very abundant and liquid at average Earth planetary temperature, it has an exceptionally high specific heat and latent heats of transition, its molecules are polar, it has strong optical absorption at infra-red and ultra-violet frequencies, and it exhibits hydrogen bonding. Almost all these unusual properties are related to the fact that the H_2O molecule is polar and not straight, with a hydrogen atom on either side of the oxygen atom, but in its ground state of energy, it is bent, with an angle of about 105° between the two bonds (Hoy and Bunker, 1979; Levitt, 2001). This mere fact also has an important effect on the Larmor resonance frequency of the protons that constitute the hydrogen nuclei. If a magnetic field is externally applied to water, its protons experience a resultant magnetic field, the sum of the external field and the shielding field arising mainly from the response of the molecule's mobile electrons. Each proton's resonant frequency is

[4]The linear increase of the induce E-fields with increasing frequency only holds for a constant B_1^+ field distribution. However, the assumption of a constant B_1^+ field distribution becomes less and less valid as the RF frequency increases, leading to a less than linear increase of induced E-fields with frequency (Collins and Smith, 2001).

[5]In fact, the conductivity of many common substances and tissue increases with frequency (Kremer and Schönhals, 2003).

[6]See Section 2.5.3 on the dielectric properties of body tissue.

[7]The described effects are a worst case estimate of SAR, for more realistic estimations of SAR see Collins and Smith and Fiedler et al. (Collins and Smith, 2001; Collins and Wang, 2011; Fiedler et al., 2017).

[8]Besides, MR thermometry was applied to phantom measurements for verification and RF coil characterisation.

determined by this net magnetic field through the Larmor equation. Hydrogen bonds between neighboring molecules distort the electronic configuration of the molecules and reduce the electronic screening of the hydrogen proton. The fraction and nature of hydrogen bonds change with temperature, and on average, the water molecules spend less time in the hydrogen-bonded state as temperature increases. As a result, the electronic screening increases, and hence, the resultant magnetic field experienced by the hydrogen proton is decreased, leading to a decrease in Larmor frequency with increasing temperature (Hindman, 1966). This has been found to be linear over a usefully broad temperature range, giving rise to the proton resonance frequency (PRF) method for nuclear magnetic resonance (NMR) thermometry (Quesson et al., 2000; Rieke and Butts-Pauly, 2008b). A remarkable opportunity arises for uniquely non-invasive and accurate temperature measurements deep within any water-containing object since the shift in PRF is easily measurable using relatively simple MRI techniques. In this work, MR thermometry was done using the PRF shift of water with temperature.

PRF MR thermometry often employs the phase of the complex MR water proton signal (Rieke and Butts-Pauly, 2008b). The temperature sensitivity of phase MR thermometry originates from the cumulative phase shift of the magnetisation for off-resonance water protons over time before the data acquisition. The shift with temperature is small (-0.01 ppm/K), and makes the method inherently sensitive to any additional causes of local frequency change, which if uncorrected, lead to errors in temperature estimates (Grissom et al., 2010a; Seifert et al., 2007). Sources of error are, for example, magnetic field drift (Foerster et al., 2005), tissue movement (Maier et al., 2012; Peters et al., 2009; van Gelderen et al., 2007) or as described in Chapter 4 susceptibility changes (Baron et al., 2014a; Kickhefel et al., 2012; Raj et al., 2000; Sprinkhuizen et al., 2010b; Streicher et al., 2012; van Gelderen et al., 2007). In this thesis air susceptibility change as a source of error to PRF shift MR thermometry is discussed in detail (Chapter 4).

In general, there are two approaches to correct PRF MR phase thermometry measurements.

The first type of these approaches are the reference-free approaches, which do not rely on a reference image acquired before heating (Grissom et al., 2010b; Kuroda et al., 2006; Rieke et al., 2004; Salomir et al., 2012). Instead, these methods require part of the water proton image to be unheated, or at least to be of known temperature. The MR background phase of the region of known temperature is then extrapolated into the region of unknown temperature change.

The second type of approaches uses a reference substance to correct MR thermometry. These approaches use a reference substance that has a PRF independent of temperature, or with a different thermal coefficient than water. This enables correction of the temperature maps using a magnetic field map of the reference substance. In this work, fat and dimethyl sulfoxide were used as reference substances. The temperature maps can also be corrected using inserted thermometers. For

referenced PRF thermometry, the water and a reference signal need to be acquired simultaneously, as with a multi echo gradient echo acquisition, or closely in time by suppression or inversion of the unwanted signal (de Senneville et al., 2010; Kuroda et al., 1997; Sprinkhuizen et al., 2010a; Taylor et al., 2008). Independent of what phase imaging and correction technique is used, it is important that chemical shift selectivity is high; meaning that a minimum of the unwanted signal (e.g., fat in the water image) contributes to the chemical species of interest. If not completely suppressed, residual signal can corrupt the phase of the imaged species and thus confound the temperature measurement (Rieke and Butts-Pauly, 2008a).

In Chapter 5 a novel frequency-selective SE technique is presented and evaluated that reliably suppresses the unwanted signal and allows precise and fast referenced MR thermometry in phantoms and in-vivo. This approach could be a step in the direction of real-time SAR monitoring due to its high speed and, more importantly, considerably reduced sensitivity to physiologically related fluctuations. With no assumptions required regarding the temperature distribution in the tissue, the approach can provide a single voxel standard deviation of 0.3 K in the brain (Streicher et al., 2014).

Chapter 2

Background

The most abundant elements in the human body are hydrogen, oxygen and carbon with number percentages of approximately 62 %, 24 % and 12 %, respectively. The main isotopes of oxygen, ^{16}O, and carbon, ^{12}C, have nuclear spin $s = 0$ in their ground nuclear state and are therefore NMR silent (Levitt, 2001). So it is fortunate that the main isotope of hydrogen, ^{1}H, contains a single proton with spin $S = 1/2$. Most of the hydrogen is found in water, making up 50-60 % of the human body mass and the rest of the hydrogen protons are mainly bound in lipids and proteins. Here the hydrogen spin dynamics in water and fat MRI, relevant to this thesis are introduced.

2.1 Nuclear Magnetic Resonance

2.1.1 Nuclear Spins in a Magnetic Field

The proton and all other elementary or composed particles have the quantum mechanical property called spin, an intrinsic form of angular momentum. The spin s can take on positive half-integer values, 0, 1/2, 1, 3/2, 2, ... including zero. The total angular momentum S measured along any direction S_i is quantized and can adopt the following values:

$$S = \hbar\sqrt{s\,(s+1)} \tag{2.1}$$

$$\boldsymbol{S_i} = \hbar \cdot \boldsymbol{s_i}, \quad s_i \in \{-s,\, -s+1,\, \ldots,\, s-1,\, s\} \tag{2.2}$$

where s_i is the spin projection quantum number along any axis i and $\hbar$ the reduced Planck constant $\hbar = \frac{h}{2\pi} = \frac{6.626 \cdot 10^{-34}\text{Js}}{2\pi}$.

The spin angular momentum S is associated with a magnetic moment μ by

$$\mu = \gamma \cdot S \tag{2.3}$$

$$\boldsymbol{\mu_i} = \gamma \cdot \boldsymbol{S_i} = \gamma \cdot \hbar \cdot \boldsymbol{s_i} \tag{2.4}$$

where γ is the particle dependent gyromagnetic ratio. For the hydrogen nucleus, a

proton, the gyromagnetic ratio is $\gamma = 2.675 \cdot 10^8 \frac{\text{rad}}{\text{s}\cdot\text{T}}$ and $\frac{\gamma}{2\pi} = 42.576 \cdot 10^6\,\text{Hz/T}$. The energy of a magnetic moment μ in a magnetic field B_0 is given by

$$E = -\boldsymbol{\mu} \cdot \boldsymbol{B_0} \tag{2.5}$$

The proton has spin $S = 1/2$ and therefore the energy difference between the two states is given by:

$$\Delta E = -\gamma \cdot \hbar \left(-\frac{1}{2} - \frac{1}{2}\right) \cdot B_0 = \hbar \cdot \gamma \cdot B_0 = \hbar \cdot \omega_0 \tag{2.6}$$

$$\Longrightarrow \quad |\gamma \cdot B_0| = |\omega_0| \tag{2.7}$$

The frequency ω_0 in Equation 2.7 associated with the emission or absorption of a quantum of energy (e.i. a photon) is the Larmor precession frequency (Haacke et al., 1999).[1,2] These two states, so-called eigenstates, form a basis for all possible spin states which point in any arbitrary direction and precess around B_0, as shown in Figure 2.1 A. The random distribution of spin directions is slightly altered by the

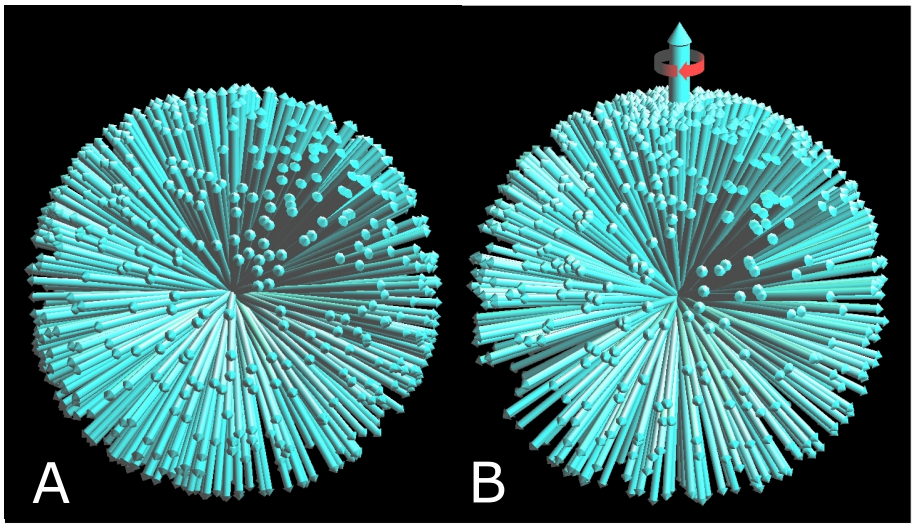

Figure 2.1: *Spin distribution for a large number of protons. (A) Random proton spin distribution in the absence of a magnetic field. (B) Spin distribution with a magnetic field B_0 pointing upward. The spin distribution is precessing around B_0 with the Larmor frequency (see Eq. 2.19). Spin orientation is still random with the longitudinal net magnetisation along B_0 gradually developing. Image from Hanson 2008.*

magnetic field with an increased probability to point in the direction of B_0, such that a net magnetisation M forms (as in Fig. 2.1 B).[3] The net magnetisation forms

[1]This does not mean that photons are detected in MRI. For more information on the induced NMR signal and virtual photons see Hoult and Bhakar (Hoult and Bhakar, 1997).

[2]Equation 2.7 gives just the magnitude of the Larmor precession frequency. In fact, $\boldsymbol{B_0}$ and $\boldsymbol{\omega_0}$ are pointing in opposite directions, i.e. $\boldsymbol{\omega_0} = -\gamma \cdot \boldsymbol{B_0}$ (see Eq. 2.19).

[3]In MRI, where a large number of protons are considered, the measurement process does not perturb the system in such a way that the protons are brought into their eigenstates. In contrast

by T_1-relaxation and approaches the equilibrium value M_0 (for more details see Section 2.1.4).[4] The longitudinal nuclear spin magnetisation is almost undetectable. It is about four orders of magnitude smaller than the typical diamagnetism of the sample, which is associated with the electrons. NMR and MRI take a different approach and do not measure the nuclear spin magnetisation along the field. Instead the longitudinal magnetisation is manipulated in such a way that it can be measured perpendicular to the main magnetic field (Levitt, 2001).

2.1.2 Macroscopic Magnetisation in a Magnetic Field

It was shown by Feynman et al. (1957) that the behaviour of an ensemble of two quantum-level, non-interacting systems under the influence of a perturbation can be described by classical mechanics (Bloch, 1946). This applies to magnetic resonance such that the behaviour of the resulting magnetisation vector $\boldsymbol{M}$ can be described by a magnetic dipole with spin angular momentum in a magnetic field. For the torque N on a magnetic dipole μ in an external magnetic field and the change of the angular momentum L due to a torque holds:

$$\boldsymbol{N} = \boldsymbol{\mu} \times \boldsymbol{B} \quad \text{and} \quad \frac{d\boldsymbol{L}}{dt} = \boldsymbol{N} \tag{2.8}$$

Combining Equation 2.3 relating the magnetic dipole moment with the spin angular momentum and Equations 2.8 results in the equation of motion for the net magnetisation (Haacke et al., 1999; Hanson, 2008; Levitt, 2001):[5]

$$\frac{\partial \langle \boldsymbol{\mu} \rangle}{\partial t} = \gamma \langle \boldsymbol{\mu} \rangle \times \boldsymbol{B} \quad \Longrightarrow \quad \frac{\partial \boldsymbol{M}}{\partial t} = \gamma \boldsymbol{M} \times \boldsymbol{B} \tag{2.9}$$

In a static magnetic field this results in a constant left-handed precession of the spin distribution and the net magnetisation $\boldsymbol{M}$ about the $\boldsymbol{B_0}$ field axis independent of the direction of $\boldsymbol{M}$.[6]

2.1.3 Magnetisation in an RF Field

In order to prepare the magnetisation for signal generation a second oscillating magnetic field $\boldsymbol{B_1}$ perpendicular to $\boldsymbol{B_0}$ is applied. The $\boldsymbol{B_1}$ field is also called RF field, since the oscillation of the field is normally close or at the Larmor frequency (see Section 2.1.1) of the nuclei of interest, which is in the RF frequency range.

---

to the Stern-Gerlach experiment, where single spin particles (originally silver atoms) are travelling through an inhomogeneous magnetic field (Gerlach and Stern, 1922; Hanson, 2008).

[4] The magnetisation equilibrium value M_0 depends on the magnetic field strength B_0, temperature, spin density and is determined by the Boltzmann distribution (Haacke et al., 1999; Hanson, 2008).

[5] Relaxation processes caused by interactions of the spins with the surrounding are an important correction to this equation.

[6] The precession frequency can be derived by solving the differential Equation 2.9 or with the help of the rotating frame, discussed in Section 2.1.3 and resulting in Equation 2.19.

To determine the effect of both fields on the magnetisation it is helpful to consider a rotating frame of reference (Haacke et al., 1999). For the magnetisation the basic kinematic equation holds:

$$\frac{d\boldsymbol{M}}{dt} = \left(\frac{d\boldsymbol{M}}{dt}\right)_{rot} + \boldsymbol{\Omega} \times \boldsymbol{M} \tag{2.10}$$

This equation relates the time derivative of the magnetisation in the stationary and rotating frame. $\boldsymbol{\Omega}$ is the angular velocity of the rotating frame of reference. Substituting Equation 2.9 into Equation 2.10 and solving for the derivative of the magnetisation in the rotation reference frame gives:

$$\left(\frac{d\boldsymbol{M}}{dt}\right)_{rot} = \frac{d\boldsymbol{M}}{dt} - \boldsymbol{\Omega} \times \boldsymbol{M} = \gamma \boldsymbol{M} \times \boldsymbol{B} + \boldsymbol{M} \times \boldsymbol{\Omega} \tag{2.11}$$

$$= \gamma \boldsymbol{M} \times \left(\boldsymbol{B} + \frac{\boldsymbol{\Omega}}{\gamma}\right) \tag{2.12}$$

Defining the effective magnetic field $\boldsymbol{B_{eff}}$ in the rotating frame as:

$$\boldsymbol{B_{eff}} = \boldsymbol{B} + \frac{\boldsymbol{\Omega}}{\gamma} \tag{2.13}$$

results in a behaviour of the magnetisation in the rotating frame:

$$\left(\frac{d\boldsymbol{M}}{dt}\right)_{rot} = \gamma \boldsymbol{M} \times \boldsymbol{B_{eff}}. \tag{2.14}$$

similar to Equation 2.9 for the stationary frame. The effective magnetic field $\boldsymbol{B_{eff}} = \boldsymbol{B} + \boldsymbol{\Omega}/\gamma$ (Eq. 2.13) is a superposition of all external fields $\boldsymbol{B}$ and an imaginary magnetic field with magnitude $|\Omega|/\gamma$ and direction parallel to the axis of rotation of the rotating reference frame.

Without loss of generality and by convention the main magnetic field $\boldsymbol{B_0}$ is pointing along the z-direction. The $\boldsymbol{B_1}$ field is perpendicular to the main magnetic field and oscillates in the x-y plane with frequency ω_{RF} and phase φ.[7] $\boldsymbol{B_1}$ in the stationary and rotating frame of reference is given by:[8]

$$\text{stationary: } \boldsymbol{B_1} = \begin{pmatrix} B_1 \cos(\omega_{RF} t + \varphi) \\ B_1 \sin(\omega_{RF} t + \varphi) \\ 0 \end{pmatrix} \text{ and rotating: } (\boldsymbol{B_1})_{rot} = \begin{pmatrix} B_1 \cos(\omega_{RF} t - \Omega t + \varphi) \\ B_1 \sin(\omega_{RF} t - \Omega t + \varphi) \\ 0 \end{pmatrix} \tag{2.15}$$

[7] In conventional MRI only $\boldsymbol{B_1}$ fields that are perpendicular to $\boldsymbol{B_0}$ are useful to manipulate the magnetisation. Furthermore, in conventional MRI the $\boldsymbol{B_1}$ field most likely has a small and unwanted component parallel to $\boldsymbol{B_0}$, but this component is not useful to manipulate the magnetisation.

[8] A circular polarized $\boldsymbol{B_1}$ field is assumed. A similar derivation holds for the less efficient linearly polarized RF field. Circular polarized RF fields are most efficient in manipulating the net magnetisation based on the transmitted RF power (for more details see Section 2.6 on RF heating). In real MRI applications RF fields are elliptically polarized and can be viewed as a superposition of inefficient linearly and efficient circularly polarized RF fields.

Therefore $\boldsymbol{B_{eff}}$ in the rotating reference frame is:[9]

$$\boldsymbol{B_{eff}} = \boldsymbol{B_0} + (\boldsymbol{B_1})_{rot} + \frac{\boldsymbol{\Omega}}{\gamma} = \begin{pmatrix} B_1 \cos(\omega_{RF} t - \Omega t + \varphi) \\ B_1 \sin(\omega_{RF} t - \Omega t + \varphi) \\ B_0 + \frac{\Omega}{\gamma} \end{pmatrix} \tag{2.16}$$

Choosing $\boldsymbol{\Omega} = \boldsymbol{\omega_0} = -\gamma \boldsymbol{B_0}$, then the magnetisation in the rotating reference frame is not affected by the static magnetic field in z-direction and only $(\boldsymbol{B_1})_{rot}$ remains. Setting the $\boldsymbol{B_1}$ frequency $\omega_{RF} = \Omega = -\gamma B_0$ defines the on-resonance condition in which only a stationary component of $\boldsymbol{B_{eff}}$ in the x-y plane remains. On-resonant:

$$\boldsymbol{B_{eff}} = \begin{pmatrix} B_1 \cos\varphi \\ B_1 \sin\varphi \\ 0 \end{pmatrix} \quad \Longrightarrow \quad \left(\frac{d\boldsymbol{M}}{dt}\right)_{rot} = \gamma \boldsymbol{M} \times \begin{pmatrix} B_1 \cos\varphi \\ B_1 \sin\varphi \\ 0 \end{pmatrix} \tag{2.17}$$

$$\left(\frac{d\boldsymbol{M}}{dt}\right)_{rot} = \gamma \boldsymbol{M} \times (\boldsymbol{B_1})_{rot} \tag{2.18}$$

For this condition it is apparent that the RF field causes the magnetisation to precess only around $(\boldsymbol{B_1})_{rot}$. This precession about B_1 in the rotating frame is also described by Equation 2.9 by substituting $\boldsymbol{B}$ with the B_1 field in the rotating frame. The action of a B_1 field on the spin distribution is visualized in Figure 2.2.

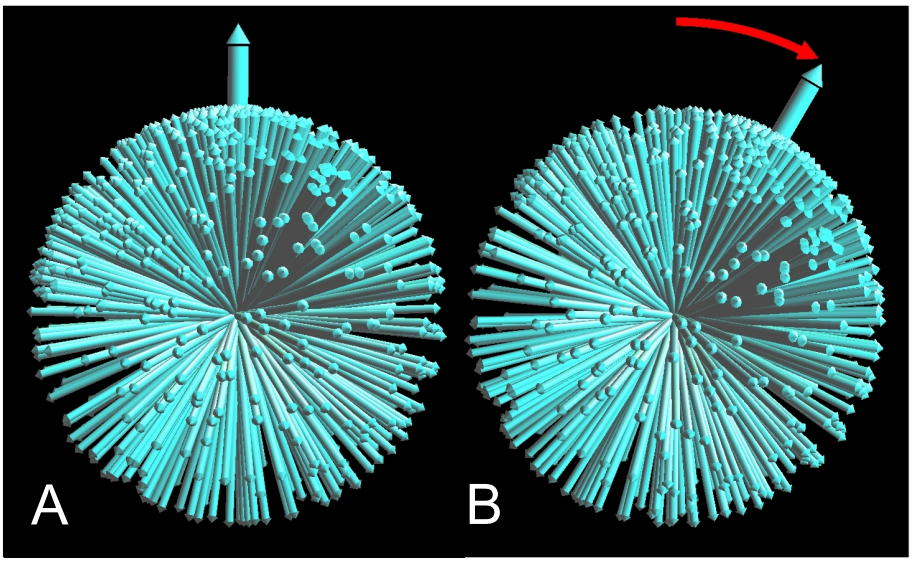

Figure 2.2: *The equilibrium spin distribution is rotated by an on-resonant RF field. (A) The spin distribution is in a magnetic field B_0 pointing upwards and a net magnetisation has developed. In the on-resonant rotating frame of reference ($\Omega = -\gamma B_0$) this distribution is stationary. (B) A circularly polarized on-resonant RF field perpendicular to B_0 is also stationary in the rotating frame. Assuming the stationary B_1 vector to point out of the page, this would cause the whole spin distribution to rotate as indicated by the red arrow. Image from Hanson 2008.*

[9] Since $\boldsymbol{B_0}$ is parallel to $\boldsymbol{\Omega}$, $\boldsymbol{B_0} = (\boldsymbol{B_0})_{rot}$.

Using the on-resonant condition and setting $\boldsymbol{B_1} = 0$ the frequency of precession of $\boldsymbol{M}$ about $\boldsymbol{B_0}$ can easily be derived in the rotating frame. In this rotating frame $\frac{\partial \boldsymbol{M}}{\partial t} = 0$, i.e. the magnetisation $\boldsymbol{M}$ is not moving and therefore the frequency of precession in the stationary frame is:

$$\boldsymbol{\omega_0} = -\gamma \boldsymbol{B_0}. \tag{2.19}$$

This equation applies in general for any magnetic field $\boldsymbol{B}$.

By applying $\boldsymbol{B_1}$ for a short period of time with appropriate frequency and phase the net magnetisation can be made to move from any arbitrary direction to any other arbitrary direction. The angle between original and final direction is called the flip angle. For on-resonant RF pulses the flip angle θ is:[10]

$$\theta = \int_0^\tau \omega\,(t)\,dt = -\gamma \int_0^\tau B_1\,(t)\,dt \tag{2.20}$$

for a RF pulse duration τ, using Equation 2.19. After the RF pulse the magnetisation precesses around $\boldsymbol{B_0}$ in the stationary frame as described in Section 2.1.2. The equilibrium magnetisation $\boldsymbol{M_0}$ is characterised by a random distribution of spin directions with only a slightly increased probability to point along $\boldsymbol{B_0}$ (see Fig. 2.1). Still, the state when the net magnetisation has a component in the transverse plane is called a coherent or phase coherent state. In order to obtain a persistent rotating component of the net magnetisation $\boldsymbol{M}$ in the transverse plane it is essential that the spin system forms a coherent mixture of states, i.e. that the relative phases of the different states do not undergo any rapid changes (Bloch, 1946).

For the on-resonant condition a narrow frequency band around $\omega_0 = -\gamma B_0$ can be made to achieve a similar flip angle and phase by modulating the B_1 amplitude. When simultaneously a magnetic field gradient is applied the narrow frequency band can be translated to a narrow slice in space for which the on-resonant condition holds (see also Section 2.2.1 on magnetic field gradients). In this way the magnetisation of only a thin slice, perpendicular to the magnetic field gradient, is manipulated by the on-resonant RF pulse while the surrounding magnetisation is not considerably affected. These RF pulses are called slice-selective. The slice-selective pulses used in this work are truncated sinc-like pulses that are designed to excite, invert or refocus a narrow frequency band (Bernstein et al., 2004).[11] In Figure 2.17 A-C on page 69 the excitation RF pulse flips a frequency range of ± 250 Hz by approximately 90°.

[10] Adiabatic pulses sweep through a relatively large frequency range and do not obey the conventional relationship between the flip angle and the B_1 amplitude described in Equation 2.20 (Bernstein et al., 2004).

[11] Optimized pulse design methods to achieve desired slice profiles are normally used. The probably most prominent method is the Shinnar-Le Roux algorithm (Pauly et al., 1991; Shinnar et al., 1989).

2.1.4 Bloch Equations and Relaxation

Up to now the response of a large number of isolated spins in an external magnetic field has been described. Interactions of the spins with the surrounding lead to important modifications to this behaviour. The Bloch equations provide a general semiclassical framework for treating the simultaneous effects of relaxation, RF fields, and resonance offset for an isolated spin-1/2 ensemble (Bloch, 1946; Bloch et al., 1946; Levitt, 2001).[12] The return of the magnetisation to its equilibrium value $\boldsymbol{M_0}$ along the z-direction after some perturbation can be described by two relaxation processes. These two relaxation processes were introduced by Bloch in 1946 and are characterised by their corresponding time constants T_1 and T_2. These relaxation time constants are strongly dependent on tissue properties and are the basis for many of the image contrasts in MRI (Haacke et al., 1999).

The first relaxation process describes the return of the net magnetisation to the equilibrium Boltzmann distribution (Hanson, 2008). This process is called longitudinal relaxation or spin-lattice relaxation, since the energy of the spin system dissipates via the crystal lattice, while internuclear interactions leave this energy unchanged (Bloch, 1946). Bloch described the spin-lattice relaxation rate of change with

$$\frac{dM_z(t)}{dt} = \frac{M_0 - M_z(t)}{T_1} \tag{2.21}$$

such that

$$M_z(t) = M_0 - (M_0 - M_z(0))\, e^{-\frac{t}{T_1}} \tag{2.22}$$

with the spin-lattice relaxation time constant T_1.

The second relaxation process describes the decay of the precessing transverse magnetisation. The net magnetisation in the transverse plane is mainly lost due to spin-spin interactions.[13] Characterised by the decay time T_2. The precessing nuclear magnetic moments cause a locally varying magnetic field in which the nuclear spins precess at different rates. These random field fluctuations and resulting precession frequency fluctuations cause a loss in phase coherence and therefore a loss in transversal net magnetisation. Additionally, dephasing is caused by magnetic field inhomogeneities, e.g. due to susceptibility variations, which are characterised by a separate decay time T_2'.[14] The combined transverse relaxation rate is called T_2^* with:

$$\frac{1}{T_2^*} = \frac{1}{T_2} + \frac{1}{T_2'} \tag{2.23}$$

The transversal decay is also well described by homogeneous first-order differential

[12] Isolated spins are to a good approximation not interacting. In NMR imaging, i.e. MRI, this condition is satisfied.

[13] For a pure liquid spin-1/2 ensemble, the relaxation processes are dominated by intramolecular dipole-dipole couplings of the spins (Vesanen et al., 2013).

[14] These magnetic field inhomogeneities are constant on the time scale of the common NMR/MRI experiment and this loss in transverse magnetisation can be recovered by a 180° RF pulse, described in Section 2.2.3.

equations (as Eq. 2.21):

$$\frac{dM_x(t)}{dt} = -\frac{M_x(t)}{T_2} \quad \text{and} \quad \frac{dM_y(t)}{dt} = -\frac{M_y(t)}{T_2} \tag{2.24}$$

such that

$$M_x(t) = M_x(0)\, e^{-\frac{t}{T_2}} \quad \text{and} \quad M_y(t) = M_y(0)\, e^{-\frac{t}{T_2}} \tag{2.25}$$

with the transverse relaxation time constants T_2 or T_2^* and in the on-resonant rotating frame of reference (Cavanagh et al., 1995).

Normally the transverse relaxation time T_2 is smaller than the longitudinal time T_1 (Bloch, 1946). However, contrary to popular belief, the theoretical limit of the transverse relaxation rates is:

$$T_2^* \leq T_2 \leq 2 \cdot T_1 \text{ (theoretical limit)} \tag{2.26}$$

and not: $T_2^* \leq T_2 \leq T_1$ which is the usual practical limit (Levitt 2001, Section 11.9.2 and Chapter 20; Traficante, 1991).[15]

Combining the equation for the effective magnetic field 2.16, and the corresponding equation of motion for the net magnetisation in the rotating frame 2.14, with the differential equations describing the longitudinal 2.21 and transversal relaxation 2.24 gives:

$$\begin{pmatrix} \frac{dM_x}{dt} \\ \frac{dM_y}{dt} \\ \frac{dM_z}{dt} \end{pmatrix}_{rot} = \gamma \begin{pmatrix} M_x \\ M_y \\ M_z \end{pmatrix} \times \begin{pmatrix} B_1 \cos(\omega_{RF} t - \Omega t + \varphi) \\ B_1 \sin(\omega_{RF} t - \Omega t + \varphi) \\ B_0 + \frac{\Omega}{\gamma} \end{pmatrix} - \begin{pmatrix} \frac{M_x}{T_2} \\ \frac{M_y}{T_2} \\ \frac{M_z - M_0}{T_1} \end{pmatrix} \tag{2.27}$$

Setting the angular velocity of the rotating frame Ω to the RF field frequency $\Omega = \omega_{RF}$ and defining $\Delta\Omega = \omega_0 - \omega_{RF}$ as the difference between the Larmor frequency of the nuclei and the applied B_1 field.[16] Equation 2.27 can be rewritten as:

$$\frac{dM_x}{dt} = -M_y \Delta\Omega - M_z \gamma B_1 \sin\varphi - \frac{M_x}{T_2} \tag{2.28}$$

$$\frac{dM_y}{dt} = M_x \Delta\Omega + M_z \gamma B_1 \cos\varphi - \frac{M_y}{T_2} \tag{2.29}$$

$$\frac{dM_z}{dt} = -M_y \gamma B_1 \cos\varphi + M_x \gamma B_1 \sin\varphi - \frac{M_z - M_0}{T_1} \tag{2.30}$$

in the rotating frame with $B_0 + \frac{\Omega}{\gamma} = -\frac{\Delta\Omega}{\gamma}$. Equations (2.28) to (2.30) can be rewritten

[15] More on relaxation can be found in the supervised BeLL thesis of Konstantin Holzhausen, who also won the 'VON ARDENNE Physikpreis 2012' for this excellent work (Holzhausen, 2011).

[16] The net magnetisation M, the RF field B_1, the frequency of the RF field ω_{RF} and the phase of the RF field φ are functions of time. For certain applications like fMRI the transversal relaxation rate T_2, for other application like pulsed high field magnets, even B_0 and T_1 are a function of time (Meier et al., 2011).

in matrix form as:

$$\frac{d}{dt}\begin{pmatrix} M_x \\ M_y \\ M_z \end{pmatrix} = \begin{pmatrix} -1/T_2 & -\Delta\Omega & \omega_1 \sin\varphi \\ \Delta\Omega & -1/T_2 & -\omega_1 \cos\varphi \\ -\omega_1 \sin\varphi & \omega_1 \cos\varphi & -1/T_1 \end{pmatrix} \begin{pmatrix} M_x \\ M_y \\ M_z \end{pmatrix} + \begin{pmatrix} 0 \\ 0 \\ M_0/T_1 \end{pmatrix} \tag{2.31}$$

by substituting $-\gamma B_1 = \omega_1$. This is the Bloch equation in the rotating frame of reference in matrix form. The rotating frame of reference is rotating with the RF frequency ω_{RF} (Allard and Helgstrand, 1997; Bloch, 1946).

2.1.5 Chemical Shift

The chemical shift is a variation of the resonant frequency in NMR depending on the local environment (Pople, 1957a,b). Although chemical shift is often a difficulty for MRI applications, it is essential for many NMR experiments and to the temperature measurements described in this thesis (Ivanov et al., 2010).[17]

In NMR the observed resonance frequencies of nuclei normally differ slightly from the predicted values depending on the local molecular environment.[18] The external magnetic field B_0 induces currents in the molecular electron clouds thereby causing variations in local magnetic fields experienced by each separate nucleus. Electrons in the ground state form currents that oppose the external field (Levitt, 2001).[19] This effect is called diamagnetic shielding. Diamagnetic shielding causes the hydrogen protons of the $-CH_3$ group, for example in dimethyl sulfoxide (DMSO, $(CH_3)_2SO$),[20] and hydrogen protons in water H_2O to experience a lower local magnetic field than free protons. In fact, under and close to standard ambient conditions the proton resonance frequency in water is slightly higher in comparison to the proton resonance frequency in DMSO (displayed in Figure 5.5).

Since for a certain nucleus in a molecule the shift in local magnetic field and resulting shift in observed resonance frequency is to a good approximation proportional to the applied field the chemical shift δ is defined as:

$$\boldsymbol{B_{induced}} = \boldsymbol{\delta} \cdot \boldsymbol{B_0} \qquad \text{for} \qquad \boldsymbol{B_{loc}} = \boldsymbol{B_0} + \boldsymbol{B_{induced}} = (\mathbf{1} + \boldsymbol{\delta}) \cdot \boldsymbol{B_0} \tag{2.32}$$

$B_{induced}$ is the induced local magnetic field at the nucleus/proton of interest, B_{loc} is the local magnetic field. In general, $\boldsymbol{\delta}$ is a tensor, however in so-called isotropic liquids, the molecules tumble rapidly through a multitude of molecular orientations such

[17] It is the change of chemical shift that causes the proton resonance frequency shift with temperature in water and separates the water proton frequency from that of protons in fat or DMSO (see Chapter 5 on asymmetric SE MR thermometry).

[18] The predicted resonance frequency is based on Eq. 2.19 and the applied external magnetic field B_0.

[19] Electrons circulating through excited electronic states are able to enhance the local magnetic field.

[20] More information on DMSO is found in Section 5.1.2. The structure of DMSO is depicted in Figure 5.4.

that the chemical shift tensor reduces to its isotropic average, the scalar δ (Levitt, 2001).

Since for many applications the knowledge of the absolute shift δ relative to the free proton frequency f_0 is not necessary and would be difficult to determine. The chemical shift δ is normally determined relative to a reference substance. A very common reference substance in hydrogen NMR is tetramethylsilane (TMS) with the chemical formula $Si(CH_3)_4$. The twelve equivalent hydrogen protons of TMS experience a stronger electronic shielding than most other samples analysed by NMR, i.e. most protons are shielded less and, therefore, experience a positive chemical shift in resonance frequency relative to TMS.[21] The chemical shift is small relative to the expected frequency, about a factor of 10^{-4}, and usually given in parts per million (ppm). More conveniently expressed:

$$\delta_{rel} = \frac{f_{meas} - f_{rel}}{f_{rel}} \qquad \text{or} \qquad \delta_{rel} = \frac{\Delta f}{f_{rel}} \tag{2.33}$$

δ_{ref} is the chemical shift relative to the resonance frequency f_{rel} of TMS or any other reference substance.

Besides other reasons for the chemical shift, for example, ring currents in aromatic molecules, the effect of hydrogen bonding on chemical shift is important to this work (Pople, 1957a,b).

Hydrogen Bonding

As already mentioned in the Introduction (on page 20) the hydrogen bond is central to the unusual physical properties of water, as the high melting and boiling points (Pauling, 1960).[22]

The definition of the International Union of Pure and Applied Chemistry (IUPAC) for the hydrogen bond is: 'A form of association between an electronegative atom and a hydrogen atom attached to a second, relatively electronegative atom. It is best considered as an electrostatic interaction, heightened by the small size of hydrogen, which permits proximity of the interacting dipoles or charges. Both electronegative atoms are usually (but not necessarily) from the first row of the Periodic Table, i.e. N, O or F. Hydrogen bonds may be inter-molecular or intramolecular.' (Mcnaught and Wilkinson, 1997).[23] Most of the hydrogen bond attraction is due to the electrostatic effects. These are increased by mutual polarization.

[21] A reason for the strong shielding is the low electronegativity of silicon (1.9) in comparison to carbon (2.55), hydrogen (2.2) and oxygen (3.44), leading to a relative high electron density around the hydrogen proton in TMS (Pauling, 1960).

[22] Pauling estimates that, based on the sequence of related substances in the oxygen group (H_2Te, H_2Se, and H_2S), the expected melting and boiling points of water without hydrogen bonding to be about -100°C and -80°C, respectively.

[23] There also exist hydrogen bonds between the oxygen atom in DMSO and the hydrogen atoms of water in H_2O/DMSO solutions, similarly affecting the electron density around the water protons (Mizuno et al., 2000). Mizuno et al. also mentions that the interaction between the hydrogen of DMSO and the surrounding oxygen of water may have some hydrogen bonding character.

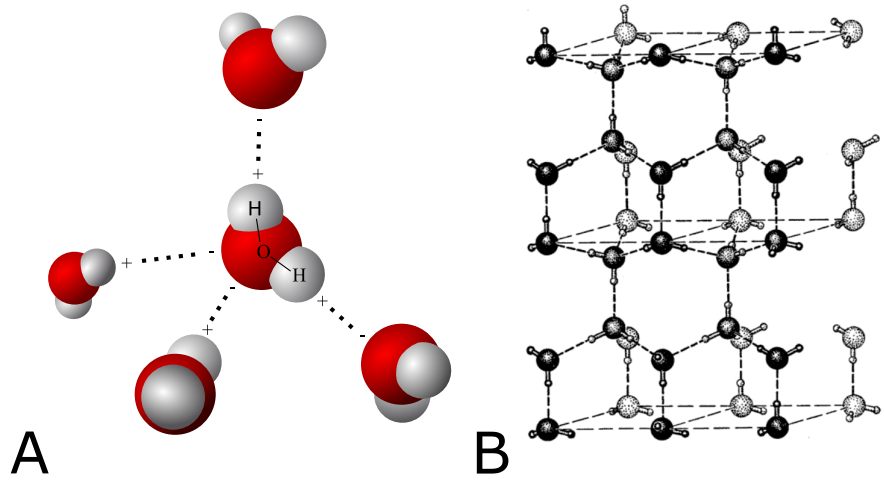

Figure 2.3: *Hydrogen bond model in water. (A) The bent water molecule has four partially charged sites. Two partially positive charged hydrogen atoms and a partially negative oxygen atom with two lone electron pairs. The spatial association due to electrostatic interaction of a partially negatively charged atom, in this case, the oxygen and a partially positive hydrogen is called a hydrogen bond. (B) A single water molecule can hydrogen bond to 4 neighboring water molecules, forming a connected tetrahedral structure that is the basic element of ice. The covalent bond length between oxygen and hydrogen in a water molecule is approximately* 1 *Å. The length of a hydrogen bond between a oxygen and hydrogen atom is approximately* 1.7 *Å (Mcnaught and Wilkinson, 1997; Nemethy and Scheraga, 1962; Pauling, 1960). (Image A from Wikipedia: Model of hydrogen bonds in water, accessed 28 Mar. 2016; Image B from Pauling, 1960.)).*

Shown in Figure 2.3 are two sketches of hydrogen bonding in water. The bent water molecule with its two positively charged hydrogen atoms and its two lone electron pairs can participate in up to four hydrogen bonds. The four partially charged sites form hydrogen bonds to the oppositely charged sites of four different water molecules. In ice, these four hydrogen bonds of each water molecule form a space-filling three dimensional crystal structure of hexagonal symmetry, depicted in Figure 2.3B. The energy of a hydrogen bond is on the order of 23 kJ/mol and therefore at body temperature approximately eight times higher than the thermal energy kT (Stillinger, 1980). The hydrogen bonds in liquid water are therefore constantly strained, bent and broken by thermal fluctuations.[24] The change in number and quality of hydrogen bonds in water is the main reason for the temperature dependent proton chemical shift in water that is basic to this work.

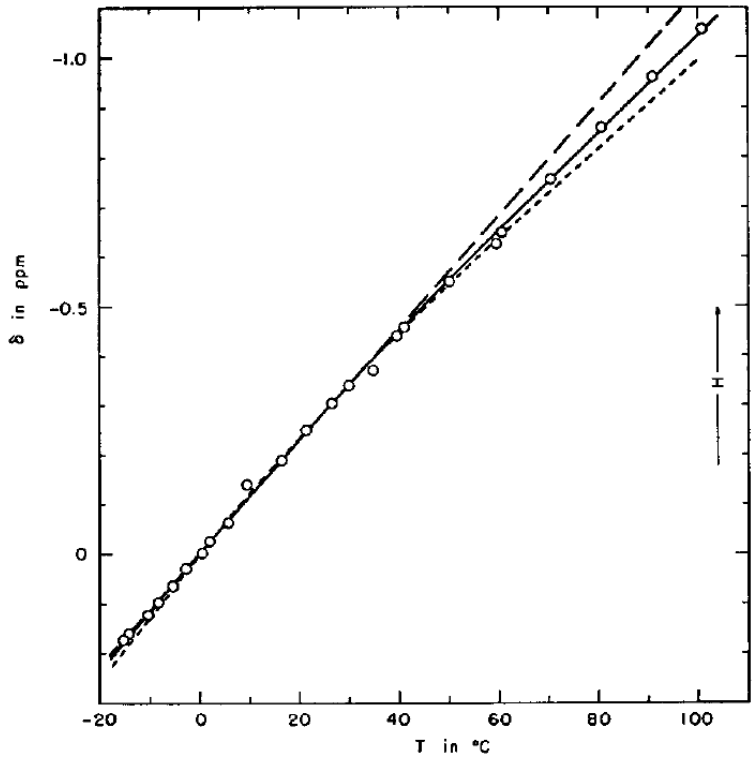

Figure 2.4: *Chemical shift of water as a function of temperature measured by Hindman in 1966. Since the magnetic susceptibility of water also slightly changes with temperature, the measured chemical shift (marked by ∘) was corrected for the variation in susceptibility. Corrected data is shown by the dashed line (- -). Image from Hindman 1966.*

Temperature-dependent Chemical Shift and Hydrogen Bonding

Pauling states that in liquid water, each molecule is hydrogen bonded to at least one other molecule at any time and the small value 6 kJ/mol of the enthalpy of fusion of ice shows that on melting only about 15 % of the hydrogen bonds are broken (Pauling, 1960). Cross et al. determined by Raman spectroscopy that liquid water still contains a considerable amount of water molecules with four, three, and two hydrogen bonds. Estimating that at 26°C slightly less than 50 % of the possible hydrogen bonds are broken (Cross et al., 1937). However, there is a large scatter in the literature ranging from 2 to almost four hydrogen bonds per molecule at body temperature (Rastogi et al., 2011).[25] Nevertheless, it is evident from a multitude of studies that the tetrahedral formation, type and number of hydrogen bonds per molecule decreases with temperature (Bakker and Skinner, 2009; Stillinger, 1980).

In most cases hydrogen bonds cause a positive shift in proton resonance frequency,

[24]The low bond energy and small activation energy of the hydrogen bond make the hydrogen bond particularly suited to be involved in reactions occurring at normal temperatures, as the body temperature (Pauling, 1960).

[25]Rastogi et al. gives the following causes of the large scatter in the average number of hydrogen bonds: differences in the definition of a hydrogen bond, limitations in the experimental technique and ambiguities in the interpretation of the experimental data.

i.e. the proton experiences less chemical shielding. Hydrogen bonds in water also cause a positive shift in proton resonance frequency. This positive shift in frequency is interesting since the hydrogen atom forms a hydrogen bond with a lone electron pair that should increase the electron density in the proximity of the hydrogen proton. However, the main effect determining the shift of the proton frequency is due to the reduction in diamagnetic circulation of the electrons in the covalent O-H bond around the proton in the water molecule. The reduction in diamagnetic circulation around the proton is due to the negative electrostatic field of the other hydrogen bonding partner (Schneider et al., 1958). Schneider et al. (1958) and Hindman (1966) measured the temperature dependence of the chemical shift of the protons resonance frequency in liquid water. Figure 2.4 depicts the measured and susceptibility corrected data of Hindman. Over the range from -20°C to 100°C, the change of chemical shift with temperature is almost linear with -0.0103 ppm/K. Interestingly, the chemical shift difference of methane CH_4 and water in the gaseous phase is within the experimental error independent of temperature and pressure (Hindman, 1966).

2.2 Magnetic Resonance Imaging

The net magnetisation $\boldsymbol{M}$ of Section 2.1.2 can be manipulated by RF pulses to have a component precessing in the plane perpendicular to the static magnetic field $\boldsymbol{B_0}$.[26] The precessing transverse net magnetisation can induce a voltage in a receive coil nearby (cf. eqs. 2.9 and 2.31; (Bloch, 1946; Hoult and Bhakar, 1997)). Simultaneously applied magnetic field gradients modify the local magnetic field resulting in locally different precession frequencies of the local net magnetisations. By applying magnetic field gradients in three perpendicular directions, the magnetisation distribution can be spatially encoded (Lauterbur, 1973).

2.2.1 Magnetic Field Gradients

In modern MRI scanners, there is a set of three mutually perpendicular magnetic gradient coils (Turner, 1993). These gradient coils can establish additional magnetic fields that modulate $\boldsymbol{B_0}$ such that the net magnetic field in z-direction (the direction of $\boldsymbol{B_0}$) varies linearly with position:[27]

$$B_z(x,y,z,t) = B_0 + x \cdot G_x(t) + y \cdot G_y(t) + z \cdot G_z(t) \tag{2.34}$$

with

$$G_x = \frac{dB_z}{dx}\ , \quad G_y = \frac{dB_z}{dy} \quad \text{and} \quad G_z = \frac{dB_z}{dz} \tag{2.35}$$

[26] As described in section Section 2.1.3 on the effect of RF fields on the magnetisation.

[27] The achieved magnetic field gradient is accurate to about 5 % over the enclosed volume. According to Maxwell's equations the magnetic field gradients in z-direction are accompanied by magnetic fields in x and y-direction. The effect of these fields can in most cases be neglected and decreases with the main magnetic field strength (Haacke et al., 1999).

$G_{x,y,z}$ are the magnetic field gradients in x, y and z-direction, respectively and are given in units of Tesla per meter.[28] The additional magnetic field gradients cause a change in resonant frequency of the local net magnetisation with position. For the precession frequency ω of the local magnetisation holds:

$$\omega(x,y,z,t) = -\gamma B_0 - \gamma\left(xG_x(t) + yG_y(t) + zG_z(t)\right) \tag{2.36}$$

Resulting in a local magnetisation phase angle change during time t of:

$$\varphi(x,y,z,t) = -\gamma B_0 t - \gamma \int_0^t xG_x(t') + yG_y(t') + zG_z(t')\,dt' \tag{2.37}$$

2.2.2 Imaging Equation

As a solution of the Bloch Equation 2.31 the local transverse magnetisation M_{xy} can be written as:

$$M_{xy}(t) = M_{xy}(t=0)\cdot e^{i\varphi(t)} \tag{2.38}$$

with the real part corresponding to the x-direction and the imaginary part corresponding to the y-direction.[29] For time-dependent magnetic field gradients the transverse magnetisation is:

$$M_{xy}(x,y,z,t) = M_{xy}(x,y,z,t=0)\cdot e^{-i\gamma B_0 t}\cdot e^{-i\gamma\int_0^t xG_x(t')+yG_y(t')+zG_z(t')dt'} \tag{2.39}$$

The measured MR signal $S(t)$, induced in the receive coils is the weighted volume integral over the whole imaging volume of the precessing transverse magnetisation of Equation 2.39:

$$S(t) = \iiint_V B_1^-(x,y,z)\cdot M_{xy}(x,y,z,t)\,dx\,dy\,dz \tag{2.40}$$

with the receive coil weighting factor $B_1^-(x,y,z)$. B_1^- is a complex position-, tissue- and coil-dependent weighting factor (Bernstein et al., 1994; Roemer et al., 1990).[30]

[28] The whole-body Siemens Magnetom 7 T system used for this work can produce gradient amplitudes of 45 mT/m with a maximal slew rate of 200 T/m/s.

[29] Here the signal decay due to relaxation is neglected. This decay would just be a multiplicative term that in the end leads to a convolution of the MR image with its sequence and tissue dependent point spread function (Haacke et al., 1999; Patzig, 2016).

[30] Compare the receive field $\boldsymbol{B_1^-}$ with Chapter 3 on the transmit RF field, also called $\boldsymbol{B_1^+}$ field. For the optimal reconstruction of the phase difference maps in Section 5.1.3 these receive coil dependent phase distortions were removed by subtraction.

Substituting Eq. 2.39 into Eq. 2.40 gives:

$$S(t) = \iiint_V B_1^-(x,y,z) \cdot M_{xy}(x,y,z,t=0) \cdot e^{-i\gamma B_0 t} \cdot e^{-i\gamma \int_0^t xG_x(t')+yG_y(t')+zG_z(t')dt'} dx\,dy\,dz \tag{2.41}$$

Due to the linearity of the magnetic field gradients $G_{x,y,z}$, the local magnetisation phase $\varphi(x,y,z,t)$ (cf. Eq. 2.36 and Eq. 2.37) also varies linearly with position. Therefore it is possible to define wave vectors $k_{x,y,z}(t)$ describing the angular spatial frequency of the magnetisation phase in all three directions:

$$k_{x,y,z}(t) = \frac{\gamma}{2\pi} \int_0^t G_{x,y,z}(t')\,dt' \tag{2.42}$$

with $t = 0\ s$ the isodelay point of the RF excitation pulse.[31] The wave vectors $k_{x,y,z}$ can be thought of as coordinates in k-space. K-Space contains the measured MR signal at the positions given by equation 2.42. Substituting the wave vectors $k_{x,y,z}(t)$ (Eq. 2.42) into the signal Equation 2.41 results in:

$$S(t) = \iiint_V B_1^-(x,y,z) \cdot M_{xy}(x,y,z,t=0) \cdot e^{-i\gamma B_0 t} \cdot e^{-i2\pi x \cdot k_x(t)} \cdot e^{-i2\pi y \cdot k_y(t)} \cdot e^{-i2\pi z \cdot k_z(t)} dx\,dy\,dz \tag{2.43}$$

After demodulation with the resonance frequency the fast oscillation with $\omega_0 = -\gamma B_0$ is removed, i.e. the exponential factor $e^{-i\gamma B_0 t}$ in Equation 2.43.

$$S(t)_{rot} = \iiint_V B_1^-(x,y,z) \cdot M_{xy}(x,y,z,t=0) \cdot e^{-i2\pi x \cdot k_x(t)} \cdot e^{-i2\pi y \cdot k_y(t)} \cdot e^{-i2\pi z \cdot k_z(t)} dx\,dy\,dz \tag{2.44}$$

Looking at Equation 2.44 it is apparent that the demodulated signal $S(t)_{rot}$ is the Fourier transform of the weighted transverse magnetisation $M_{xy} \cdot B_1^-$. The inverse Fourier transform of $S(t)_{rot}$ recovers the spatially distributed weighted magnetisation:

$$M_{xy}(x,y,z) \cdot B_1^-(x,y,z) = \int_{k_x} \int_{k_y} \int_{k_z} S(k_x,k_y,k_z)_{rot} \cdot e^{-i2\pi x \cdot k_x} \cdot e^{-i2\pi y \cdot k_y} \cdot e^{-i2\pi z \cdot k_z} dk_x\,dk_y\,dk_z \tag{2.45}$$

[31] The isodelay point of an RF pulse describes the point in time for which the RF pulse can be approximated by an instantaneous magnetisation flip of equal flip angle.

with the function $k_{x,y,z}(t)$ given by Equation 2.42. Depending on the sequence, the demodulated signal $S(t)_{rot}$ describes a trajectory through k-space. The sequence type and corresponding parameters determine the k-space trajectory by the timing of the RF-pulses and magnetic field gradients. Most common is a rectilinear k-space path. For this work k-space was exclusively sampled in a 2D or 3D rectilinear fashion. By convention, the direction along acquired lines is called read direction and perpendicular to it, across lines, phase direction. The different methods of acquiring k-space by a certain sequence of RF pulses and magnetic field gradients are call MRI sequences. There are an infinite number of ways to sample k-space in an MRI scan. Next, the most important MRI sequences are explained.

2.2.3 MRI Sequences

MRI sequences describe a specific series of RF and magnetic field gradient pulses which are applied during an MRI scan to produce a desired MR signal.

Spin Echo

The spin-echo (SE) sequence is based on the application of two RF pulses. A 90° excitation RF pulse generates transverse magnetisation. Imaging gradients, magnetic field inhomogeneities, susceptibility variations and others sources (see Section 2.1.4 on relaxation) cause the transverse magnetisation to dephase. A second refocusing RF pulse rotates the complete or partially dispersed magnetisation by 180° such that the magnetisation rephases again to form a spin echo. Normally the refocusing is about an axis in the transverse plane and perpendicular to the 90° excitation RF pulse direction. The time between the 90° and the 180° RF pulses is equal to the time between the 180° pulse and the refocused net magnetisation maximum. The refocused net magnetisation maximum is known as a spin, or Hahn echo (Hahn, 1950; Hennig, 1991). The echo time (TE) is the time between the excitation RF pulse and the spin echo. For most applications, TE_{SE} is set to coincide with the acquisition of the centre of k-space. However, the aim of this work was to detect small changes in MR phase due to small changes in resonance frequency. Phase sensitivity of the SE sequence can be achieved by shifting the acquisition of the centre of k-space back in time, to be reached later than the spin echo.[32] Here the time between the spin echo and the k-space centre of the readout is called effective echo time TE_{eff}, effective since this is the time of free MR phase evolution.[33]

Refocusing RF pulses normally have flip angles of 180°, however, also other pulses are capable of rephasing the magnetisation to produce a SE. Considering an isochromat[34] with offset frequency $\Delta\omega$ undergoing the SE sequence $\theta_x - \tau - (2\theta)_y -$

[32]The centre of k-space is defined as $k_{Read} = 0$ and $k_{PE} = 0$.

[33]Bernstein et al. defines TE_{eff} differently as the time between RF excitation and k-space centre of the readout.

[34]An imagined group of spins that precess at the same frequency during the NMR/MRI

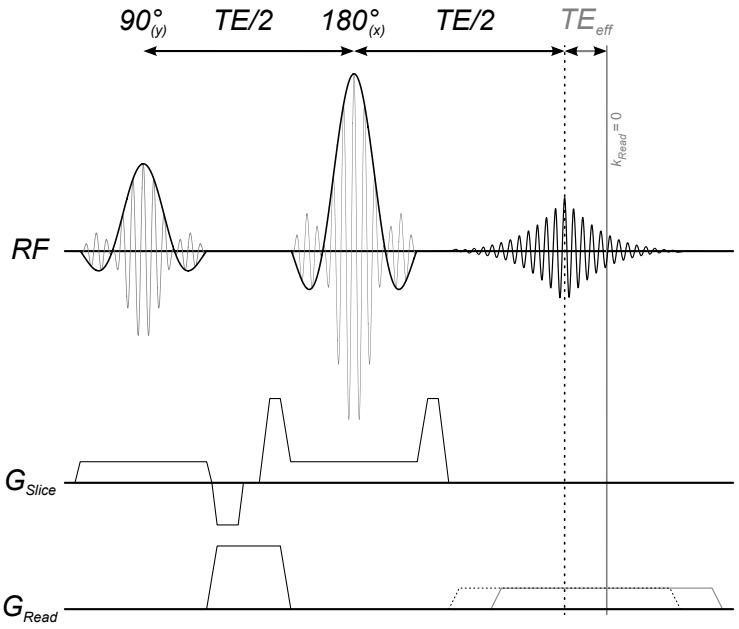

Figure 2.5: *Displayed is a basic slice-selective spin-echo sequence. The 90° sinc-shaped excitation RF pulse is about the y-axis in the on-resonant frame of reference and rotates the magnetisation into the transverse plane. The 180° sinc-shaped refocusing RF pulse is about the x-axis. The 90° and 180° RF pulses generate a magnetisation maximum, i.e. echo, at the echo time TE (Hahn, 1950). The simultaneously applied slice-select gradient G_{Slice} makes the RF pulses slice selective. After the 90° RF excitation pulse, the G_{Slice} gradient is rephased. Before and after the 180° RF pulse crusher gradients dephase unwanted signal pathways. For conventional SE sequences, the slice-select gradients G_{Slice} during excitation and refocusing have similar amplitudes. To traverse a line in k-space during signal acquisition and to generate a gradient-echo, the read gradient G_{Read} is prephased (see pages 41ff. on the gradient-recalled echo). Prephasing can be done before or after the refocusing pulse. Normally prephasing is done between the excitation and refocusing RF pulse, in this case, the prephasing gradient has the same gradient polarity as the read gradient G_{Read} during signal acquisition. The gradient echo, i.e. $k_{Read} = 0$, and the spin-echo can be made to not coincide in time, then the time between the spin-echo and gradient echo is defined as the effective echo time TE_{eff}. The effective echo time between the SE and GRE is used in Chapter 5 for MR thermometry. The oscillating curves of the RF pulses with the sinc envelope are supposed to indicate the fact that the RF field oscillates at approximately 300 MHz at 7 T with a sinc-shaped amplitude modulation. The sinc-shaped amplitude modulation makes the RF pulse selective for a certain frequency range and, in combination with a gradient, slice selective. Not displayed in the figure is the fact that there is a phase shift of 90° between the excitation and refocusing RF pulses. The RF pulses are phase shifted since the pulses are about the y- and x-axes, respectively.*

experiment is called an isochromat, i.e. they are imagined to experience the same magnetic field, the same field gradients and move together in space.

$\tau -$ acquisition. Time τ between the excitation and refocusing RF pulse and the refocusing RF pulse to have twice the flip angle θ as the excitation RF pulse. The $\boldsymbol{B_1}$ field of the excitation RF pulse is about the x-axis in the rotating on-resonant frame of reference and the $\boldsymbol{B_1}$ field of the refocusing RF pulse about the y-axis of the rotating frame of reference. Ignoring relaxation effects the resulting magnetisation at the time of the SE is:

$$M_{iso} = R_z(\varphi)\, R_y(2\,\theta)\, R_z(\varphi)\, R_x(-\theta)\, M_0 \tag{2.46}$$

R_x, R_y and R_z are rotation matrices around the x-, y-, and z-axis in the rotating frame of reference, respectively and the phase offset $\varphi = \Delta\omega \cdot \tau$.[35] Figure 2.6 displays

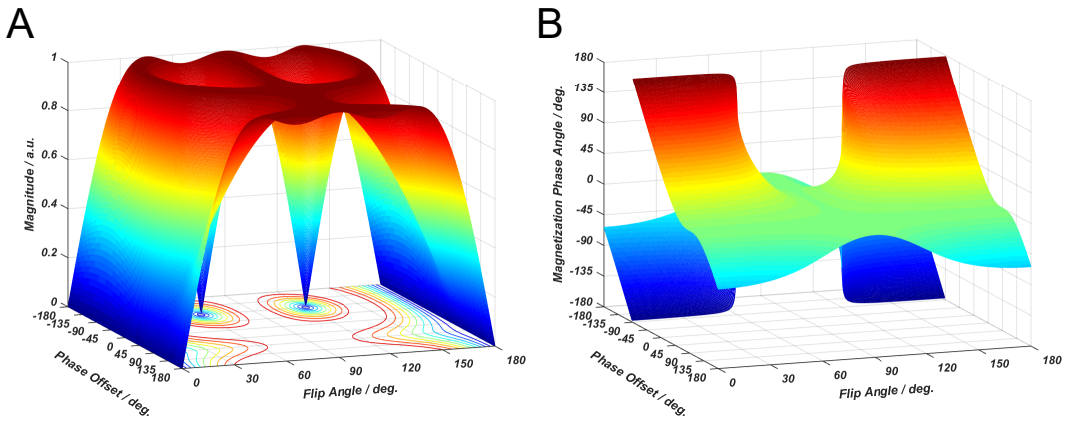

Figure 2.6: *The magnitude (A) and phase (B) of the isochromat's magnetisation in the transverse plane at the time of the SE are displayed. The simulation is based on the sequence which is described in Equation 2.46. The magnitude and phase are functions of flip angle θ and the phase offset φ which is acquired during the time τ. τ is the time between the excitation and refocusing RF pulse and between the refocusing pulse and the SE. The refocusing flip angle is assumed to be twice the excitation flip angle. For an excitation flip angle of 90° and a refocusing flip angle of 180°, all isochromats are in the transverse plane and parallel to the y-axis. For the different flip angle, the isochromats magnetisation is not completely in the transverse plane, and not all are parallel to the y-axis. The summation over all phase offsets φ gives the signal amplitude of the SE for different flip angle θ. It is given by $|M_0| \sin^3\theta$, cf. Eq. 2.48.*

the magnitude and the phase of the isochromat's magnetisation depending on flip angle and phase offset.

Now considering an ensemble of isochromats with a uniform distribution of offset

[35] A negative excitation flip angle was chosen to achieve a net magnetisation at the SE in the direction of the positive y-axis.

frequencies $\Delta\omega$, then the net magnetisation M_{acq} at the time of the SE is given by:

$$M_{acq} = \frac{1}{2\pi} \int_{-\pi}^{\pi} R_z(\varphi)\, R_y(2\,\theta)\, R_z(\varphi)\, R_x(-\theta)\, M_0\, d\varphi \tag{2.47}$$

$$= \begin{pmatrix} 0 \\ \sin^3\theta \\ \cos\theta \cdot \left(2\cos^2\theta - 1\right) \end{pmatrix} |M_0| \tag{2.48}$$

The results of the Bloch simulations in Section 5.2.4 on page 115 also illustrate the relationship between flip angle and signal amplitude for the on resonant case. Normally when running a SE MRI sequence, the SE is combined with a simultaneously occurring gradient echo.

Gradient-Recalled Echo

The Gradient-Recalled Echo (GRE) is mainly used for the fast acquisition of a line in k-space as in the 'fast low-angle shot' (FLASH) sequence by Haase et al. and Frahm et al. (1986). To generate an echo the gradient rephases the magnetisation. Contrary to the SE, where the refocusing RF pulse generates the echo.

For example, after the RF excitation pulse, usually with a flip angle considerably below 90°, a prephase gradient in read direction is applied. The prephase gradient dephases the transverse magnetisation which is then rephased by the read gradient during signal acquisition. Prephase and rephase gradient have opposite polarity and the signal maximum, i.e. gradient-recalled echo, occurs when the integral over the gradient lobes in read direction is zero again.

The echo time is defined as the time between the isodelay point of the RF excitation pulse and the nulling of the read and phase gradient integral, i.e. when the centre of k-space is passed ($k_{Read} = 0$). The repetition time (TR) between consecutive excitation RF pulses and readouts can be short since the excitation flip angles are below 90°. Magnetisation is not inverted, and low flip angles leave substantial amounts of longitudinal magnetisation along B_0 undisturbed, leading to a high SNR efficiency.[36] The Ernst angle is the flip angle that provides optimal signal-to-noise for a given TR (Ernst and Anderson, 1966). GRE sequences deposit relatively small amounts of energy in the imaged tissue, due to the low flip angle, therefore, it is suited for high field MRI (see Section 2.6 on RF Heating). However, the signal decays with T_2^* in comparison to T_2 for the SE. T_2^* can be considerably smaller than T_2 for example close to air-tissue boundaries. Still, transverse magnetisation remains when TR is on the order or less than T_2 at the time of the next repetition. In one type of GRE sequences, it is being attempted to destroy this transverse magnetisation such that none of the transverse magnetisation contributes to the signal of the next repetition. Therefore these type of GRE sequences are called spoiled or incoherent

[36] Gradient echo flip angle are typically in the range between 5°-30° and repetition times between 5ms to several hundred milliseconds.

GRE sequences.[37] In the other type of GRE sequences, the transverse magnetisation and the end of the repetition is not spoiled and therefore contributes to the following signals. These type of sequences are called steady-state free precession or coherent steady-state sequences. In this work, for B_0 and B_1^+ mapping, only spoiled gradient echo sequences were used.

Up to now, the excitation RF pulse for GRE imaging and the refocusing RF pulse for SE imaging was followed by the acquisition of one line of k-space. Echo planar imaging allows acquiring the complete k-space, at least of one slice, by repeated gradient-recalled echoes after just one excitation.

Echo Planar Imaging

Echo planar imaging (EPI) was introduced by Mansfield trying to speed up MR imaging (Mansfield, 1977).[38] EPI is one of the fastest conventional MRI sequence acquisition techniques and now the most popular fMRI imaging method (Speck et al., 2008). [39] EPI differs from the standard SE or GRE sequences by employing all the read and phase encoding steps for a complete 2D image after just a single RF preparation step.[40] In the most common EPI method, after the RF preparation, k-space is traversed by a series of gradient echoes in a rectilinear meander-like fashion.

Figure 2.7 displays a typical 2D GRE EPI pulse sequence. The pulse sequence starts with a slice-selective excitation RF pulse. Then the slice select gradient is rewound. At the same time, the readout and phase gradient are prephased to one of the outer corners of k-space. Followed by the acquisition of consecutive lines of k-space by the oscillating read gradient. At the end of the lines in k-space phase encoding gradient blips move the acquisition to the next line of acquisition in k-space. This way 2D images can be acquired in tens of milliseconds. However, the acquired signal requires pre-processing before doing a 2D Fourier-transform since the k-space data is distorted, i.e. the k-space trajectory during signal acquisition is distorted (Haacke et al., 1999).

EPI is prone to image artefacts like distortions and each line in k-space has a slightly different TE. One way to cope with these challenges is to use parallel imaging techniques (Griswold et al., 2002; Pruessmann et al., 1999).[41]

For SE EPI the refocusing RF pulse is added before the EPI readout. As for GRE EPI, the k-space in SE EPI is sampled by gradient echoes. Prephasing of the read

[37] A combination of RF and gradient spoiling is applied (Bernstein et al., 2004; Zur et al., 1991).

[38] Mansfield states: 'Speed is imperative if NMR is to be successfully used in medical imaging.'

[39] Newer approaches to fast scanning are radial undersampling or compressed sensing used for heart imaging or MR thermometry (Cao et al., 2015; Krahmer and Ward, 2014; Uecker et al., 2010).

[40] For GRE EPI the RF preparation just includes the RF excitation pulse and the slice select gradient, while for SE EPI the refocusing RF pulse and crusher gradients are also included.

[41] Different echo times for each line of k-space influences the MR phase. The MR thermometry in this work utilises MR phase measurements. Parallel imaging can significantly reduce the problem of MR phase and distortions in EPI scanning. In this work, GRAPPA was used for EPI scanning sampling only every 4th line of k-space (see Chapter 5 on SE thermometry).

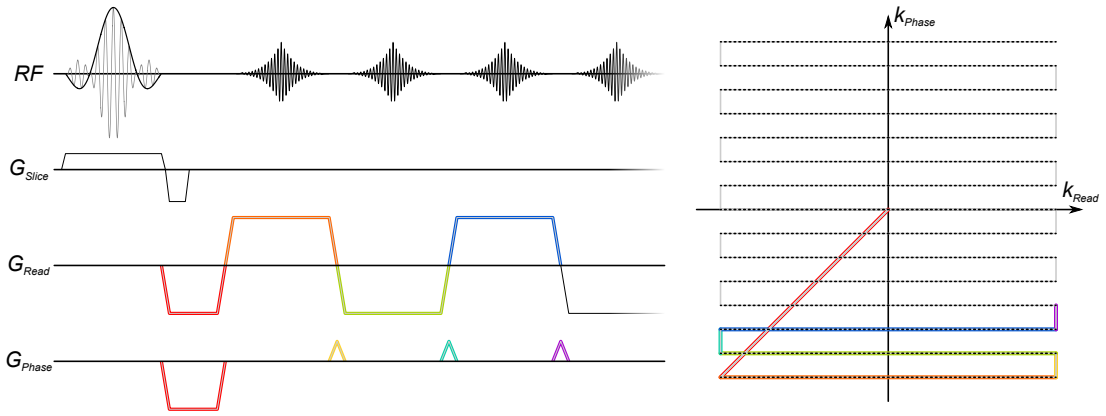

Figure 2.7: *Displayed is a basic echo planar imaging (EPI) sequence. The slice-selective sinc-shaped excitation RF pulse generates a transverse magnetisation. Excitation is followed by the prephasing of the read G_{Read} and phase G_{Phase} gradients to the outer edges of k-space (red). Then the bipolar echo planar imaging readout starts. The first line (orange) of k-space is acquired from left to right, followed by a phase encoding gradient G_{Phase} blip (yellow). The G_{Phase} blip moves the acquisition one line up in k-space. The second line (green) of k-space is acquired from right to left, again followed by a phase encoding gradient blip (turquoise). During each acquisition of a line in k-space a gradient-echo at ($k_{Read} = 0$) is produced. The echo amplitudes for these echoes depend on the transverse relaxation rate T_2^* and the position in k-space k_{Phase}, and obviously on the initial transverse magnetisation and its spatial distribution. In this work, the transverse magnetisation was prepared by a spin-echo excitation and refocusing RF pulse prior to the EPI readout (see Section 5.1.1). Parallel imaging techniques can reduce the number of lines in k-space, increasing the phase-encoding gradient blips and decrease the duration of acquisition (Griswold et al., 2002; Pruessmann et al., 1999).*

and phase gradients can be done before the refocusing RF pulse to save time.[42] To dephase unwanted signal pathways crusher gradients before and after the refocusing pulse are needed. Other methods than rectilinear meander like k-space sampling are also possible. For example, zig-zag, spiral, oscillating (Haacke et al., 1999).

Discrete and Finite Sampling

In practice, the analogue signal $S(t)_{rot}$ is sampled at finite and discrete points in time. The processes of truncation and discretization lead to artefacts in the reconstructed image. Haacke and Patzig nicely explain these artefacts and their origin (Haacke et al., 1999; Patzig, 2016). The signal is sampled at discrete points in time, i.e. at discrete values of k in steps of:

$$\Delta k(t) = \frac{\gamma}{2\pi} \int_{t}^{t+\Delta t} G(t')\, dt' \tag{2.49}$$

[42] If prephasing is done before the refocusing RF pulse the gradient amplitude has to be reversed.

with the time interval Δt between the sampled points. The lowest spatial frequency unequal to zero determines the distance for which the Fourier transform of the acquired signal repeats itself. This repetition length is the field of view (FOV) and defined as $FOV = 1/\Delta k_{x,y,z}$.[43] If the FOV is smaller than the physical spin density, aliasing occurs. The bandwidth in read direction BW_{Read} for a constant read gradient G_R is:

$$BW_{Read} = f_R = \frac{1}{\Delta t} = \frac{\gamma}{2\pi} \cdot G_R \cdot FOV \tag{2.50}$$

The bandwidth in phase encoding direction for conventional gradient echo sequences is virtually infinite since the time between the excitation RF pulse, and signal acquisition is equal for each acquired line in k-space. However, in echo-planar imaging the bandwidth BW_{Phase} in phase encoding direction is:

$$BW_{Phase} = \frac{1}{\Delta t_{Phase}} \tag{2.51}$$

where Δt_{Phase} is the time between the acquisition of consecutive lines in k-space. Finite imaging bandwidths lead to displacement of off-resonant nuclei (Jezzard and Balaban, 1995).[44] For the displacement x_{displ} holds:

$$x_{displ} = \frac{FOV}{BW} \cdot \Delta f = N \cdot x_{voxel} \cdot \Delta t_{Read/Phase} \cdot \Delta f \tag{2.52}$$

with Δf being the frequency offset, N the number of voxel and x_{voxel} the voxel size both in the imaging direction of interest.

2.3 MR Thermometry

A review by Tempany et al. discussing surgery based on focused ultrasound, argues convincingly that the opportunity for simultaneous excellent soft-tissue contrast and non-invasive real-time thermometry makes MR the most reliable and comprehensive modality available to guide therapeutic ultrasound (Lewa and de Certaines, 1994; Tempany et al., 2011). For this reason, MR thermometry has found clinical applications in recent years for uterine fibroid ablation and hyperthermia of brain and abdominal tissue (Dadakova et al., 2014; Hindley et al., 2004; Kickhefel et al., 2011; Rieke et al., 2013). Not only is MRI compatible with focused ultrasound, but so too are cryoablation and laser ablation (Saccomandi et al., 2013). Numerous physical quantities that show temperature dependence are measurable by MRI (or MR spectroscopy). The most prominent parameters are, the proton resonance fre-

[43] $FOV = 1/\Delta k_{x,y,z}$ since the lowest spatial frequency is $\Delta k_{x,y,z}$ off from $k_{x,y,z} = 0/m$, the k-space centre.

[44] Possible causes for off-resonant spins are for example B_0 field-inhomogeneities or chemically shifted nuclei.

quency (PRF), the apparent diffusion coefficient D, and the T_1 and T_2 relaxation times. An overview of the different temperature-dependent parameters and MR thermometry techniques is given here, with a particular focus on the PRF shift methods. PRF shift MR thermometry methods are the preferred choice for many applications (McDannold et al., 2008; Odéen et al., 2016; Rieke and Butts-Pauly, 2008b) and PRF-based thermometry challenges and solutions are at the heart of this work.

2.3.1 Diffusion

Based on the Stokes-Einstein relation between viscosity and the translational self-diffusion coefficient D, the following relation holds:

$$D \propto e^{-\frac{E_a}{k_B T}} \tag{2.53}$$

Where k_B is the Boltzmann constant,[45] E_a the activation energy for translational diffusion and T the absolute temperature (Bloembergen et al., 1948; Dhital et al., 2015; Le Bihan et al., 1989; Simpson and Carr, 1958). The temperature dependent self-diffusion coefficient D describes the average thermal Brownian motion of molecules or particles in a medium. D can be measured using standard diffusion-weighted MRI sequences that relate diffusion in certain directions to MR signal attenuation (Chilla et al., 2015). Differentiating Eq. 2.53 leads to the temperature dependence of D:

$$\frac{dD}{D} = \frac{E_a}{k_B T} \cdot \frac{dT}{T} \tag{2.54}$$

assuming the activation energy E_a to be independent of temperature (Le Bihan et al., 1989). Then for a temperature change of 1 K in pure water ($E_a = 18.8$ kJ/mol)[46] the diffusion coefficient changes by approximately 2.4 %.[47]

Although temperature sensitivity is comparatively high, there are several challenges related to diffusion MR thermometry, like long scan times, sensitivity to motion, heat induced tissue changes can lead to large changes in diffusion coefficient and anisotropic diffusion for example in muscle tissue (Rieke2008). The T_1 relaxation rate also changes with temperature causing problems for diffusion based MR thermometry, yet T_1 can also be used for MR thermometry.

[45] The Boltzmann constant $k_B = 1.3806 \cdot 10^{-23}$ J/K.

[46] Dhital et al. estimates the activation energies in brain white matter to be 13.9 kJ/mol and 8.3 kJ/mol for the fast and the slow water pool, respectively. The smaller activation energies compared to water also reduce the sensitivity.

[47] A water molecule at body temperature wanders over a distance of approximately 13 μm over a time interval of 10 ms in 3D (Holz et al., 2000; Levitt, 2001).

2.3.2 T_1 Relaxation

The longitudinal or spin-lattice relaxation rate T_1 shortly described in Section 2.1.4 is also temperature dependent and in general increases with temperature (Nelson and Tung, 1987). For biological tissue above a minimum temperature, the temperature dependence of T_1 can well be approximated by:

$$T_1 \propto e^{-\frac{E_a}{k_B T}} \tag{2.55}$$

where E_a describes the activation energy of the spin-lattice relaxation process and, as above, k_B the Boltzmann constant and T the absolute temperature (Bottomley et al., 1984; Parker et al., 1983; Rieke and Butts-Pauly, 2008b).[48] For small changes in temperature[49], T_1 can be approximated by:

$$T_1(T) = T_1(T_{ref}) + m \cdot (T - T_{ref}) \tag{2.56}$$

where T_{ref} is the reference temperature, T the temperature of interest and $m = dT_1/dT$ needs to be determined empirically for each tissue type (Birkl et al., 2013; Todd et al., 2013).

Normally the measured temperature dependence of T_1 is between 1 and 2 %/°C in breast tissue, bovine muscle, liver, and fat and even 3.6 % in oils samples (Nelson and Tung, 1987; Rieke and Butts-Pauly, 2008b). Fast methods rely on correction schemes based on the steady-state signal and B_1^+ corrections, while inversion recovery sequences or saturation recovery sequences give a more direct measure of T_1 but are time-consuming. Additionally, the sequences should be frequency-selective since water and fat have significantly different T_1 values.[50]

Although T_1 and the change in T_1 are tissue dependent and T_1 imaging is relatively time-consuming and heat induced protein denaturation can lead to large changes in T_1 of water protons, T_1 based MR thermometry is still used, especially in fatty tissue or close to significant susceptibility differences as in the vicinity of metallic implants (Baron et al., 2015; Gensler et al., 2012; Hynynen et al., 2000; Kuroda et al., 2011; Todd et al., 2014).

2.3.3 T_2 Relaxation

Inversely related to viscosity and similarly dependent on T as T_1, T_2 is also temperature dependent (Nelson and Tung, 1987; Parker, 1984).[51] In aqueous solutions,

[48] In fact, Eq. 2.53 and Eq. 2.55 are related, for more details see Simpson and Carr (1958).

[49] Common are temperature changes of $10 - 30$°C.

[50] Todd et al. (2014) segmented breast tissue in high water (above 75 %) and high fat (above 75 %) sections and performed PRF phase-based thermometry in water and T_1-based thermometry in fat sections.

[51] This holds for $\tau \cdot \omega < 1$, where τ is the molecular correlation time and ω the Larmor frequency.

an increase in T_2 with temperature has been observed. In tissue, however, the T_2 is reduced and T_2 dependence might by masked by other factors (Rieke and Butts-Pauly, 2008b).

Yet in recent years Baron has successfully measured fat T_2 (and fat-water tissue T_2) to monitor the temperature in adipose porcine, human breast and after focused ultrasound treatment of uterine fibroids in the subcutaneous tissue. As for T_1 based MR thermometry, Equation 2.56 can also be used for T_2 temperature measurements for small temperature changes. For the temperature range from 25°C to 65°C Baron et al. modelled T_2 using a mono-exponential function.

$$T_2 = Ae^{-\frac{B}{T}} \tag{2.57}$$

Where A and B are constants and T is the absolute tissue temperature.

In the range from 25°C to 45°C at 1.5 T in ex vivo adipose porcine tissue Baron et al. determined the fat T_2 temperature dependence to approximately 5 ms/°C. In the ex vivo breast tissue, the temperature sensitivity varied from approximately 3.7 ms/°C at 25°C to roughly 8 ms/°C at 65°C.[52] Still, scan time is an issue, since, for the same resolution, quantitative T_2 mapping methods require significantly more scan time than MR phase maps for PRF-based MR thermometry (Baron et al., 2014b, 2015).

T_2 based MR thermometry in frozen tissue is also possible. T_2 and T_2^* in frozen tissue are usually very short, still T_2 and T_2^* increase with increasing temperature (Belton et al., 1972; Kaye et al., 2010).

2.3.4 Proton Resonance Frequency change

The proton resonance frequency (PRF) shift method is based on the change of resonance frequency of the water protons with temperature. As explained in Section 2.1.5 on chemical shift, the resonance frequency of protons is influenced by their local chemical environment via altering the magnetic field B_{loc} at the site of the proton. In water, the chemical shift of protons is temperature dependent since the fraction and nature of hydrogen bonds changes with temperature. With increasing temperature, the water molecules spend less time in the hydrogen-bonded state, and the electronic screening of the water protons increases causing a decrease in water PRF. Section 2.1.5 describes hydrogen bonding in water (p. 32) and the resulting temperature dependent chemical shift (p. 34).

PRF exhibits no hysteresis when tissue returns to its initial temperature after heating or cooling and is insensitive to coagulation (De Poorter et al., 1995; Rieke and Butts-Pauly, 2008b). Furthermore, the thermal PRF change coefficient is relatively independent of tissue type (McDannold, 2005).

[52] The measured T_2 values were approximately 140 ms, 250 ms and 350 ms at 25°C, 45°C and 65°C respectively.

Hindman measured the change of the water proton chemical shift with temperature and found an almost linear relation for the thermal PRF change coefficient α from -20°C to 100°C:

$$\alpha = -0.0103\,\text{ppm/K} \tag{2.58}$$

The temperature induced frequency shift can be expressed as an additional relative chemical shift δ_{Temp}:

$$\delta_{Temp} = \alpha \cdot \Delta T \tag{2.59}$$

δ_{Temp} is the chemical shift relative to the PRF at the reference temperature $T(t_0)$.[53] With Eq. 2.33 the change in frequency $\Delta f = f(t) - f(t_0)$ can then be expressed as:

$$\Delta f = \delta_{Temp} \cdot f_0 \qquad \rightarrow \qquad \Delta f = \alpha \Delta T \cdot f_0 \tag{2.60}$$

and therefore the change in temperature ΔT is:

$$\Delta T = \frac{\Delta f}{\alpha f_0} \tag{2.61}$$

By contrast, many other protons (typically in compounds with CH bonds) giving a resonance line in NMR spectra are not involved in hydrogen bonds. Their resonance frequencies have much smaller temperature dependence and need to be discarded for PRF-based MR thermometry (Kuroda et al., 1997). Alternatively, if these resonances are sufficiently distinct from the water proton resonant frequency, such compounds can provide a temperature-independent reference to correct for errors in PRF-based MR thermometry (Ishihara et al., 1995). Fat is often used as a PRF reference substance since it is common in the human body and the fat PRF is in the range of interest independent of temperature (De Poorter, 1995).

Temperature measurements using the PRF shift is mainly done in two ways, by measuring the spectrum of the tissue or by phase mapping methods.

PRF MR Phase Thermometry

An intriguing way to make this subtle change of -3 Hz per K at a Larmor frequency of $3 \cdot 10^8$ Hz (at 7 T) visible is by looking at the direction of the net magnetisation in the transverse plane at a certain time.[54] Ishihara et al. was the first to do phase MR temperature mapping in 1995.[55]

The sensitivity originates from the cumulative phase shift of the magnetisation for off-resonance water protons over time before the acquisition of the centre of k-space

[53] $\Delta T = T(t) - T(t_0)$.

[54] The MR scanner is set to the weighted average tissue frequency. Therefore the measured signal is already demodulated, and only the frequency difference between the averaged and the position dependent frequency contributes to the MR phase.

[55] Interestingly Ishihara et al. also used an asymmetric spin-echo sequence to measure the phase change, as it is done in this work in Chapter 5.

($k_{Read} = 0$) at the echo time TE:[56]

$$\varphi = 2\pi f \cdot TE \tag{2.62}$$

Since MR phase varies spatially not the absolute phase φ can directly be used to calculate the temperature, but instead the change in phase $\Delta\varphi(t) = \varphi(t) - \varphi(t_0)$ is used to determine the change in PRF:[57]

$$\Delta\varphi(t) = 2\pi\Delta f(t) \cdot TE \tag{2.63}$$

So, for basic MR thermometry, a reference or baseline MR phase map $\varphi(x, y, z, t_0)$ is acquired before the session, providing a phase offset at each imaged position. Substituting $\Delta f(t)$ using Eq. 2.60 gives the change in temperature $\Delta T(t)$:

$$\Delta\varphi(t) = 2\pi \cdot \alpha\Delta T(t) f_0 \cdot TE \qquad \rightarrow \qquad \Delta T(t) = \frac{\Delta\varphi(t)}{2\pi\alpha TE f_0} \tag{2.64}$$

This basic MR thermometry method of just acquiring a reference or baseline MR phase map at the beginning requires the MR phase change to be purely caused by a change in temperature. However, the varying magnetic field is the chief source of error in MR phase thermometry. Field fluctuations are, for example, caused by B_0 field drift, tissue movement or, susceptibility changes and the phase can change due to heat induced electric conductivity changes of the tissue (Foerster et al., 2005; Kickhefel et al., 2012; Maier et al., 2012; Peters et al., 2009; Peters and Henkelman, 2000; Raj et al., 2000; Sprinkhuizen et al., 2010b; Streicher et al., 2012; van Gelderen et al., 2007).

An excellent method of estimating the reference phase map are the so-called referenceless methods. No reference map needs to be acquired, but instead, a 2D function is fitted in areas of no expected temperature change and interpolated to areas with temperature change. Techniques vary on the type of functions that are used for the fit and the weighting procedure (Grissom et al., 2010b; Salomir et al., 2012; Yung et al., 2017). Referenceless methods require an area where no temperature change occurs or where the temperature change is well known. Tissue motion can be corrected for, and the referenceless method has even been adapted to mixtures of adipose and aqueous tissue (de Senneville et al., 2010; Rieke et al., 2007).

The multi-baseline methods acquire a whole library of phase reference maps before heating. Then during heating, the most appropriate reference map is selected. Multi-baseline techniques are especially appropriate for periodic motion like breath-

[56] Optimal MR phase sensitivity is achieved for $TE = T_2^*$ (Yuan et al., 2012).

[57] The measured MR phase of each voxel and channel is a sum of many contributions, such as the spatially varying phase of the transmit coil or receive coils, eddy current and B_0 variations.

ing (Pichardo et al., 2014; Vigen et al., 2003). Changes not encountered during acquisition of the reference library causes difficulties. Grissom et al. tries to solve this by hybrid referenceless and multi-baseline MR thermometry 2010. Rieke et al. (2013) presents a comparison of methods.

Referenced MR thermometry can be applied if distortions are limited and a signal from a reference substance is available in or close to the tissue (De Poorter et al., 1995; Kuroda et al., 1997; Sprinkhuizen et al., 2010a; Streicher et al., 2014; Taylor et al., 2008). The reference substance can make the method sensitive to many non-temperature-related effects that alter the MR phase (Kardoulaki et al., 2016).[58]

The correction is done by acquiring so called reference or baseline maps of water $\varphi_{H_2O}(t_0)$ and the reference substance $\varphi_{ref}(t_0)$, which are then separately used to calculate the phase change of the water $\Delta\varphi_{H_2O}(t)$ and reference substance $\Delta\varphi_{ref}(t)$:[59]

$$\Delta\varphi_{H_2O}(t) = \varphi_{H_2O}(t) - \varphi_{H_2O}(t_0) \quad \text{and} \quad \Delta\varphi_{ref}(t) = \varphi_{ref}(t) - \varphi_{ref}(t_0) \tag{2.65}$$

The reference substance MR phase change $\Delta\varphi_{ref}(t)$ can then be used to correct the water MR phase change $\Delta\varphi_{H_2O}(t)$ by subtraction. Putting the reference corrected water MR phase change $\Delta\varphi_{corr}(t) = \Delta\varphi_{H_2O}(t) - \Delta\varphi_{ref}(t)$ into Equation 2.64 gives the reference corrected temperature change map:

$$\Delta T_{corr}(t) = \frac{\Delta\varphi_{corr}(t)}{2\pi\alpha TE f_0} \tag{2.66}$$

The usual water thermal PRF change coefficient α (see Eq. 2.58) can be applied to fat referenced MR thermometry since the fat thermal PRF change coefficient is negligible (De Poorter, 1995). If Dimethyl sulfoxide (DMSO) is employed the relative thermal PRF change coefficient of the water-DMSO solution has to be applied, as done in Section 5.1.2.

How the images of the eight separate coil elements are combined to achieve high SNR is described in Section 5.1.3 on page 104.

Spectroscopic Imaging of the PRF shift

Cady et al. measured absolute temperature in the brain using MR spectroscopy and N-actyl-aspartate as a reference (Cady et al., 1995). Spectroscopic data at relatively high spatial and temporal resolution can be acquired using multi-echo GRE sequences.[60] Instead of acquiring just one line in k-space after excitation, the same

[58] On the limitations of the used referenced MR thermometry techniques see the Discussion (Section 5.3) and the Conclusion (Chapter 6).

[59] To determine usable phase changes, the MR time series images might have to get registered onto each other.

[60] The multi-echo readout can by prepared by different RF pulses. Taylor et al. used a single excitation pulse while the LSEPSI sequence uses an excitation and refocusing pulse to excite a

line in k-space is acquired several times after the excitation with different echo times. A realistic spectrum for each voxel can be generated if the number and spacing of echoes are high enough (Brown et al., 1982; Kuroda et al., 2003; Labadie et al., 2013).[61] The Fourier transform over the different echo times generates the spectrum for each voxel.

In the case, when a few proton frequencies dominate the spectrum, the signal can either be fitted by Lorentzian peaks in the frequency domain or by exponential decay functions in the time domain. Linear superposition of the individual chemical species allows to model the complex MR signal in time. This can be done in tissue contain fat:

$$S(t)_{rot} = C_{H_2O} \cdot e^{-\left(i2\pi \cdot f_{H_2O} + 1/T_{2\,H_2O}^*\right)\cdot t} + C_{fat} \cdot e^{-\left(i2\pi \cdot f_{fat} + 1/T_{2\,fat}^*\right)\cdot t} \tag{2.67}$$

where C are the signal amplitudes, f the frequencies and T_2^* the relaxation rates of the water (H_2O) and fat component (Soher et al., 2010; Wyatt et al., 2011).[62]

Taylor et al. acquired 16 equally spaced echoes to fit the complex signal in the time domain applying an autoregressive moving average technique for low-resolution spectral data (Taylor et al., 2009). McDannold et al. acquired 32 echoes with the line scanning spectroscopy sequence LSEPSI and fitted two Lorentzian curves to the water/fat data (McDannold et al., 2007).[63] For more information see ''Non-invasive MR thermography using the water proton chemical shift'' (Kuroda, 2005; Kuroda et al., 2003).

Effects of pH on PRF MR thermometry

Intra- and extracellular pH in mammalian tissue is highly regulated in a robust dynamic steady state. However, in many pathological states, this state is altered. For example, in cancer where the extracellular pH in tumours is acidic (Gillies et al., 2004). Additionally, pH in water decreases naturally with increasing temperature.[64,65] Therefore, the effect of tissue pH on MR thermometry should be known. Based on numerous studies, the effect of the pH on the offset and linear dependence of PRF on temperature is small, if not completely negligible at least for the physiologically relevant pH values, and the error should be on the order of 1-2 % (Ackerman et al., 1981; Cady et al., 1995; Coman et al., 2009; Corbett et al., 1995; Gillies et al., 2004;

single column, while a stimulated echo preparation would also be possible (Frahm et al., 1985).

[61] As for the image reconstruction by Fourier transform, the resolution of the spectrum is given by the longest echo time TE_{max} and the width of the spectrum by the echo spacing. See Section 2.2.3 for further details.

[62] Here, just the main peak $(CH_2)_m$ approximates the fat spectrum. For the complete proton spectrum of fat, see Figure 5.18.

[63] When echoes are acquired with alternating gradient polarity an extra post-processing step similar to the EPI (see Section 2.2.3) corrections might be required (see Taylor2008).

[64] The reason for the decrease of pH of water is similar to the origin of the water proton frequency shift. As the temperature increases, the average number of broken water-proton bonds increases.

[65] Most biological buffer solutions have a negative temperature coefficient. Therefore, the overall pH in biological tissue should also decrease with temperature.

Hall and Talagala, 1985; Hashim et al., 2011; Kuroda, 2007; Lutz et al., 1993).[66]

2.4 Fat Suppression Techniques

This section is mainly named 'Fat Suppression Techniques' because the main use of the described techniques is to suppress fat during water imaging. It should rather be called MRI active substance selective techniques. The techniques described here can suppress substances due to their T_1 relaxation rate and alternatively, can suppress or select substances due to their chemical shift.

As mentioned before, the PRF of fat is not temperature sensitive, and the PRF of DMSO has a different temperature sensitivity than water. Thus the sensitivity of MR phase to temperature changes is altered in voxel containing water and fat (or DMSO) depending on the signal ratio.[67] Strategies to cope with this problem are fat suppression, water/fat selective excitation and water-fat separation.

2.4.1 Water/Fat Imaging Methods

Good reviews on the subject are by Bley et al. 2010 and Del Grande et al. 2014.[68]

Water and fat can be separated based on their different T_1 relaxation times, called short TI inversion recovery (STIR).[69] Either a global or spectral selective inversion pulse is applied, and the wanted signal is excited with another excitation pulse at the time when the unwanted signal passes through zero, i.e. has zero magnetisation along the longitudinal axis (Borman et al., 2016; Bydder and Young, 1985; Bydder et al., 1985). By using (non-spectral) adiabatic inversion pulses this sequence is very robust with regard to B_0 and B_1 inhomogeneities, but at high field requires rather long scan times.

The chemical shift based techniques take advantage of the different chemical shifts of, for example, water and fat or DMSO. Water-fat separation can be done during image reconstruction using the Dixon method. In general, the various Dixon methods acquire several images at different echo times to reconstruct water and fat images (Reeder et al., 2004). The simplest is by just acquiring two images where fat and water are once in-phase and once with opposite phase (Dixon, 1984). An extension to the Dixon method is the linear superposition approach described in Section 2.3.4. Several echoes have to be acquired with, ideally, optimal spacing. Therefore these sequences cannot simply be used as a single shot method. The

[66] Physiologically relevant pH values range from 5.5 to 8.0.

[67] The offset in fat susceptibility and its temperature dependence can additionally corrupt the water and fat phase even when chemical selective imaging techniques are employed. This challenge is discussed later.

[68] Of course, hybrid methods combining two more basic methods, described here, have also been developed, but these hybrid methods are not discussed here.

[69] The inversion time TI is the time between the inversion RF pulse and the excitation RF pulse used for imaging.

multi-echo approaches are B_1 and fairly B_0 insensitive and acquire the water and the fat image simultaneously (Todd et al., 2014).

A simpler method is the chemical shift selective (CHESS); here the unwanted magnetisation is saturated. CHESS uses a frequency-selective excitation pulse, set to the unwanted PRF frequency, with a flip angle of 90° followed by a dephasing gradient. Immediately afterwards the wanted species can be imaged (Borman et al., 2016; Haase et al., 1985). Saturation techniques are fast but relatively sensitive to B_0 and B_1 inhomogeneities.

The probably most elegant methods are spectral-spatial excitation pulses that only excite a certain frequency band and at a certain spatial location. Therefore making it possible to image water or fat and leave the other species magnetisation along the longitudinal axis (Boulant et al., 2015; Grissom et al., 2009; Meyer et al., 1990). The simpler spectral-spatial pulses apply a series of RF pulses with binomial weighting while applying a constant slice select gradient (with rephase gradients after each RF pulse). The probably simplest spectral-spatial excitation pulse is made up of two slice select RF pulses of 45° flip angle. The first RF pulse tips the water and fat magnetisation equally by 45°. The second 45° RF pulse is applied when the water and fat magnetisation are out-of-phase, rotating the water magnetisation into the transverse plane and the fat magnetisation back along the longitudinal axis (Schick et al., 1997).[70] Spectral-spatial RF pulses are B_0 sensitive, and require more time than simple slice-selective pulses, but are insensitive to B_1 inhomogeneities.

Bley et al. (2010) and Del Grande et al. (2014) both miss mentioning the spin-echo chemical shift selective techniques used in this work.

2.4.2 Spin-Echo Frequency-selective Sequences

Historically the chemical shift selective gradient reversal spin-echo (GR SE) imaging technique was first (Gomori et al., 1988; Park et al., 1987; Volk et al., 1987). Much later, my colleague Dr. Dimo Ivanov came up with principally the same technique, but with gradients of the same polarity for excitation and refocusing (Ivanov et al., 2010). Both techniques are based on the fact that the excited and refocused slices of chemically shifted species are also shifted in space. If the excitation and the refocusing slice of the unwanted species do not overlap in space, then no observable transverse magnetisation of the unwanted species is generated.

Water and fat protons precess at slightly different frequencies in a magnetic field, due to their chemical shift difference.[71] When a slice-selective RF pulse with its corresponding gradient is applied a water, and a fat slice at different positions are manipulated. Combining equation 2.32 for the chemically shifted local magnetic

[70] The simple 45°-τ-45° binomial pulse has a very smooth frequency response. Imaging the frequency offsets $\Delta f = 0, 1/\tau, 2/\tau, ...$ and suppressing $\Delta f = 1/2\tau, 3/2\tau, 5/2\tau, ...$ Higher binomial series coefficients achieve sharper frequency responses.

[71] The same applies for DMSO. However, for this discussion, fat is used representative for any substance chemically shifted relative to water.

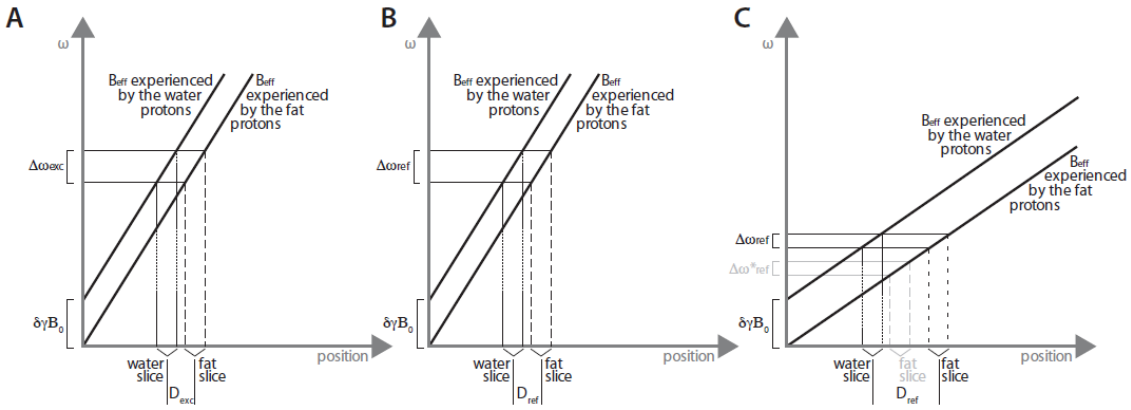

Figure 2.8: *Illustration of the fat suppression technique introduced by Ivanov et al. The scanner frequency is set to the water PRF. The x-axis depicts the position in space, the y-axis the PRF frequency. Water and fat PRFs differ by $\delta\gamma B_0$ at the same position. (A) During slice excitation, the MR scanner plays out an RF pulse and a slice-select gradient simultaneously. The excitation RF pulse has a frequency bandwidth of $\Delta\omega_{\text{exc}}$. Due to the chemical shift difference and dependent on the gradient amplitude the fat slice is shifted by D_{exc} in space. (B) For a conventional spin-echo sequence, the refocusing RF pulse frequency bandwidth and gradient amplitude are similar to the values during excitation. Due to the same gradient and bandwidth, the refocused fat slice is at the same position as the excited fat slice, i.e. $D_{\text{ref}} = D_{\text{exc}}$. The excited water and fat slice are both refocused and contribute to the signal during image acquisition. (C) The Ivanov method changes the bandwidth $\Delta\omega_{\text{ref}}$ of the refocusing RF pulse and the gradient amplitude G_{exc} in such a way that the fat slice that gets refocused does not overlap with the excited fat slice, i.e. $D_{\text{ref}} > D_{\text{exc}}$. No fat magnetisation contributes to the signal acquisition since the transverse magnetisation is dephased by the slice select and crusher gradients of the refocusing RF pulse (Bernstein et al., 2004). Since the scanner frequency is set to the water frequency, the refocused slice of water is at the same spatial location as the excited water slice. See also Figure 5.15, depicting the fat magnetisation during a spin echo selective excitation on the water frequency and Figure 2.17 for the on resonant species. Image from Ivanov et al. 2010.*

field change and equation 2.36 for the frequency difference due to a difference in position D along a gradient, one gets:

$$D = \frac{B_0 \cdot \delta_{rel}}{G} \tag{2.68}$$

where δ_{rel} is the chemical shift between water and fat. Figure 2.8 depicts the situation in case of excitation and refocusing gradients of equal polarity, i.e. the Ivanov method (IV SE). If the scanner frequency is set to the water frequency, then the water slice is manipulated exactly at the desired position and the fat slice is displaced by D.[72] Slice-selective RF pulses can be described by the dimensionless bandwidth-time

[72] Assuming a homogeneous B_0 field and a perfectly linear gradient field.

product P:

$$P = \Delta\omega \cdot \tau \tag{2.69}$$

where $\Delta\omega$ is the frequency bandwidth that the RF pulse effectively manipulates and τ the RF pulse duration. By Eq. 2.36 and 2.69 above, the relation for the slice thickness d holds (Bernstein et al., 2004):[73]

$$d = \frac{P}{\gamma G \cdot \tau} \tag{2.70}$$

To achieve fat suppression for a spin echo sequence, the excitation and refocusing slice of fat must not overlap:

$$|D_{exc} - D_{ref}| \geq \frac{|d_{exc}|}{2} + \frac{|d_{ref}|}{2} \tag{2.71}$$

where d_{exc} and d_{ref} are the slice thicknesses of the excited and refocused slice, respectively. For the gradient reversal technique Equation 2.71 can be rearranged to:

$$\text{GR SE}: \quad \gamma G d = \frac{P}{\tau} \leq 2\gamma B_0 \left|\delta_{rel}\right| \tag{2.72}$$

under the condition of equal slice thicknesses and bandwidth-time products of the excitation and refocusing RF pulses and therefore also equal RF durations. And for the Ivanov method under the conditions of equal slice thickness and slice displacement $D_{ref} > D_{exc} > 0$:

$$\text{IV SE}: \quad \gamma G_{rel} d = \frac{P_{rel}}{\tau_{rel}} \leq \frac{\gamma G_{exc} \tau_{exc} \cdot d \cdot \gamma B_0 \left|\delta_{rel}\right|}{P_{exc} + \gamma B_0 \left|\delta_{rel}\right| \cdot \tau_{exc}} \tag{2.73}$$

The assumption of $D_{ref} > D_{exc}$ is in general useful to reduce SAR. The larger displacement D_{ref} implies a smaller slice select gradient G_{ref} which in turn implies a longer pulse duration τ_{ref}. SAR scales inverse quadratically with τ (see Section 2.6 on RF Heating and SAR).

2.5 Electric Properties of Matter

In this section the behaviour of linear, isotropic and homogeneous matter in electric fields is discussed. Linear and isotropic means, that the response of the system is along the direction of the applied force and the response of the system on two disturbances is equal to the sum of the two individual reactions. Homogeneous means, that the response of the system is independent of position. This is usually the case for the electromagnetic (EM) field strengths and tissues of interest in MRI. First, the origin of the complex and frequency-dependent electric permittivity in insulators is briefly described, followed by a discussion of conductivity due to mobile

[73] Instead of bandwidth-time product Bernstein et al. calls it time-bandwidth product.

charge carriers, and the resulting electromagnetic behaviour of tissue (Hayt and Buck, 2011; Jackson, 1998; Raistrick et al., 2005).

Magnetic susceptibility μ is the main source of B_0 field inhomogeneities in MRI (on the order of 10^{-6}), causing distortions and artefacts. However, the magnetic susceptibility is negligible when describing the RF fields in MRI. Here, the electric permittivity ε and conductivity σ dominate giving rise to perturbations on the order of the applied field itself (Collins, 2006).

2.5.1 Dielectric Relaxation

'It is a familiar fact that the dielectric constants of many liquids and solids depend markedly on the frequency of measurement' (Cole and Cole, 1941). The dependence is in general found to be a decrease from a static value ε_s at low frequencies to a smaller limiting value ε_∞ at higher frequencies. In the transition region of anomalous dispersion there is an 'absorption conductivity' and the situation may be described in terms of a complex dielectric constant $\varepsilon^* = \varepsilon' - i\varepsilon''$ (Cole and Cole, 1941).

When an electric field $\boldsymbol{E}$ is applied to a material, bound charges of the constituent atoms are displaced, inducing a local electric dipole moment.[74] The sum over these local electric dipoles leads to the macroscopic polarization $\boldsymbol{P}$, which is proportional to $\boldsymbol{E}$ for linear materials:

$$\boldsymbol{P} = \varepsilon_0 \chi_e \boldsymbol{E} \tag{2.74}$$

with the dielectric susceptibility χ_e. The induced macroscopic polarization leads to a displacement current which establishes an electric displacement $\boldsymbol{D}$. The electric displacement is defined as,

$$\boldsymbol{D} = \varepsilon_0 \boldsymbol{E} + \boldsymbol{P} = \varepsilon_0 \boldsymbol{E} + \varepsilon_0 \chi_e \boldsymbol{E} = (1 + \chi_e)\, \varepsilon_0 \boldsymbol{E} = \varepsilon_0 \varepsilon_r \boldsymbol{E} \tag{2.75}$$

with the permittivity of free space $\varepsilon_0 = 8.854 \cdot 10^{-12} F/m$ and the definition of the relative permittivity:

$$\varepsilon_r = 1 + \chi_e \tag{2.76}$$

Due to the linear response of the material to the applied electric field, the polarization is proportional to the electric field. Additionally, the resulting polarization response is dependent on time and can be divided according to the time constants of their response. An almost instantaneous polarization caused by the displacement of bound electrons, with a time constant of approximately $10^{-16} s$, defines the high-frequency dielectric permittivity (Raistrick et al., 2005). Slower time-dependent polarizations which are caused by the re-orientation of dipoles in the electric field or by atomic polarization and the bound electrons determine the static low frequency dielectric permittivity. In the effort to describe the frequency-dependence of the dielectric relative permittivity $\varepsilon_r(f)$ Debye introduced the concept of dipole relax-

[74] For this derivation, the assumption of no free charge carriers applies. Section 2.5.2 describes how free charges can be incorporated into the theory of dielectric relaxation.

ation in 1912 (Debye, 1929). This approach of treating a dielectric material as a collection of independent dipoles floating in a viscous non-polar liquid gives results which are in excellent agreement with measurements of many substances, like water and DMSO (Gregory et al., 2009; Kaatze, 1997; Raistrick et al., 2005).[75]

Debye Relaxation

Debye developed a model for the frequency dependence of the complex permittivity $\varepsilon_r(f)$ based on the assumption of a single relaxation process of dipole re-orientation when an electric field is applied. [76] Additionally, Debye assumed that this relaxation to an equilibrium polarization is exponential with a single relaxation time τ, resulting in:

$$\varepsilon_r(f) = \varepsilon_\infty + \frac{\varepsilon_s - \varepsilon_\infty}{1 + i2\pi f\tau} \tag{2.77}$$

with ε_s and ε_∞ being the real valued low and high frequency limit of the permittivity ε_r. Defining the real ε' and imaginary ε'' dielectric permittivity as:

$$\varepsilon_r(f) = \varepsilon'(f) - i\varepsilon''(f) \tag{2.78}$$

gives,

$$\varepsilon'(f) = \varepsilon_\infty + \frac{\varepsilon_s - \varepsilon_\infty}{1 + (i2\pi f\tau)^2} \quad \text{and} \quad \varepsilon''(f) = \frac{(\varepsilon_s - \varepsilon_\infty)(i2\pi f\tau)}{1 + (i2\pi f\tau)^2}. \tag{2.79}$$

The behaviour of the real and imaginary part of the permittivity with frequency can be nicely seen in a log-plot.[77] In Figure 2.9 the Debye model for pure water at a temperature of 20°C is plotted. Additional relaxation mechanisms like the fast displacement of bound electrons can simply be added if necessary. For water, a single loss process at approximately 17 GHz (at 20°C)[78] is sufficient to describe $\varepsilon_r(f)$ up to 300 GHz (Kaatze, 1997).

There is another way of plotting the dielectric permittivity, named Cole-Cole plot, after the two brothers Kenneth and Robert Cole (Cole, 1932; Cole and Cole, 1941). They recommended to do a parametric plot of $\varepsilon''(f)$ vs. $\varepsilon'(f)$ (Figure 2.10), which results in a perfect half circle for the Debye model.[79]

Combining equations 2.74, 2.75, 2.76 and 2.78 it becomes clear what the real and

[75] Dimethyl sulfoxide (DMSO) is frequently used in NMR as a solvent. In this work it was used as a reference substance for the MR temperature measurements (see Section 5.1.2).

[76] The relaxation process is called resonance, relaxation or loss process. See also Clarke et al. (Clarke et al., 2003).

[77] The real and imaginary permittivity are not independent, but connected via the complex dielectric susceptibility which satisfies the Kramers-Kronig relation (Jackson, 1998).

[78] The frequency of the loss process strongly depends on temperature, i.e. from 9 GHz at 0°C to 40 GHz at 60°C.

[79] Slight deviations from the Debye model of real substance can be more easily seen in the Cole-Cole plot, i.e. water/DMSO substances used for the temperature phantoms (see Equation 2.89).

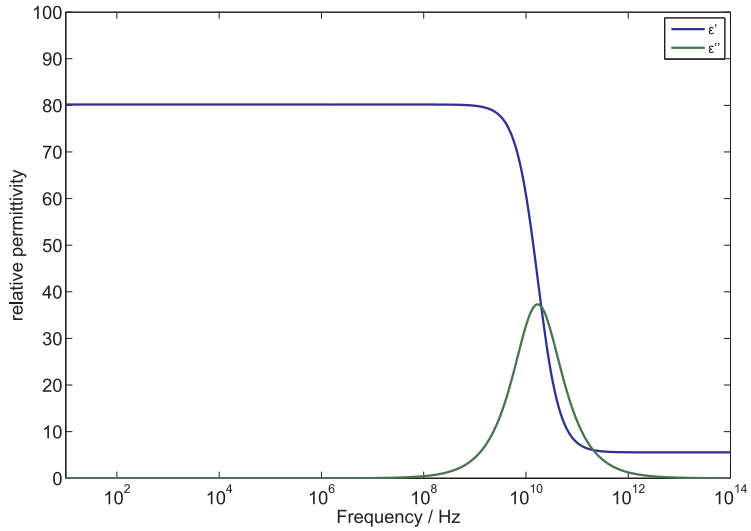

Figure 2.9: *The Debye model for the dielectric spectrum of water at 20°C, with* $\varepsilon_s = 80.2 \pm 0.4$, $\varepsilon_\infty = 5.5 \pm 0.3$, *and* $\tau = (9.4 \pm 1.0)\,ps$ *(Kaatze, 1997). The resonance occurs at* $1/(2\pi\tau)$, *here at approximately 17 GHz.* ε' *drops by* $\Delta\varepsilon = \varepsilon_s - \varepsilon_\infty = 74.7 \pm 0.5$, *in the vicinity of the resonance.*

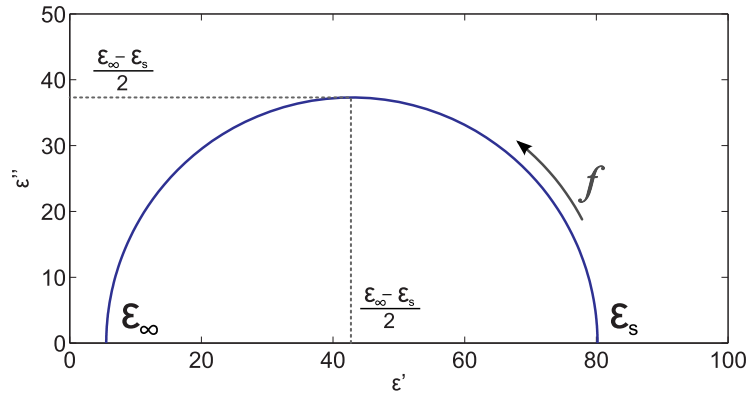

Figure 2.10: *Cole-Cole plot of water using the same parameters as in Figure 2.9.* $\varepsilon''(f)$ *vs.* $\varepsilon'(f)$ *describes a perfect half-circle for the Debye model. The parameters describing the circle are given in the plot, with the permittivities going from right to left with increasing frequency.*

imaginary part of the permittivity mean:

$$\boldsymbol{D}(f) = \varepsilon_0 (\varepsilon'(f) - i\varepsilon''(f))\,\boldsymbol{E} \tag{2.80}$$

$$\boldsymbol{P}(f) = \varepsilon_0 (\varepsilon'(f) - 1 - i\varepsilon''(f))\,\boldsymbol{E}. \tag{2.81}$$

ε' determines the part of $\boldsymbol{D}$ and $\boldsymbol{P}$ which is parallel to $\boldsymbol{E}$, while ε'' determines the part of $\boldsymbol{D}$ and $\boldsymbol{P}$ which is perpendicular to $\boldsymbol{E}$ and lags behind.

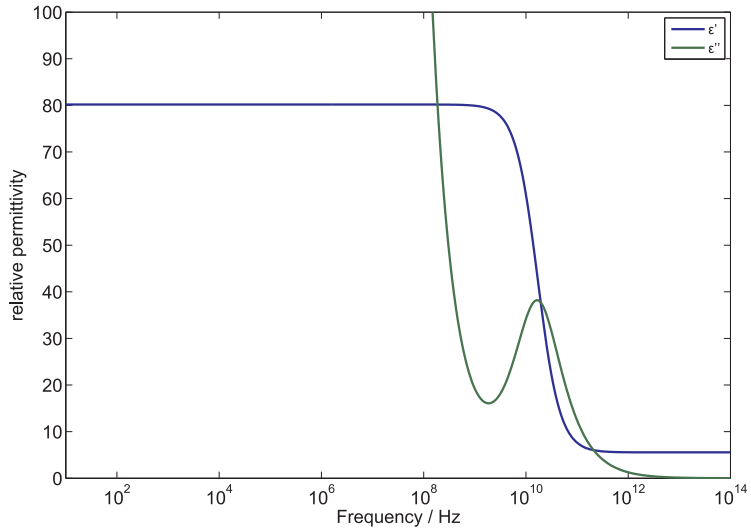

Figure 2.11: *The Debye model for the dielectric spectrum of an aqueous NaCl solution at 20°C. Assuming unchanged relaxation variables ε_s, ε_∞, and τ (cf. Figure 2.9) and a dc conductivity of $\sigma_{dc} = (0.83 \pm 0.01)\, S/m$ (Buchner et al., 1999; Nörtemann et al., 1997).*

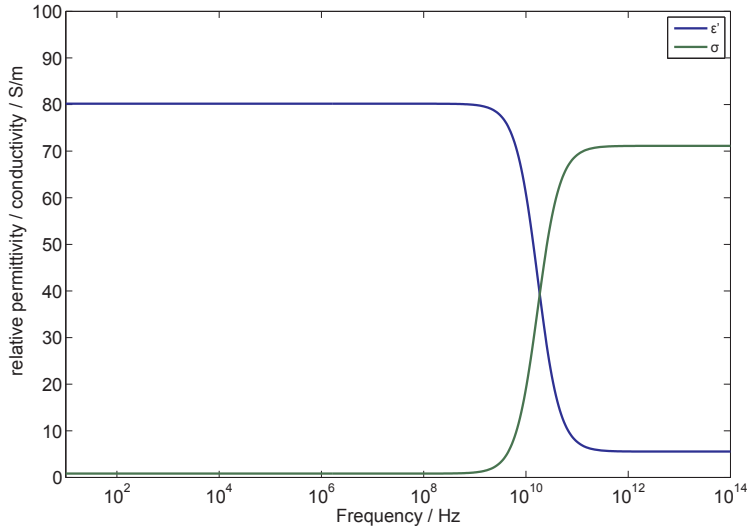

Figure 2.12: *The same dielectric spectrum as in Figure 2.11, but with the conductivity in S/m, instead of ε'' (see Equation 2.87). The aqueous NaCl solution has a dc conductivity of $\sigma_{dc} = (0.83 \pm 0.01)\, S/m$ at 20°C (Buchner et al., 1999; Nörtemann et al., 1997).*

2.5.2 Direct Current (dc) Conductivity

Up to now only bound charges without any dc conductivity were considered. However, if there are mobile charge carriers in the material (e.g. ionic substances dissolved in a liquid), the current density $\boldsymbol{J}$ is proportional to $\boldsymbol{E}$ and the conductivity σ_{dc}:[80]

$$\boldsymbol{J} = \sigma_{dc}\boldsymbol{E} \tag{2.82}$$

[80] The dc conductivity σ_{dc} is a real number

which is called Ohm's law. Ampere's law of Maxwell's equations is:

$$\nabla \times \boldsymbol{H} = \boldsymbol{J}_f + \frac{\partial \boldsymbol{D}}{\partial t}. \tag{2.83}$$

Putting Equation 2.75 and 2.82 into Ampere's law and assuming a harmonic oscillating $\boldsymbol{E}$ field one gets (Jackson, 1998):[81]

$$\begin{aligned} \nabla \times \boldsymbol{H}(f) &= \sigma_{dc}\boldsymbol{E}(f) + i2\pi f\varepsilon_0\varepsilon_r(f)\boldsymbol{E}(f) \\ &= i2\pi f\varepsilon_0\varepsilon_{\mathit{eff}}(f)\boldsymbol{E}(f) \end{aligned} \tag{2.84}$$

Defining an effective complex relative permittivity $\varepsilon_{\mathit{eff}}(f)$ as,

$$\begin{aligned} \varepsilon_{\mathit{eff}}(f) &= \varepsilon(f) - i\frac{\sigma_{dc}}{2\pi f\varepsilon_0} \\ &= \varepsilon'(f) - i\left(\varepsilon''(f) + \frac{\sigma_{dc}}{2\pi f\varepsilon_0}\right) \end{aligned} \tag{2.85}$$

with the effective imaginary permittivity:

$$\varepsilon''_{\mathit{eff}}(f) = \varepsilon''(f) + \frac{\sigma_{dc}}{2\pi f\varepsilon_0} \tag{2.86}$$

resulting in an effective conductivity:

$$\sigma_{\mathit{eff}} = 2\pi f\varepsilon_0\varepsilon'' + \sigma_{dc} \tag{2.87}$$

Equation 2.85 demonstrates that the dc conductivity adds to the imaginary part of the permittivity. Furthermore, it is obvious that the σ_{dc} term dominates for low frequencies and gets negligible for higher frequencies. In Figure 2.11 the Debye model for a 5 g per litre aqueous NaCl solution at a temperature of 20°C is plotted. The Debye model with unchanged relaxation parameters plus the σ_{dc} term of Equation 2.85 still provides a good fit for aqueous NaCl solutions of this concentration (Buchner et al., 1999; Nörtemann et al., 1997).[82] In Figure 2.12 the effective conductivity σ_{eff} (Eq. 2.87) instead of the imaginary dielectric permittivity ε'' is plotted. The dc conductivity of the NaCl ions just causes a constant offset across the frequency range, which is much smaller than the contribution of the relaxation process at 17 GHz.

2.5.3 Dielectric Properties of Body Tissue

Gabriel et al. did an extensive literature survey on dielectric properties of human tissue (Gabriel et al., 1996a; Gabriel et al., 1996b; Gabriel et al., 1996c). The spectra from 10 Hz to 100 GHz were empirically modelled by four dispersion regions

[81] The electric field oscillating with frequency f: $\boldsymbol{E}(\boldsymbol{r},t) = Re\left[\boldsymbol{E}(\boldsymbol{r})\,e^{i2\pi ft}\right]$

[82] The dc conductivity was obtained by fitting the Debye-Huckel-Onsager equation to tabulated values ("3.9.2 Conductivities" 2005).

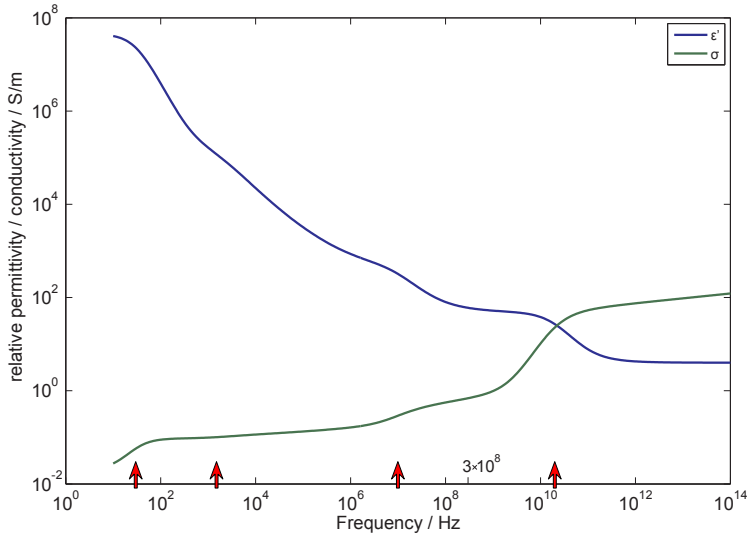

Figure 2.13: *The dielectric spectrum of human brain grey matter at 37°C (conductivity in S/m). The four dispersion frequencies are marked by the red arrows. At 7 Tesla or 297.22 MHz $\varepsilon' = 60.1$ and $\sigma = 0.69$ S/m. The white matter dielectric spectrum is similar with a slightly reduced conductivity (Gabriel et al., 1996a).*

plus an ionic dc conductivity term. Broadening of the dispersions were empirically accounted for by introducing the distribution parameter α, thus changing the Debye equation to the Cole–Cole equation where α is a measure of the broadening of the dispersion (Cole and Cole, 1941).[83]

$$\varepsilon_r(f) = \varepsilon_\infty + \sum_n \frac{\Delta\varepsilon_n}{1 + (i2\pi f\tau_n)^{(1-\alpha_n)}} + \frac{\sigma}{i2\pi f\varepsilon_0} \tag{2.88}$$

The dielectric spectrum of human grey matter up to 10^{14} Hz is plotted in Figure 2.13. The static dielectric permittivity in grey matter reaches an extremely high value of $\varepsilon_r = 4.07 \cdot 10^7$ in comparison to pure water with $\varepsilon_r = 74.2 \pm 0.4$ at 37°C. A comparison of grey (GM) and white matter (WM) conductivity in the frequency range of interest to MRI is shown in Figure 2.14.

2.5.4 Phantom Dielectric Properties

The dielectric properties of water and DMSO mixtures for a large range of frequencies (1 MHz to 40 GHz) and concentrations have been extensively studied by Kaatze et al. and Lu et al. (Kaatze et al., 1989; Lu et al., 2009). Kaatze et al. fitted the Davidson-Cole equation to the measured permittivities for the different mole fractions:

$$\varepsilon(f) = \varepsilon_\infty + \frac{\varepsilon_s - \varepsilon_\infty}{(1 + i2\pi f\tau)^{1-\beta}} \tag{2.89}$$

[83]The subscript for the effective permittivity ε_{eff} of Section 2.5.2 is dropped to avoid confusion. However Section 2.5.2 is still valid and ε'' can simply be substituted by ε''_{eff}.

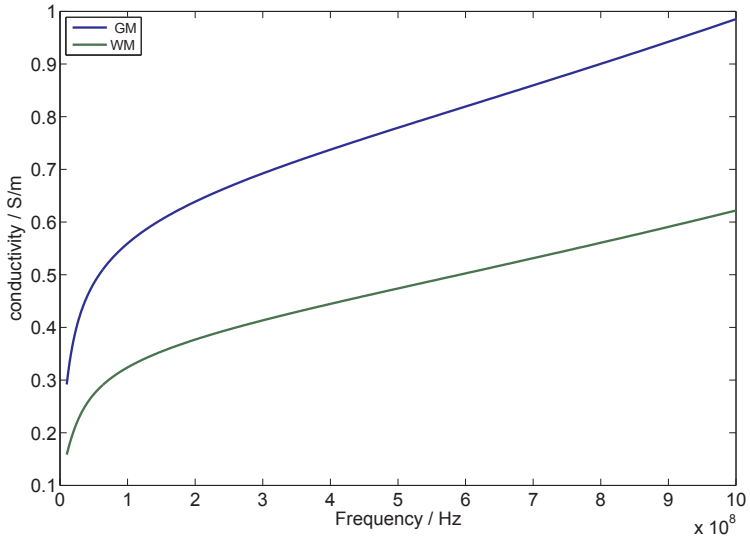

Figure 2.14: *The conductivity of human brain grey (GM) and white matter (WM) at 37°C in the range from 10 MHz to 1 GHz, the frequency range of interest in human MRI (at least for the next decade (Robitaille, 2006)).*

where β is the relaxation time distribution parameter (Davidson and Cole, 1951; Harvey and Prausnitz, 1987). The Davidson-Cole equation is another modification of the Debye equation (Eq. 2.77), different to the Cole-Cole equation (Eq. 2.88). The phantoms used for the RF-heating experiments were made up of 64 % H_2O and 34 % DMSO (DMSO mole fraction X= 0.11, see Section 5.2 on the experiment). The coefficients of the Davidson-Cole equation for pure DMSO, pure Water and for the phantom DMSO mole fraction are shown in table 2.1.

	ε_s	ε_∞	τ/ps	β
H_2O	81.90 ± 0.05	5.78 ± 0.08	9.01 ± 0.02	0
X_{DMSO} =0.11	78.9 ± 1.8	4.1 ± 0.9	29.0 ± 1.6	0.19 ± 0.05
DMSO	48.0 ± 0.6	4.7 ± 1	22.7 ± 0.2	0.11 ± 0.01

Table 2.1: *Davidson-Cole equation coefficients (equation 2.89) for pure DMSO (M_{DMSO}= 78.13 g/mol), pure water (M_{H_2O}= 18.02 g/mol) and a DMSO mole fraction X= 0.11 of the phantom mixture at 20°C from Kaatze et al. and Lu et al. (Kaatze et al., 1989; Lu et al., 2009).*

In another study by Nörtemann, Hilland and Kaatze and in a study by Buchner et al. the complex permittivity of aqueous sodium chloride (NaCl)[84] solutions for NaCl mass fractions ranging from 0 to 0.035 at temperatures from 5 to 35°C were measured (Buchner et al., 1999; Nörtemann et al., 1997). In these publications the dielectric properties of the sodium solutions were described by a Cole-Cole spectral function (Eq. 2.88). However, the distribution parameter of the Cole-Cole model was only 0.04 ± 0.02. Therefore, to estimate the complex relative permittivity of

[84]In this work 'salt' was used synonymously for NaCl.

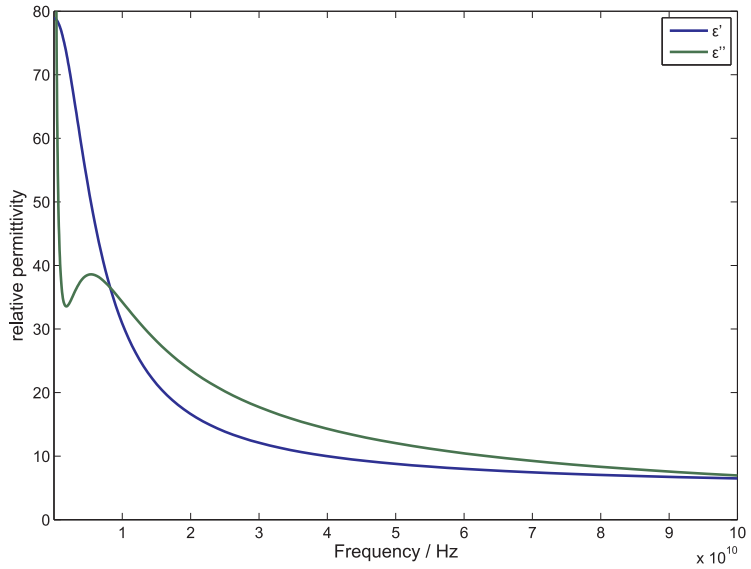

Figure 2.15: *The calculated dielectric spectrum of a water, DMSO and salt solution with a water:DMSO mass ratio of 64:34 at 20°C and a salt ion concentration of 1 %.*

the phantom gels the Davidson-Cole equation (Eq. 2.89) describing the water and DMSO mixture with the ionic term for salt were used (Cole and Cole, 1941):

$$\varepsilon(f) = \varepsilon_\infty + \frac{\varepsilon_s - \varepsilon_\infty}{(1 + i2\pi f\tau)^{1-\beta}} - \frac{i\sigma_{dc}}{2\pi\varepsilon_0 f}. \tag{2.90}$$

As above (Section 2.5.2), the dc conductivity was obtained by fitting the Debye-Huckel-Onsager equation to tabulated values (“3.9.2 Conductivities” 2005). For a NaCl mass fraction of 1 % the dc conductivity was estimated to be $\sigma_{dc} \approx (1.53 \pm 0.2)$ S/m at a temperature of 20°C.[85] The resulting complex relative permittivity spectrum is seen in Figure 2.15.

2.5.5 Wave Propagation in Dielectrics

The analytical treatment is extended to a uniform plane wave in a substance with relative permittivity ε_r, to visualise the effect of a complex relative permittivity on wave propagation. The situation in MRI is more complicated than this. In human MRI the body is not in the far field of the RF coils, except for the travelling wave approach of Brunner et al. (2009). Instead the subject is in the near (especially at high field) or transition region of the RF transmit coils (Roemer et al., 1990). Still it gives some insight on the wave behaviour in MRI to look at plane waves in an isotropic and homogeneous dielectric. The time-independent wave equation, called Helmholtz equation, is

$$\nabla^2 \boldsymbol{E} = -\boldsymbol{k}^2 \boldsymbol{E} \tag{2.91}$$

[85]The NaCl mass fraction is slightly higher than the physiological value to compensate for the larger real part of the permittivity and to reduce the field focusing effect.

where the wavenumber $\boldsymbol{k}$ is in the direction of propagation and is a function of the material properties:

$$|\boldsymbol{k}| = 2\pi f\sqrt{\mu_0\mu_r\varepsilon_0\varepsilon_r} = 2\pi f\sqrt{\mu_0\varepsilon_0}\sqrt{\mu_r\varepsilon_r} \tag{2.92}$$

with the magnetic permeability $\mu_0 = 4\pi\cdot 10^{-6}N/A^{-2}$ and the relative permeability μ_r. A relative permeability of $\mu_r = 1$ is assumed, which is a reasonable approximation for the wave propagation in biological tissue and aqueous solutions (Schenck, 1996). A solution to the Helmholtz equation (Eq. 2.91) is:

$$\boldsymbol{E}(\boldsymbol{r}) = \boldsymbol{E}_0 e^{-i\boldsymbol{k}\boldsymbol{r}}. \tag{2.93}$$

To understand the wave behaviour in the dielectric medium, $|\boldsymbol{k}|$ can be split up into its real and imaginary terms in the following way:

$$i\,|\boldsymbol{k}| = \alpha + i\beta = i\frac{2\pi f}{c_0}\sqrt{\varepsilon' - i\varepsilon''} \quad \rightarrow \quad \boldsymbol{E} = \boldsymbol{E}_0 e^{-\alpha\hat{\boldsymbol{e}}_{\boldsymbol{k}}\boldsymbol{r}} e^{-i\beta\hat{\boldsymbol{e}}_{\boldsymbol{k}}\boldsymbol{r}} \tag{2.94}$$

with the speed of light in vacuum $c_0 = 1/\sqrt{\mu_0\varepsilon_0}$ and the unit vector in direction of propagation $\hat{e}_k$. By squaring both sides of Equation 2.94 and solving for α and β using the quadratic formula gives (Balanis, 1989):

$$\alpha = \frac{2\pi f}{c_0}\sqrt{\frac{\varepsilon'}{2}\left(\sqrt{1+\left(\frac{\varepsilon''}{\varepsilon'}\right)^2} - 1\right)} \tag{2.95}$$

$$\beta = \frac{2\pi f}{c_0}\sqrt{\frac{\varepsilon'}{2}\left(\sqrt{1+\left(\frac{\varepsilon''}{\varepsilon'}\right)^2} + 1\right)} \tag{2.96}$$

The wavelength λ is defined as $\lambda = 2\pi/\beta$ and the skin depth δ as $1/\alpha$, the depth at which the electric field magnitude drops to $1/e$. In Figure 2.16 the simulated electric field for a plane wave at 300 MHz is plotted. The dielectric properties were chosen to be of grey matter at 300 MHz and 37°C (see Section 2.5.3). It is obvious from the wavelength and the rounded shape of the human head, that the incident EM fields do interfere and strong signal inhomogeneities occur at high fields (Hoult and Phil, 2000; Robitaille et al., 1998). Another challenge and a major health concern at high field is the induced tissue heating caused by the RF pulses.

2.6 RF Heating and SAR

The primary bioeffect of RF radiation in MRI is tissue heating and a considerable amount of the transmitted RF power is converted into heat within the patient's tissue (Shellock, 2000). According to Faraday's law, the time-varying $\boldsymbol{B_1}$ field used

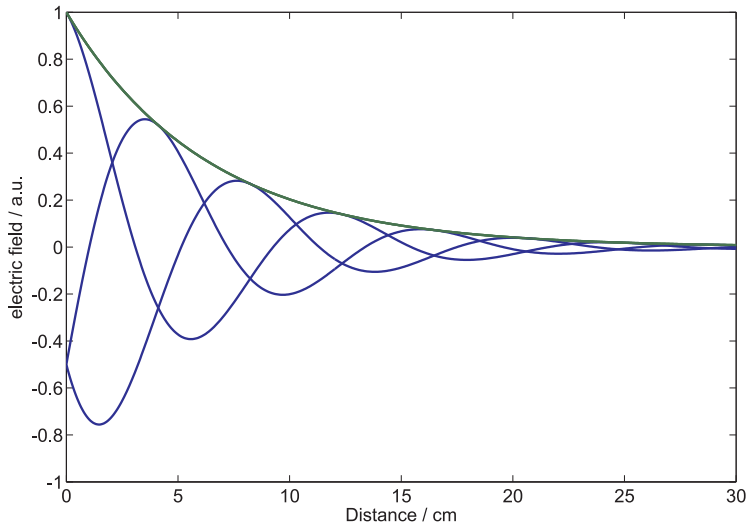

Figure 2.16: *Simulated wave propagation for 297.22 MHz in a dielectric of $\varepsilon' = 60.1$ and conductivity $\sigma = 0.69 S/m$ (grey matter). The skin depth in grey matter is 6.3 cm and the wavelength 12.4 cm. White matter has on average a lower relative permittivity $\varepsilon' = 43.8$ and conductivity $\sigma = 0.41 S/m$. Resulting in an average wavelength of 14.7 cm and skin depth of 8.8 cm at 297.22 MHz in white matter. The dielectric properties of white matter are highly anisotropic due to its highly anisotropic structure needed for electric neuronal interaction. The anisotropy of white matter is utilized in diffusion MRI (Jones et al., 2013; Turner et al., 1990).*

to manipulate the net spin magnetisation induces electric fields $\boldsymbol{E}$:

$$\nabla \times \boldsymbol{E} = -\frac{\partial \boldsymbol{B}}{\partial t} \tag{2.97}$$

these electric fields are therefore called 'magnetically induced' fields. In addition, electric fields can arise from electric potentials on nearby wires and capacitors.[86] These electric vector fields are irrotational and the gradient of a scalar electric potential, identifying them as a 'conservative' field.[87] For most applications in MRI the magnetically induced electric fields dominate, except for small coils or capacitances close to the tissue (Collins and Wang, 2011). The vector sum of both electric fields then causes a current flow in conductive tissue according to Ohm's law (Eq. 2.82: $\boldsymbol{J} = \sigma \boldsymbol{E}$), which in turn causes tissue heating.

Dissipated power P in tissue is described by (Jackson, 1998):

$$P = \int_V \boldsymbol{J} \cdot \boldsymbol{E}\, dV = \int_V \sigma \boldsymbol{E}^2\, dV \tag{2.98}$$

To better estimate the potential risk of RF induced heating, the bioelectromagnetic

[86] According to Gauss's law: $\nabla \cdot E = \rho/\varepsilon_0$ with the charge density ρ.

[87] In a conservative vector fields the line integral from one point to another is independent on the choice of the path connecting the two points.

and MRI communities use the term specific absorption rate (SAR), defined as the absorbed power per tissue mass:

$$SAR = \frac{\sigma \boldsymbol{E}^2}{\varrho} \tag{2.99}$$

where ϱ is the local tissue density. SAR is usually averaged over the whole body or over tissue samples of 1 g or 10 g (Magin et al., 1992).[88] RF power deposition and SAR has been extensively studied (Bottomley et al., 1985; Chen et al., 1986; van Lier et al., 2012; Vaughan et al., 2001). For RF frequencies below 60 MHz where the wavelengths are much larger than the imaged tissue, the induced electric fields can easily be approximated analytically.[89] The electric and magnetic field behaviour in this so called quasistatic regime is nicely described in several publications, e.g. Collins and Wang (Collins and Wang, 2011) or in the book by Haacke et al. (Haacke et al., 1999). It is shown that the total SAR increases quadratically with frequency, assuming a constant conductivity.[90] For higher frequencies practically all SAR calculations rely on simulations (Collins, 2006). However, some attempts have been made to analytically describe the EM fields in simple geometries for higher frequencies (Bottomley and Andrew, 1978; Hoult and Phil, 2000). These analytic calculations and RF simulations show that the quadratic SAR increase with frequency becomes smaller for higher frequencies (Tang and Ibrahim, 2007; Vaughan et al., 2001). Vaughan et al. found that 2.1 times more power was needed at 7 T compared to 4 T to attain a 90° pulse in the center of the brain (Vaughan et al., 2001). Here it should be mentioned that the magnetic field in the center was the same, but on average the field at 4 T should be higher and more homogeneous across the brain. This is due to the field focusing effect seen at high field (Hoult and Phil, 2000).[91]

The standard approximation for low magnetic fields states, that the induced electric fields $\boldsymbol{E}$ increase linearly with frequency, according to Faraday's law (Equation 2.97).[92] This results in a quadratic increase in SAR (see Equation 2.99). Additionally, dielectric dispersion (see Section 2.5.3) causes an increase in conductivity with frequency and therefore even higher average SAR. The decrease in wavelength

[88] To estimate the upper limit of the RF induced temperature change the specific heat capacities of tissue are needed. The specific heat of human tissue is on average 3500 J/(kg K), which is smaller than the specific heat of water (4178 J/(kg K) at 37°C) ("2.3.6 Specific heat capacities" 2005; McCall, 2010).

[89] The wavelengths in grey matter are approximately, 40 cm at 1.5 T, 24 cm at 3 T, 12 cm at 7 T (also see Equations 2.95 and 2.96 and Figure 2.13).

[90] The assumption of a constant conductivity is not correct. As described in Section 2.5.3 and especially Figure 2.14 the conductivity increases with frequency.

[91] A homogeneous field is only a static solution, and the more the wavelength shrinks and approaches the dimensions of the human body as B_0 field strength rises, the more inhomogeneous the RF field must be.

[92] The linear increase of the induce E-fields with increasing frequency only holds for a constant B_1^+ field distribution. However, the assumption of a constant B_1^+ field distribution becomes less and less valid as the RF frequency increases, leading to a less than linear increase of induced E-fields with frequency (Collins and Smith, 2001).

causes the SAR distribution in the object to be more inhomogeneous, which causes a decrease in local SAR in some locations and again an increase in others. Normally one tries to apply the $\boldsymbol{B}_1^+$ field in a circular mode for better efficiency (Haacke et al., 1999). Due to stronger absorption and the spatially varying phase of $\boldsymbol{B}_1^+$ the circular mode gets less efficient and again requires more SAR (Homann, 2011). This discussion shows that SAR presents a serious problem at 7 T and higher, since many sequences are already at the SAR limit at 3 T.

SAR Regulatory Limits

SAR (see Eq. 2.99) limits in the European Union are specified by the European Committee for Electrotechnical Standardization (CENELEC). CENELEC follows the standards of the International Electrotechnical Commission (IEC), which specifies the requirements for the safety of patients in MRI in standard IEC 60601-2-33 (International Electrotechnical Commission, 2008). In normal operation mode the IEC standard specifies the average SAR for the whole body, an exposed body part and specifically the head for an averaging time period of 6 minutes (see table 2.2). The

Whole body SAR	Partial body SAR	Head SAR
whole body	exposed body part	head
2	2 - 10 (a)	3.2

Table 2.2: *Normal mode IEC 60601-2-33 standard for the average SAR in W/kg in 6 minutes. (a) The limit varies depending on the exposed patient mass.*

local SAR limit for a tissues mass of 10 g is also specified and given in table 2.3. Additionally, the SAR limit over any 10 s period shall not exceed three times the

Local SAR		
head	trunk	extremities
10 (b)	10	20

Table 2.3: *Normal mode IEC 60601-2-33 standard for the local SAR of any tissue mass of 10 g in W/kg, also averaged over a period of 6 minutes. (b) Further limited by a maximum tissue temperature increase of 1 K.*

specified 6 minutes SAR limit.

2.7 Bloch Simulation

This section is based on the publications by Allard and Helgstrand, 1997 and Helgstrand et al., 2000 for simulating nuclear magnetic resonance experiments with

chemical exchange. The inhomogeneous Bloch equations in the rotating frame can be can be written in matrix form as (see Section 2.1.4 Equation 2.31):

$$\frac{d}{dt}\begin{pmatrix} M_x \\ M_y \\ M_z \end{pmatrix} = -\begin{pmatrix} 1/T_2 & \Delta\Omega & -\omega_y \\ -\Delta\Omega & 1/T_2 & \omega_x \\ \omega_y & -\omega_x & 1/T_1 \end{pmatrix}\begin{pmatrix} M_x \\ M_y \\ M_z \end{pmatrix} + \begin{pmatrix} 0 \\ 0 \\ M_0/T_1 \end{pmatrix} \tag{2.100}$$

with $\Delta\Omega = \omega_0 - \omega_{RF}$ the resonance offset frequency and ω_0 the Larmor frequency. $\omega_x = -\gamma B_1 \cos\phi$ and $\omega_y = -\gamma B_1 \sin\phi$ with B_1, ω_{RF} and ϕ the strength, frequency and phase of the applied RF-pulse, respectively. ω_x and ω_y are the precession frequencies of the magnetisation about the transversal x- and y-axis.

The inhomogeneous Bloch Equation 2.100 can be rewritten in a homogeneous form by appending a constant to the magnetisation vector and including the longitudinal equilibrium magnetisation in the matrix:

$$\frac{d}{dt}\begin{pmatrix} 1/2 \\ M_x \\ M_y \\ M_z \end{pmatrix} = -\begin{pmatrix} 0 & 0 & 0 & 0 \\ 0 & 1/T_2 & \Delta\Omega & -\omega_y \\ 0 & -\Delta\Omega & 1/T_2 & \omega_x \\ -2M_0/T_1 & \omega_y & -\omega_x & 1/T_1 \end{pmatrix}\begin{pmatrix} 1/2 \\ M_x \\ M_y \\ M_z \end{pmatrix} \tag{2.101}$$

Equation 2.101 can be solved like any homogeneous first-order differential equation:

$$\frac{d}{dt}\sigma(t) = -P\sigma(t) \tag{2.102}$$

$$\Rightarrow \sigma(t + \Delta t) = e^{-P\Delta t}\sigma(t) \tag{2.103}$$

where

$$P = \begin{pmatrix} 0 & 0 & 0 & 0 \\ 0 & 1/T_2 & \Delta\Omega & -\omega_y \\ 0 & -\Delta\Omega & 1/T_2 & \omega_x \\ -2M_0/T_1 & \omega_y & -\omega_x & 1/T_1 \end{pmatrix} \quad \text{and} \quad \sigma = \begin{pmatrix} 1/2 \\ M_x \\ M_y \\ M_z \end{pmatrix}. \tag{2.104}$$

For speeding up the calculations, an improved algorithm recently introduced by Müller et al., 2013 was used (Müller et al., 2015). The simulation algorithm was implemented in Matlab (MathWorks, USA). From the MR IDEA sequence development environment exported slice-select gradient amplitudes, RF-pulse shapes and phases can then be used to calculate the magnetisation vector step by step and with a temporal resolution of $\Delta t = 5\ \mu s$. This was normally done for a 10 mm slab and a variable resolution of up to 4096 isochromates along the slice select gradient. A simulated time series for an on-resonant gradient reversal SE slice excitation is displayed in Figure 2.17. The nominal slice thickness is 1.5 mm, in the simulation it is approximately 2 mm and over a thickness of more than 2.3 mm the magnetisation is strongly influenced by the excited slice and partially saturated, inverted and

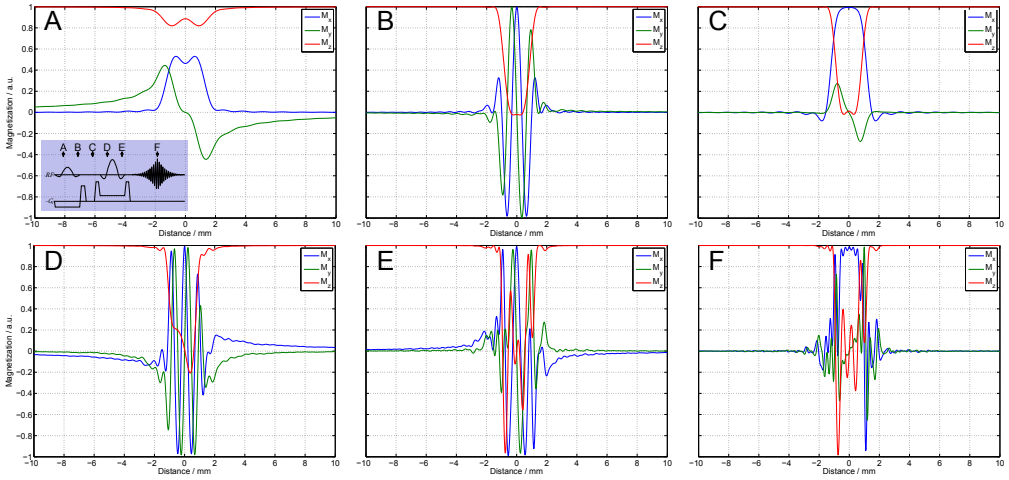

Figure 2.17: *Simulated on-resonant GR SE slice excitation time series for the sequence parameters used in Section 5.2.3 on in-vivo MR thermometry (specified slice thickness 1.5 mm). The points in time depicted in the subfigures are displayed in the blue box in Figure A. Displayed is the x-, y-, z-magnetisation along the direction of the slice select gradient in blue, green and red, respectively (as always z is along the B_0 direction and x and y in the transverse plane). The simulation starts in equilibrium, when all the magnetisation is in the z-direction. (B) The excitation RF pulse is almost finished and therefore the value of the z-magnetisation is close to zero at the position of the slice and the magnetisation in the transverse plane dephased. (C) The dephased transverse magnetisation is rephased by the gradient following the RF pulse and almost completely along the x-direction. (D) The crusher gradient before the refocusing pulse dephased the transverse magnetisation and the RF pulse just started to manipulate the magnetisation. (E) Almost at the end of the refocusing pulse, the z-magnetisation is much more irregular than before and the transverse magnetisation dephased. (F) At the time of the SE, the transverse magnetisation is rephased in x-direction, however the slice profile is more irregular than before and the magnetisation at one point even inverted.*

dephased in the transverse plane. The vector sum of the transverse magnetisation along the complete slab gives a relative MR phase and a magnitude proportional to the MR signal amplitude. The Bloch simulation for the slab was then done for varying frequency offsets and flip angle magnitudes to generate simulated MR magnitude and phase profiles which are plotted in Figures 5.16 and 5.17.

Chapter 3

Measuring the transmit RF field - B_1^+ Mapping

In this chapter an overview and evaluation of a selection of five B_1^+ mapping sequences is given. This was done to make an educated decision on which B_1^+ mapping method to use for this work and to know its limitations. A broader overview of B_1^+ mapping methods was done by Pohmann and Scheffler (2013).

The goal of B_1^+ mapping is to measure the active magnetic component of the RF field, i.e. the transverse component of the RF magnetic field that rotates in the same direction as the magnetisation and therefore is able to effectively manipulate the magnetisation (see Section 2.1.3). B_1^+ mapping is used to evaluate RF coil performance, adjust the transmit voltage and to correct quantitative imaging (Insko and Bolinger, 1993; Volz et al., 2010). In recent years there has been a lot of interest in B_1^+ mapping due to the introduction of parallel transmit RF coils (Katscher and Börnert, 2006). In parallel transmission B_1^+ mapping techniques are needed for the excitation pulse design. The acquisition speed is critical, since a B_1^+ map for each transmit coil and patient configuration needs to be acquired (Brunner and Pruessmann, 2009).

In the work presented in this thesis mostly the Actual Flip-Angle Imaging (AFI) sequence was used to measure B_1^+ (see Section 3.2). The sequence code was received from Alexis Amadon but the implementation of the necessary evaluation software was done as part of this thesis work. Moreover, the dynamic range of AFI, which is normally from 0° to 90°-100°, was extended to 180° by using the phase of the MR images (see Section 3.2 which covers the range extension in detail). Extending the dynamic range is useful at high field since the RF field gets increasingly more inhomogeneous (cf. Section 2.5.5). Further, the range extension helps to avoid folding in of flip angle above the dynamic range into the dynamic range of the sequence. This folding in artefact is often difficult to detect with just one B_1^+ map.

A very simple and extensively employed B_1^+ mapping method that also suffers from folding in of high flip angle is the double angle method (Cunningham et al., 2006; Insko and Bolinger, 1993; Stollberger and Wach, 1996).

3.1 Double Angle B_1^+ Mapping

The double angle method involves the acquisition of two gradient echo images (see Section 2.2.3). Image I_1 with flip angle (FA) α and image I_2 with flip angle $2 \cdot \alpha$ and keeping all other sequence parameters the same. To avoid the averaging error due to improper slice profiles this technique is inherently a 3D technique and requires at least a slab selective approach (see also Section 2.7 for Bloch simulations of the slice profiles).[1] For a $TR \gg T_1$ the image signal ratio is then proportional to:

$$\begin{aligned} \frac{I_2(r)}{I_1(r)} &= \frac{\sin(2 \cdot \alpha(r))\, f\left(T_2^*, TE, B_1^-, \rho_{pd}, \dots\right)}{\sin(\alpha(r))\, f\left(T_2^*, TE, B_1^-, \rho_{pd}, \dots\right)} \\ &= \frac{\sin(2 \cdot \alpha)}{\sin(\alpha)} = \frac{2\sin(\alpha)\cos(\alpha)}{\sin(\alpha)} = 2\cos(\alpha(r)) \end{aligned} \tag{3.1}$$

where r represents spatial position and f a in general spatially varying function that alters the signal amplitude depending on T_2^*, TE, receive sensitivity B_1^- and proton density ρ_{pd}. The signal amplitudes of $I_1(\alpha)$ and $I_2(2 \cdot \alpha)$ are displayed in Figure 3.1. The actual flip angle can then be calculated as follows:

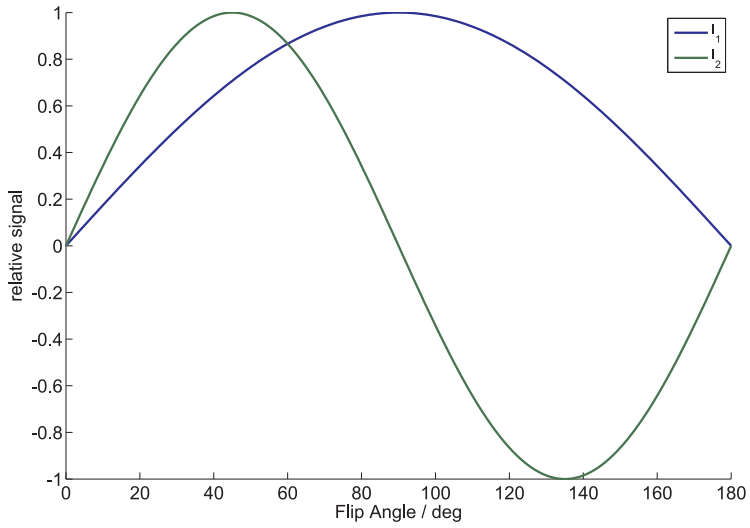

Figure 3.1: *The relative transverse signal amplitudes of the double angle method. Negative values mean that the transverse magnetisation of I_2 is shifted by 180° relative to the phase of I_1. T_1 and T_2^* effects were not considered for this plot.*

$$\alpha(r) = \arccos\left(\frac{I_2(r)}{2I_1(r)}\right) \tag{3.2}$$

For the conventional double angle method only the signal magnitude is considered for evaluation and therefore the dynamic range is between 0° and 90°. Higher actual

[1] For the slab selective approach, the outer slices need to be neglected. The high flip angle for image I_2 makes improper slice or slab profiles unavoidable.

flip angle are folded in, such that for a flip angle $\alpha = 100°$ the double angle method would determine an erroneous 80° flip angle. The dynamic range of the double angle method can be extended to $\alpha = 180°$ by considering the phase of the gradient echo images.[2] If a magnetisation along B_0 experiences a flip angle larger than 180°, the phase of the transverse magnetisation is phase shifted by 180° with respect to the phase of the transverse magnetisation for flip angle below 180°. This is for example illustrated by $\alpha = 135°$ and $2 \cdot \alpha = 270°$. In this case, the relative phase between the two transverse magnetisations is 180°.[3] In this way the otherwise ambiguous magnitude signal of I_2 can be uniquely mapped to a flip angle α up to 180°. The phase shifted signal I_2 is given a negative sign, which therefore follows a sinusoidal behaviour (see Figure 3.1).

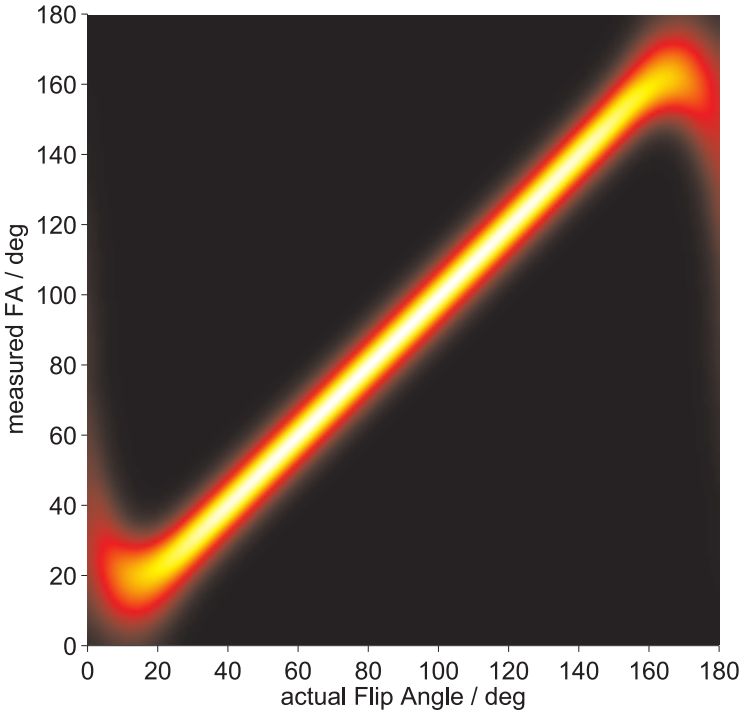

Figure 3.2: *2D histogram plot of the Monte Carlo simulation for the double angle method. Ideally, the actual and measured Flip Angle (FA) should coincide and therefore give a thin straight diagonal line. The measured FA clearly deviates from the actual FA for $\alpha < 20°$ and $\alpha > 160°$. The Monte Carlo simulation was done with a SNR = 100 for an unsaturated 90° FA image, $T_1 = 2000$ ms, $TR = 10$ s, $T_2^* = 30$ ms, and $TE = 4$ ms. For an actual flip angle of 90° the mean measured FA is 90.01° with a standard deviation of 0.34°.*

The noise in a real measurement causes the calculated flip angle to deviate from the actual flip angle. To evaluate the noise sensitivity of the method a Monte Carlo simulation was implemented (Metropolis and Rosenbluth, 1953). The Monte Carlo

[2] This also applies to other methods like AFI (Section 3.2), but is not mentioned in the literature.
[3] The phase shift is independent of any phase shifts introduced by B_0 or $B_1^{\pm}$.

simulation included T_1 and T_2^* decay, and assumed perfect spoiling.[4] The result for a reasonable set of imaging values is plotted in Figure 3.2. It can be nicely seen, that the measured flip angle deviates in the low and high actual flip angle regime, but has a very good performance in between and the measured FA practically matches the actual FA.

3.2 Actual Flip-Angle Imaging

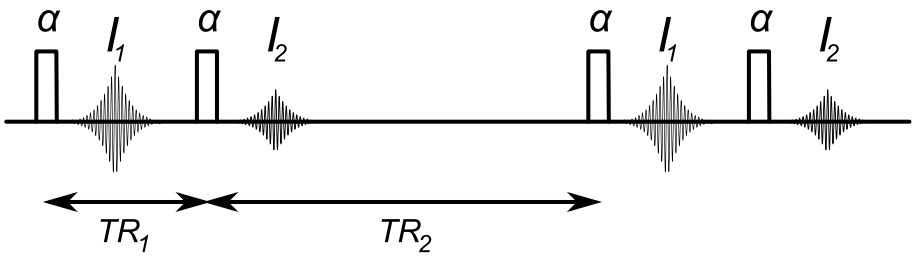

Figure 3.3: *Sequence timing diagram of the AFI pulse sequence with the exact same RF pulses for excitation followed by an identical readout, but different delays TR_1 and TR_2. The method relies on good RF and gradient spoiling, which is not included in the diagram (Nehrke, 2009).*

The relatively new actual flip angle imaging (AFI) technique of Yarnykh was introduced in 2007 and also employs the acquisition of two 3D gradient echo images (Sections 3.1 and 2.2.3) (Malik et al., 2011; Yarnykh, 2007). However, instead of waiting for the magnetisation to completely relax this approach relays on the magnetisation being in a pulsed steady state. The method consists of two identical RF pulses followed by two delays of different duration ($TR_1 < TR_2$) and a GRE acquisition immediately after each of the two pulses (see Figure 3.3). Following Yarnykh (2007), for TR_1 and TR_2 the longitudinal magnetisations $M_{z1,2}$ in the steady state before each excitation is:[5]

$$\begin{aligned} M_{z1} &= M_0 \frac{1 - A_2 + (1 - A_1) A_2 \cos\alpha}{1 - A_1 A_2 \cos^2\alpha} \\ M_{z2} &= M_0 \frac{1 - A_1 + (1 - A_2) A_1 \cos\alpha}{1 - A_1 A_2 \cos^2\alpha} \end{aligned} \tag{3.3}$$

with $A_{1,2} = e^{-\frac{TR_{1,2}}{T_1}}$. The signal intensities $I_{1,2}$ are then proportional to

$$I_{1,2} = M_{z1,2} e^{-\frac{TE}{T_2^*}} \sin\alpha \tag{3.4}$$

[4] In this context, perfect spoiling means that the transverse magnetisation is completely dephased and that no other coherence pathways contributing to the signal than the desired one (Crawley et al., 1988; Hennig, 1991).

[5] The longitudinal magnetisations $M_{z1,2}$ are easily derived for the steady state when $M_{z1,2}$ return to their initial value after each TR and excitation and relaxation processes equal out.

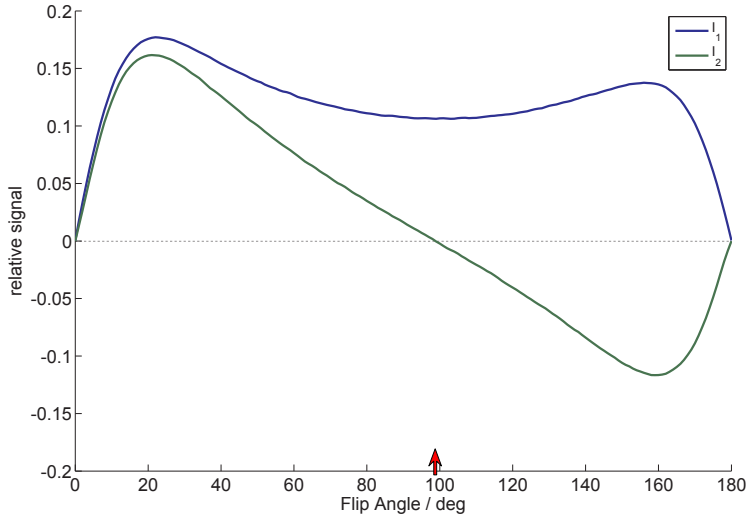

Figure 3.4: *The relative transverse signal amplitudes of the actual flip angle method. The signal amplitudes are significantly lower than for the double angle method, due to the much shorter TR and interleaved acquisition. This results in a acquisition time of just 1/67 of the double angle method (values vary on experimental conditions). Similar as in Figure 3.1 for the double angle method, negative values mean that the transverse magnetisation I_2 has a 180° phase shift relative to the phase of image I_1. The red arrow points to the FA where I_2 becomes negative (FA > 90°). The signal amplitudes were calculated for a $TE = 4$ ms, $T_2^* = 30$ ms, $T_1 = 2000$ ms, $TR_1 = 37.5$ ms, and $TR_2 = 262.5$ ms, resulting in $n = 7$.*

(see Figure 3.4) and the resulting signal ratio is then:

$$r = \frac{I_2}{I_1} = \frac{1 - A_1 + (1 - A_2)\, A_1 \cos\alpha}{1 - A_2 + (1 - A_1)\, A_2 \cos\alpha} \approx \frac{1 + n\cos\alpha}{n + \cos\alpha} \tag{3.5}$$

with

$$n = \frac{TR_2}{TR_1} \quad \text{and} \quad A_{1,2} = e^{-\frac{TR_{1,2}}{T_1}} \approx 1 - \frac{TR_{1,2}}{T_1} \quad \text{and} \quad 1 - \frac{TR_{1,2}}{T_1} \approx 1 \tag{3.6}$$

and assuming $TR_1 < TR_2 < T_1$ for the approximate solution. For the conventional, only magnitude based AFI method the highest measurable FA is achieved when the nominator of Equation 3.5 becomes negative, i.e. when $\alpha > \arccos\left(-\frac{TR_1}{TR_2}\right)$ (further discussed in Section 3.2). To calculate the achieved FA from the measured signal ratio, equations 3.5 need to be solved for α:

$$\alpha = \arccos\frac{A_1 - 1 + (1 - A_2)\, r}{(1 - A_2)\, A_1 + (A_1 - 1)\, r A_2} \approx \arccos\frac{rn - 1}{n - r}. \tag{3.7}$$

The approximate solution of Equation 3.7 can be solved without exact knowledge of T_1.[6] A T_1 on the order of TR leads to a systematic underestimation of the FA for

[6] It just has to be known that $TR_1 < TR_2 < T_1$.

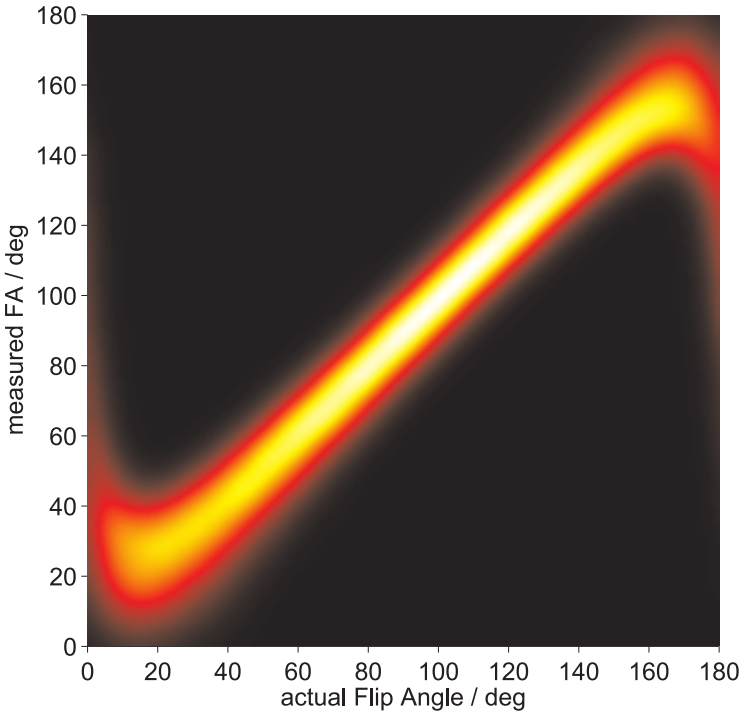

Figure 3.5: *2D histogram plot of the Monte Carlo simulation for the AFI method. Overall the standard deviation is larger than for the double angle method with similar problems for low and high actual flip angle, again for an unsaturated 90° image SNR of 100. For an actual flip angle of 90° the mean measured FA is 89.37° with a standard deviation of 5.65°. Assuming the same acquisition time as for the double angle method (3.1) and averaging the signals I_1 and I_2 would result in a similar measured FA and a standard deviation of 0.68°.*

high FA. If T_1 of the imaged tissue is known the exact solution can be used, which is relatively insensitive to uncertainties in T_1. This was often done for phantoms with a high sugar content and therefore short T_1 (≈ 440 ms).

The Monte Carlo simulation of the original and approximate AFI solution is shown in Figure 3.5. The significantly shorter acquisition time resutls in a higher noise in compare to the double angle method (Section 3.1). Averaging the raw images before doing the FA calculation leads to similar values of accuracy as for the double angle method for the same acquisition time.[7] Nehrke and Yarnykh point out that spoiling is essential for an accurate FA calculation (Nehrke, 2009; Yarnykh, 2010). This sequence including the correct gradient and RF spoiling scheme was implemented by Alexis Amadon and provided to us (Amadon and Boulant, 2008).

[7]It is important to do the averaging on the two acquired complex images, since otherwise the biases for low and high flip angle do not get reduced.

AFI Dynamic Range Extension

The dynamic range of the conventional AFI method is limited to a flip angle range between 0° and a flip angle somewhat higher than 90°. The exact upper limit of the dynamic range depends on TR_1, TR_2 and T_1. For a FA above 90° M_z (the component of the magnetisation parallel to B_0) becomes negative and partially recovers during TR_1. M_{z2} (Eq. 3.3) will be negative if TR_1 is not long enough for M_z to relax to positive values. The FA when this occurs marks the upper limit of the conventional AFI evaluation dynamic range. In the simulated case (see Figure 3.4) this occurs for a FA above 98°.[8] For FA above the limit of the conventional AFI evaluation M_{z2} will always be negative and M_{z1} will always be positive, therefore the phase of I_2 will be shifted by 180° with respect to I_1. Therefore the dynamic range of the AFI method can be extended to 180° by assigning a negative value to I_2 when the phase shift is detected. This was implemented into the AFI evaluation software written in C++ when the phase difference of I_1 and I_2 was larger than 90°.

In reality, the dynamic range is a bit smaller since for low (close to 0°) and high (close to 180°) flip angle the signal amplitudes of I_1 and I_2 are so similar that noise leads to a strong bias in measured FA (see Figures 3.4 and 3.5). The increase in dynamic range is without a large loss in signal amplitude and sensitivity in the high flip angle range. This is because the magnetisation M_{z1} does not have to relax from the inverted state for FA larger than 90° to positive M_z values during TR_1, but is actively moved to a positive M_z by the excitation pulse of image I_2. This effect also reduces a potential bias due to T_1 relaxation effects that become more important when the magnetisation is inverted. Increasing the repetition time ratio n would further reduce this bias.

Using complex images for the flip angle calculation also has the positive effect that there is no bias to lower measured FA in the region where I_2 goes to zero, i.e. when the α is approximately 90°. In pure magnitude FA calculations the magnitude has on average an offset from zero due to the Rician distribution of magnitude data (Andersen, 1996; Gudbjartsson and Patz, 1995).[9] Using complex images this can be avoided and on average a value of zero can be experimentally achieved. There is still a bias to lower measured FA for angles close to 180°, since here both I_1 and I_2 are small.

3.3 Pre-Saturation Method

Unlike the previous B_1^+ mapping methods, the pre-saturation method is most often used to map B_1^+ in 2D and therefore very suitable for parallel transmit pulse adjustment (Brunner and Pruessmann, 2009; Cao et al., 2016; Chung et al., 2010;

[8] FA higher than 98° would be folded in, i.e. a FA of 110° would yield an erroneous 86° FA (for the values used for the Monte Carlos simulation of Figure 3.4 and 3.5).

[9] This principle applies to all the originally magnitude based B_1 methods discussed here in sections 3.1 and 3.3.

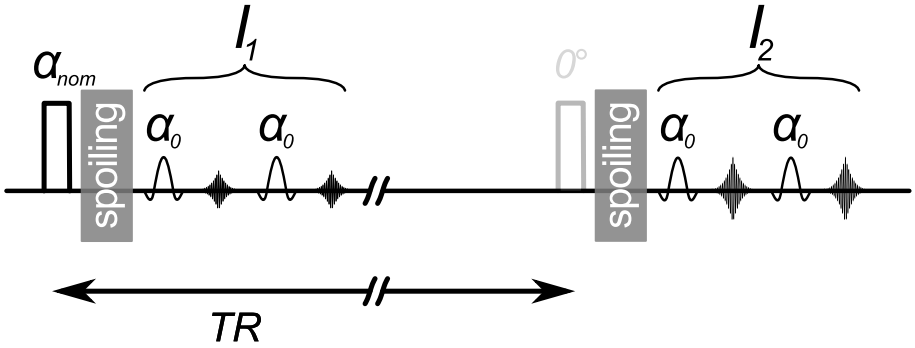

Figure 3.6: *Sequence timing diagram of the pre-saturation pulse B_1^+ mapping sequence. Two images need to be acquired. In this diagram, the first image is acquired with a pre-saturation pulse of nominal flip angle α_{nom}, then spoiler gradients are applied in all three directions followed by the image acquisition with FA α_0. The image acquisition is often done using a very fast FLASH readout, but an EPI readout can also be used (see Section 2.2.3 on GRE and EPI) (Haase et al., 1986; Stehling et al., 1991). After $TR \gg T_1$, the exact same image is acquired but with a nominal pre-saturation FA of α_{nom}= 0°. This method works under the assumption that T_1 relaxation in-between the pre-saturation and imaging RF pulse is negligible.*

Fautz et al., 2008; Klose, 1992).

The method requires the acquisition of two images (see Figure 3.6). First, a slice-selective pre-saturation RF pulse is applied with a FA α_{nom}, followed by spoiler gradients causing the net magnetisation to be parallel to B_0. The, in general, partially saturated longitudinal magnetisation is then excited and imaged by a second RF pulse with FA α_0. It is important that the slice-profile of the imaging RF pulse is thinner and in the constant part of the pre-saturation pulse profile (Fautz et al., 2008). The readout can then either by a centric-reordered fast FLASH readout or an EPI readout.[10] After $TR \gg T_1$ when the net magnetisation is in equilibrium, another image with exactly the same imaging parameters, but without the pre-saturation pulse is acquired. Assuming the T_1 relaxation between saturation and image acquisition to be small (Figure 3.6) the image signal ratio is given by:

$$r = \frac{I_1}{I_2} \approx \frac{\sin\alpha_0 \cos\alpha_{nom}}{\sin\alpha_0} = \cos\alpha_{nom} \tag{3.8}$$

with I_1 being the image after the pre-saturation pulse and I_2 the image acquired in the equilibrium magnetisation state (shown in Figure 3.7).

For parallel transmit applications the unsaturated image has to be acquired only once and a saturated image has to be acquired for each of the transmit coils. It is most efficient to do the saturation using only one coil, but the image acquisition

[10] A long centric reordered FLASH readout can lead to low signal in the outer parts of k-space and therefore to a lower actual resolution than the nominal resolutions suggests. B_1 profiles vary on the order of the wavelength and skin depth in the tissue therefore presenting no big problem at 7 T (see Section 2.5.5).

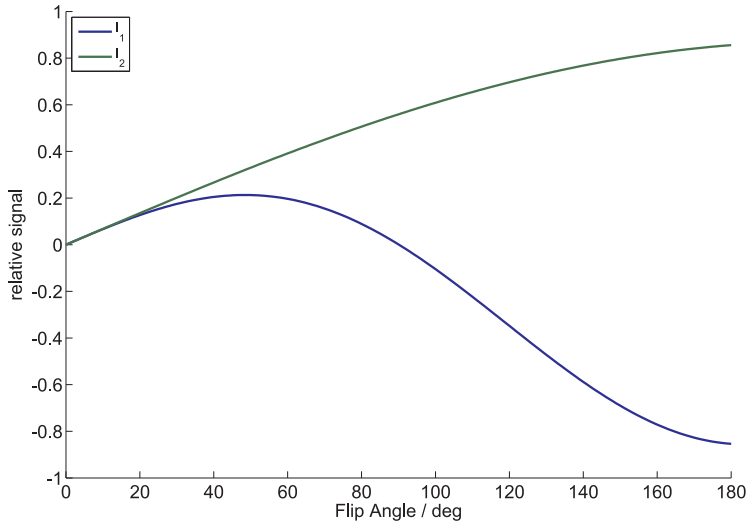

Figure 3.7: *The relative transverse signal amplitudes of the pre-saturation method. For this simulation, a single coil set-up is assumed. Therefore, the achieved pre-saturation FA and the imaging FA are coupled. In a multi transmit channel set-up the signal I_2 would be constant across the whole range and probably not equal to zero, since all transmit channels are used for imaging. Again, negative signal amplitudes I_1 are caused by a phase shift of 180° with respect to I_2. The signal amplitudes were calculated for a $TE = 4$ ms, $T_2^* = 30$ ms, $T_1 = 2000$ ms, $TR = 10$ s, and spoiling delay between saturation and imaging pulse of 4 ms.*

in the combined mode, so relatively high SNR images can be acquired across the whole field of view. This approach also gives much better accuracy for low FA (cf. Figure 3.8). Even better B_1 for low FA can be obtained using the new approach by Fautz (Fautz et al., 2012). They combine the pre-saturated B_1 maps with relative B_1 maps for low FA sensitivity. The relative B_1 maps are acquired using a FLASH acquisition. The FLASH acquisition is needed anyways to determine the relative B_1^+ phase of each channel. This sequence was part of the parallel transmit system installed on the 7 T MRI scanner.

Another approach based on the interference between the different coil elements was introduced by Brunner and Pruessmann, 2009. In principle the approach is similar to the normal pre-saturation method. However, instead of just saturating with one element at a time, all elements are used for saturation, but with a changing relative phase with respect to each other. By solving the inverse linear problem the B_1^+ fields of the individual transmit channels are determined. These individual channel B_1^+ fields have less bias and an accuracy that is largely independent of the local RF field strength of the particular coil, which is not the case for the original pre-saturation method.

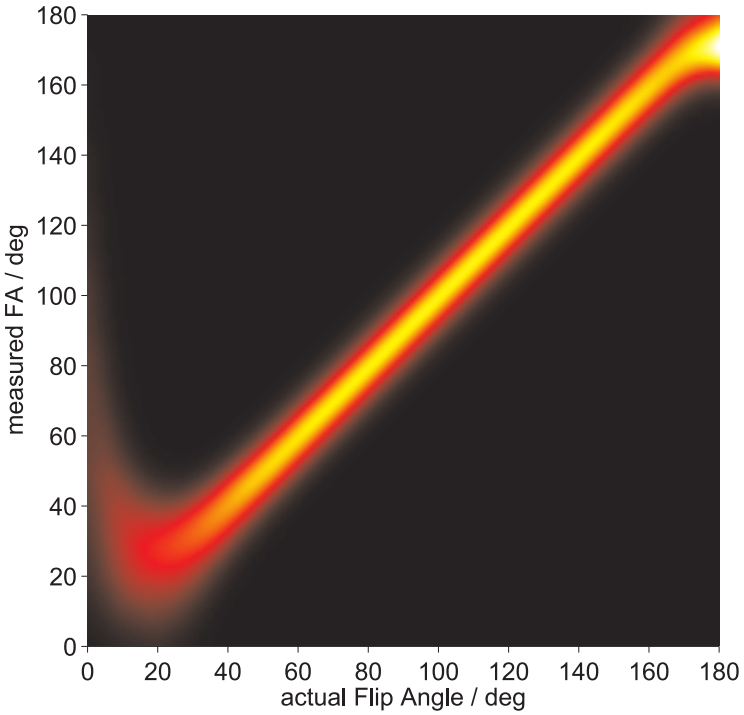

Figure 3.8: *2D histogram plot of the Monte Carlo simulation for the pre-saturation B_1 method. Overall the standard deviation is small. However in the small FA regime the deviation and bias is large. This is due to the single coil set-up, where low saturation FA also mean low imaging FA. In the parallel transmit coil approach this bias and uncertainty in the low FA regime is strongly reduced. For an actual flip angle of 90° the mean measured FA is 89.88° with a standard deviation of 1.05° (using the values given in Figure 3.7).*

3.4 Phase-Sensitive Method of FA Mapping

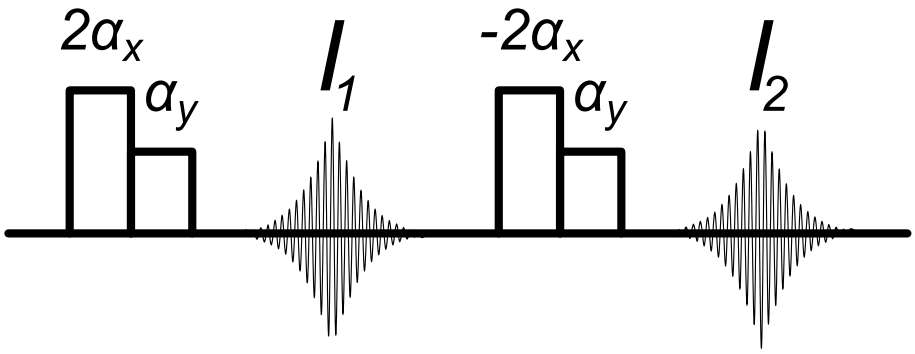

Figure 3.9: *Sequence timing diagram of the phase-sensitive B_1^+ mapping sequence introduced by Morrell (Morrell, 2008). The method is based on the application of a composite RF pulse. The first part of the pulse with FA $2 \cdot \alpha_x$ tips the magnetisation around the x-axis, the second part of the pulse α_y tips the magnetisation only half as much about the y-axis. To remove flip angle independent contributions to the phase, two images need to be acquired that differ in the phase of the $2 \cdot \alpha$ part of the composite pulse.*

Up to now, the magnitude of the MR signal was used to calculate the achieved FA and the phase was used to extend the dynamic range. There is a whole range of methods that encode the FA in the phase of the MR signal. One of the simplest methods is probably the phase-sensitive method by Morrell (Morrell, 2008). This method is based on the acquisition of two images (see Figure 3.9). For excitation a short composite pulse is used consisting of a $\pm 2 \cdot \alpha_x$ sub-pulse around the x-axis and a α_y sub-pulse around the y-axis. The data can be acquired using different acquisition schemes, e.g. GRE or EPI. Given an initial magnetisation along B_0, the composite RF pulse $2\alpha_x\ \alpha_y$ generates the following magnetisation:

$$\begin{aligned} M_x &= -M_{z_0} \sin\alpha \cos 2\alpha \\ M_y &= M_{z_0} \sin 2\alpha \\ M_z &= M_{z_0} \cos\alpha \cos 2\alpha \end{aligned} \tag{3.9}$$

with M_{z_0}, the magnetisation along B_0 before the pulse. The phase of the transverse component M_{xy} is therefore strongly dependent on the flip angle α. This is demon-

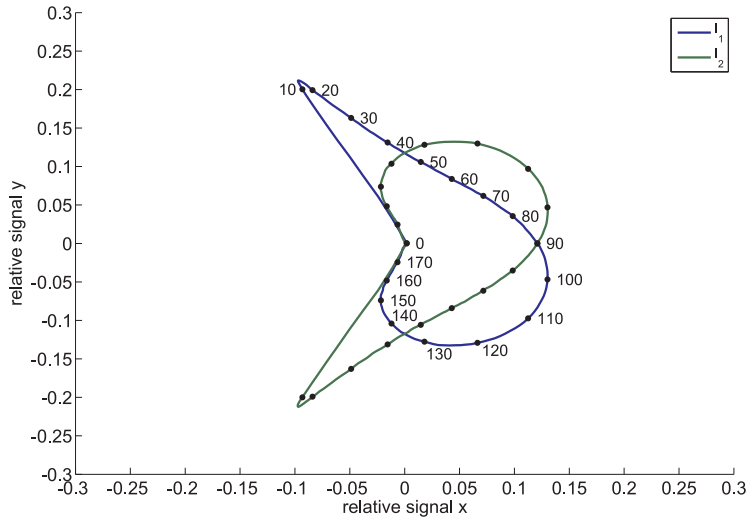

Figure 3.10: *Plotted is the relative signal in the transverse plane given for the two composite pulses of Figure 3.9 in steady-state. Next to the data points of I_1 are the angles α in degree. The two composite pulses $\pm 2\alpha_x\ \alpha_y$ generate x-axis symmetric transverse magnetisations. The phase difference of the two acquisitions is plotted in Figure 3.11. It is already obvious from this plot, that the sensitivity for low and high FA is low, similar to all the other methods.*

strated in Figure 3.10 where the transverse component of the magnetisation for different FA is plotted. The plot is based on realistic scan values of $T_1 = 2000$ ms, $TR = 300$ ms, $T_2^* = 30$ ms, $TE = 4$ ms, and the duration of the composite pulses of 2 ms. Assuming to be on-resonant and in steady-state.[11,12]

[11] Off-resonance introduces an error in the FA calculation which can be corrected if an additional B_0 map is acquired.

[12] The steady-state is the reason why this plot (Figure 3.10) looks different to the plot given in

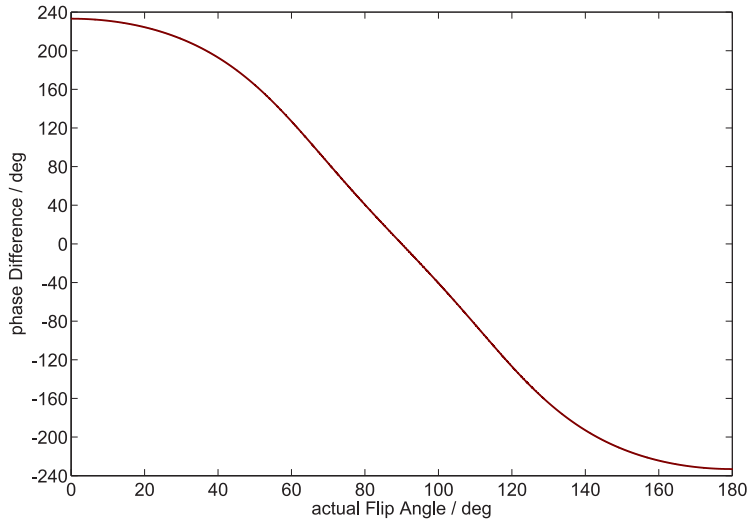

Figure 3.11: *Plotted is the phase difference of the two acquisitions I_1 and I_2 plotted in Figure 3.10. The sensitivity of the method is greatest in the center of the plot, where the slope of phase change vs. FA is the greatest.*

To images with $\pm 2\alpha_x$ α_y need to be acquired to remove phase variations not related to the excitation, similar to the case of MR thermometry (see Section 2.3.4). Since there is no easy analytical solution to the behaviour of the phase difference (cf. Equation 3.9 and Figure 3.11) it is recommended to make a lookup table relating the achieved FA to the measured phase difference (Morrell, 2008). Additionally, as the phase difference spans from 233° for a FA of 0° to -233° for a FA of 180°, there will most likely be phase wraps in the phase difference image that need to be unwrapped.[13]

The Monte Carlo simulation for the phase-sensitive method using a lookup table is plotted in Figure 3.12. The plot was made assuming a SNR of 100 (for an unsaturated 90° pulse) and 1000 trails per FA were made. The phase-sensitive method of Morrell performs better at low FA compared to all the other methods, but worse for the very high FA. This is caused by the small slope of phase difference vs. FA (cf. Figure 3.11) and the low signal amplitude for high FA. For an actual flip angle of 90° the mean measured FA is 89.95° with a standard deviation of 1.70°, using the parameters given above and used for all of the plots. This technique can be used in 2D or 3D mode using short pulses that can still be approximated by Equation 3.9. And the acquisition speed can be further increased by using a short TR. The lower limit for TR depends on T_1 and the actually achieved flip angle. For some FA, the magnetisation M_z is in the inverted state after excitation. If the next excitation is applied before it has returned to a positive M_z, the phase of the magnetisation would alternate and not be usable.[14]

the original publication of Morrell, 2008.

[13]Phase unwrapped can be done with the ΦUN software from Jena (Witoszynskyj et al., 2009).

[14]This is similar to the AFI method at high FA, but in that case the images are acquired interleaved and therefore an alternating phase is desirable 3.2.

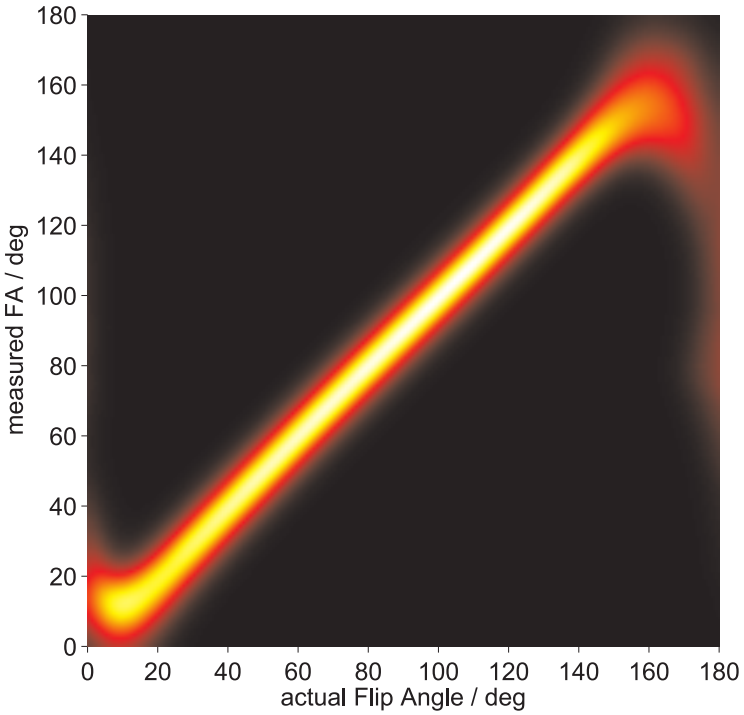

Figure 3.12: *2D histogram plot of the Monte Carlo simulation for the phase-sensitive method (Morrell, 2008). The phase-sensitive method works better at low FA then all the previous methods, but worse at high FA.*

3.5 B_1^+ Mapping by Bloch-Siegert Shift

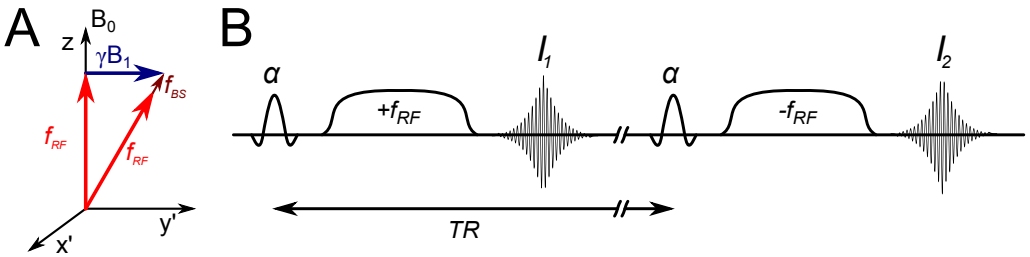

Figure 3.13: *(A) In the by f_{RF} off-resonance rotating frame of reference the spins experience an effective field, which is made up of $B_{RF} = f_{RF}/\gamma$ along B_0 and the B_1 field of the RF pulse. For $\gamma B_1 \ll f_{RF}$ this results in an effective field experienced by the spins that is slightly larger than the B_{RF} field and still approximately along B_0. This small extra field causes the so called Bloch-Siegert frequency shift f_{BS}. (B) Sequence timing diagram of the Bloch-Siegert B_1^+ mapping sequence. Two images need to be acquired using for example a gradient echo acquisition with flip angle α. The first image I_1 is acquired with a positive frequency offset f_{RF} for the Bloch-Siegert pulse and the second image I_2 with a negative frequency offset.*

Another phase sensitive B_1^+ mapping technique was published in 2010 (Sacolick

et al., 2010).[15] It is based on the so called 'Bloch-Siegert shift' describing the effect that the nucleus experiences a slightly different effective B-field when an off-resonant RF field is applied (Bloch and Siegert, 1940; Ramsey, 1955). This field does not excite the spin system, but changes the precession frequency.

Figure 3.13 (A) depicts the B-fields acting upon the spins in the rotating frame with off-resonance frequency f_{RF}. The frequency difference between the spin Larmor frequency and f_{RF} can be seen as a constant magnetic field $B_{RF} = f_{RF}/\gamma$ along the z-axis and perpendicular to it the B_1 of the off-resonant RF field.[16] For the right triangle of Figure 3.13A therefore holds:

$$(f_{RF} + f_{BS})^2 = f_{RF}^2 + (\gamma B_1)^2 \tag{3.10}$$

with the extra Bloch-Siegert frequency component f_{BS}. Solving for f_{BS} and doing a series expansion for small $\gamma B_1 \ll f_{RF}$ gives (Ramsey, 1955):

$$f_{BS} = \sqrt{f_{RF}^2 + (\gamma B_1)^2} - f_{RF} \approx \frac{(\gamma B_1)^2}{2 f_{RF}}. \tag{3.11}$$

By putting the off-resonant RF field between the excitation and readout of an imaging sequence, this frequency change f_{BS} can be measured by means of the induced MR phase change (see Figure 3.13B).[17] The magnetisation phase change ϕ_{BS} for an arbitrary $B_1(t)$ with off-resonant frequency $f_{RF}(t)$ and using the Bloch-Siegert frequency given by Equation 3.11 is then:

$$\phi_{BS} = \int_0^T f_{BS}(t)\, dt \approx \int_0^T \frac{(\gamma B_1(t))^2}{2 f_{RF}(t)} dt. \tag{3.12}$$

Acquiring one image I_1 with a positive $+f_{BS}$ and another image I_2 with a negative frequency offset $-f_{BS}$ eliminates phase altering effects of a single acquisition and to first order corrects for B_0 inhomogeneities (for $f_{B_0} \ll f_{RF}$) (Sacolick et al., 2010).[18]

The simulated transverse signal of the two images is shown in Figure 3.14. For the simulation a Fermi-pulse (Figure 3.13 B) with a duration of 8 ms and a peak B_1 of 20 μT was used. The 20 μT were used to encode a flip angle of 180°.[19] TR was set to 300 ms and the echo time to 14 ms. All the other parameters were the same as for the other simulations before (e.g. Figure 3.2). In Figure 3.15 the phase difference of the two acquisitions is plotted. For low FA the noise biases

[15] Laura Sacolick won the Young Investigator Award of the International Society of Magnetic Resonance in Medicine for the introduction of this novel concept to measure B_1^+.

[16] For protons $\gamma = 42.576$ MHz/T.

[17] Sacolick et al. recommend in their two papers on the Bloch-Siegert shift B_1 mapping method to either use a GRE or spin-echo sequence (see Section 2.2.3) (Sacolick et al., 2010, 2011).

[18] A symmetric 1000 Hz B_0 inhomogeneity combined with a Bloch-Siegert pulse of $f_{RF} = 4$ kHz leads to a maximum error in the measured B_1 of 2 %.

[19] An on-resonant square RF pulse applied for 1 ms with a 11.7 μT amplitude tips the magnetisation by a FA of 180° (cf. Section 2.1.3).

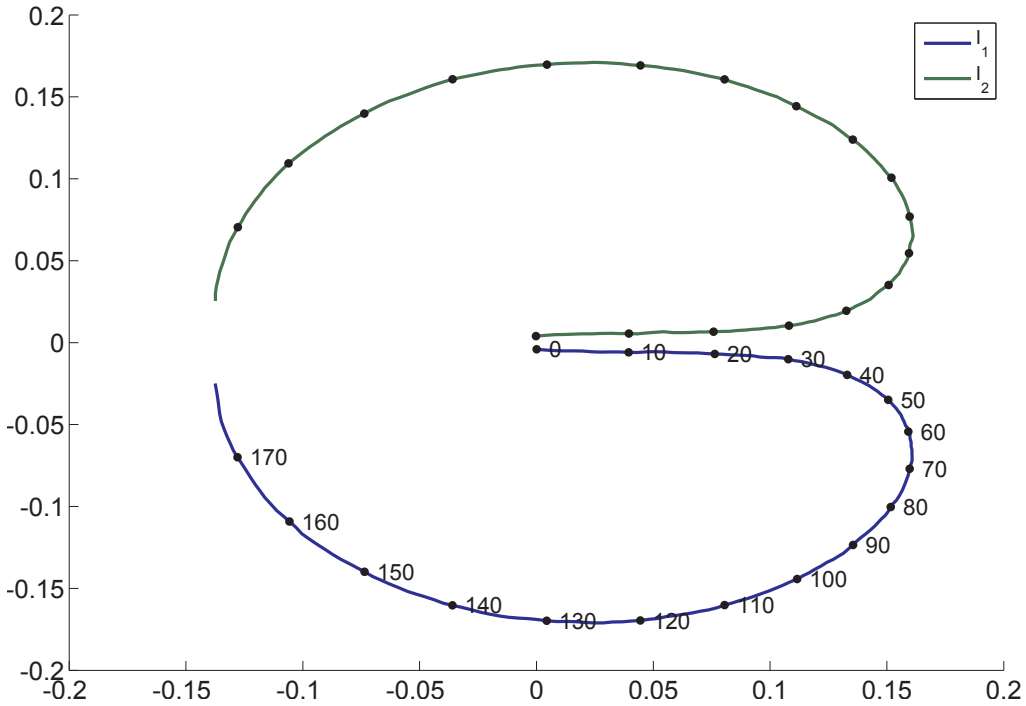

Figure 3.14: *Plotted is the relative signal in the transverse plane. The two signals were simulated in the steady-state with a 4 kHz positive and negative off-resonance, as seen in Figure 3.13 (B). Next to the data points of I_1 are the angles α in degree. In the case of the Bloch-Siegert methods these angles are just a scaling factor for the applied B_1 with the specific off-resonant frequency. The phase difference of the two acquisitions is plotted in Figure 3.15. It is already clear from this plot, that the sensitivity for low FA is low, worse than for the other methods. However, it is very sensitive for high FA.*

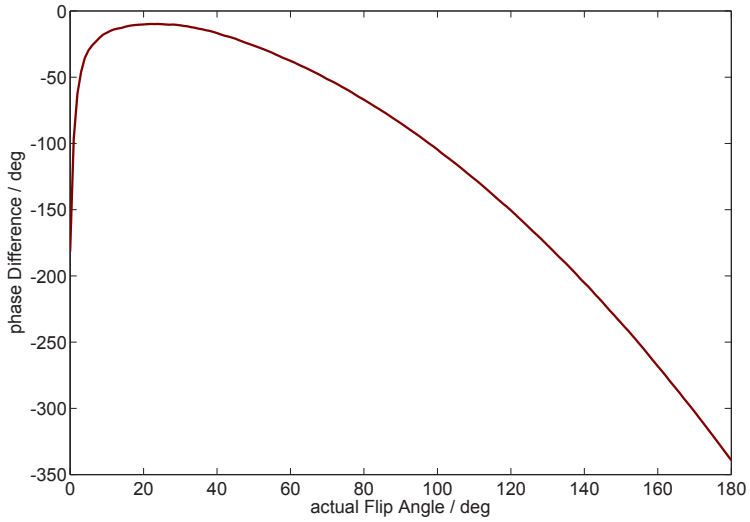

Figure 3.15: *Plotted is the phase difference of the two acquisitions I_1 and I_2 plotted in Figure 3.14. Noise causes the interpretable signals for low FA to deviate from 0 with small signal magnitude, but large phase difference.*

the results in such a way that the mean interpretable signals are not approaching zero. The phase difference between the two images therefore become large and fold into the high FA range. Figure 3.16 nicely shows this for low FA, where measured

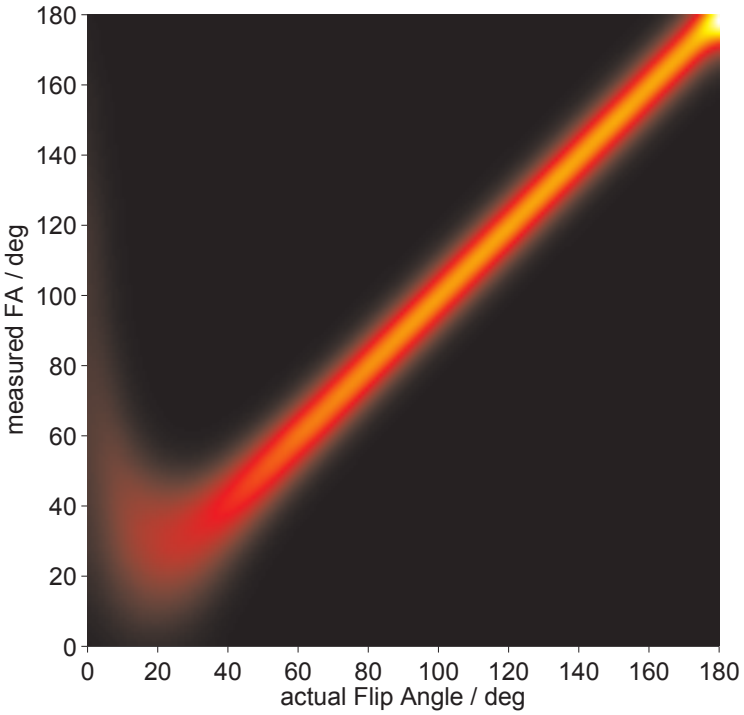

Figure 3.16: *2D histogram plot of the Monte Carlo simulation for the Bloch-Siegert method (Sacolick et al., 2010, 2011). The Bloch-Siegert method works better at high FA then all the previous methods, but worse at low FA. The relatively fast Bloch-Siegert method returns a measured mean FA of 89.91° with a standard deviation of 2.39° for an actual FA of 90°.*

and actual FA strongly deviate with large spread in measured FA. The method becomes increasingly more accurate for high B_1^+ due to the square dependence of the Bloch-Siegert phase shift (cf. Equation 3.12). Since B_1 is a smoothly varying function of distance the dynamic range of the method can be extended to higher FA using phase unwrapping (Witoszynskyj et al., 2009). However SAR will most likely be the limiting factor, since a typical Bloch-Siegert pulse would have a FA of 1200° or higer if it were on-resonant (see Section 2.6 and Figure 3.13). Khalighi et al. discuss pulse optimization that maximize the Bloch-Siegert phase shift and minimize SAR (Khalighi et al., 2013, 2011). The SAR can further be minimized by using spiral, EPI or any other phase sensitive readout. The small flip angle bias can be reduced by combining the Bloch-Siegert method with the interferometric approach by Brunner et al. (Brunner and Pruessmann, 2009).

Chapter 4

Influence of Air Susceptibility on PRF MR Thermometry

To test MR thermometry sequences it is useful to have a well defined and significant temperature increase across the whole phantom. Using hot air to heat a phantom inside the scanner is convenient, since the phantom can be put into the scanner in thermal equilibrium with the environment and the necessary phase reference images can be acquired prior to heating on a homogeneous and well known temperature distribution.[1] In addition, it is cheap and easy to set up, since only a hair dryer and some pipes are necessary. However, when doing the first experiments, an apparent and almost homogeneous MR temperature increase across the phantom was always measured at the time when the hair dryer was turned on. An artefact could be excluded since it appeared in all the measurements. Another explanation was movement of the phantom due to the air flow that was turned on when the heating started. Movement was excluded after another measurement with a fixed phantom and a continuous cold air flow before heating. After another measurement with a field reference substance outside of the heating air flow, it was clear that the reason could only be the air itself.[2]

In this chapter, which is based on the publication 'Effects of air susceptibility on proton resonance frequency MR thermometry' Streicher et al.,[3] the effect of a changing susceptibility of surrounding air on the magnetic field inside an object and the possible MR temperature error is discussed. In one experiment, the surrounding air susceptibility was varied by changing the air temperature. In another set of experiments, the surrounding air susceptibility was changed by changing its gaseous composition. To assess the dependence of the effect on the experimental configuration, the size of the gas container and the size of the enclosed agar gel phantom were varied. All experiments were simulated and compared with the experimental results.

[1] The phase reference is necessary for simple PRF phase MR thermometry (Rieke and Butts-Pauly, 2008b).

[2] The reference substance outside the airflow did not detect a field change.

[3] Complete author list: Markus N. Streicher, Andreas Schäfer, Enrico Reimer, Bibek Dhital, Robert Trampel, Dimo Ivanov, Robert Turner.

4.1 Experimental Set-ups

4.1.1 Hot Air Experiment

Air Heating Set-up

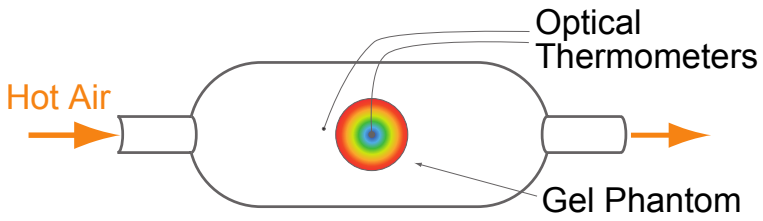

Figure 4.1: *The agar gel phantom was positioned in the middle of a cylindrical polystyrene box connected by long piping to a hair dryer outside the scanner room. The air temperature and the temperature in the centre of the phantom were measured with fibre-optic thermometers.*

To illustrate the effect of a surrounding air temperature change on the PRF shift MR temperature, a spherical 1 % agar gel phantom (0.9 % NaCl, diameter 10 cm) was mounted inside a polystyrene foam box (see Figure 4.1) connected by long pipes on both ends. At the end of one pipe, a hair dryer was placed outside the scanner room. The phantom within the polystyrene box was positioned inside a circularly polarized (CP) RF coil (single channel, In vivo, Orlando, FL, USA) at the magnet isocenter. Experiments were carried out on a 7 T whole body scanner (7 T Magnetom, Siemens Healthcare, Erlangen, Germany). The hair dryer continuously blew air through the piping into the box and around the phantom. With the hair dryer heating control, the air temperature surrounding the agar phantom could be raised from room temperature to about 70°C (Pandeya et al., 2012). Due to the heat capacity of the long piping from outside the scanner room to the phantom inside the scanner, it took more than 10 minutes after heating was commenced for the air surrounding the phantom to reach 69°C. An accurate fibre-optic temperature sensor (Luxtron LumaSense Technologies, Santa Clara, CA, USA) was placed inside the polystyrene box to monitor the air temperature around the phantom, and another fibre-optic temperature sensor was placed in the centre of the agar phantom. At the active point of the fibre-optic thermometer, a MR image voxel was used to compare the fibre-optic temperature with the MR temperature. For all the experiments described, the agar phantoms initially had a constant temperature equal to the scanner room temperature.

Imaging and Evaluation

Coronal MR magnitude and phase images were acquired continuously throughout the experiments with a standard 2D spoiled gradient echo sequence (TR = 200 ms; TE = 20 ms; bw = 100 Hz/pixel; FA = 25°; matrix size: 64 × 64, voxel size 2 × 2 × 2 mm^3). All images were co-registered using the Insight Segmentation and

Registration Toolkit (ITK, http:// www.itk.org) (Yoo et al., 2002). The first 10 scans were averaged and used as a phase reference. The following phase images were then subtracted from this reference to get the phase difference images $\Delta\varphi$. Remaining phase wraps in these phase difference images were unwrapped using the automated phase unwrapping algorithm ΦUN (Witoszynskyj et al., 2009). Relative frequency shift maps $\Delta f/f_0$ were then determined using

$$\frac{\Delta f}{f_0} = \frac{\Delta\varphi}{2\pi\, TE f_0} \tag{4.1}$$

where TE is the echo time, and f_0 is the proton resonance frequency. The MR temperature maps (with respect to the phase reference) were then computed by putting the relative frequency shift $\Delta f/f_0$ into:

$$\Delta T = \frac{1}{\alpha}\frac{\Delta f}{f_0} = \frac{\Delta\varphi}{2\pi\alpha\, TE f_0} \tag{4.2}$$

where α = -0.01 ppm/K is the thermal PRF change coefficient (see also Section 2.3.4) (Hindman, 1966; Rieke and Butts-Pauly, 2008b). Since MR phase can only measure relative temperature changes, the MR phase temperatures were set to the fibre-optic temperatures at the beginning of the experiments.

4.1.2 Gas Composition Experiment

To verify the hypothesis of the hot air experiment in Section 4.1.1 that the observed magnetic field change inside the phantom is caused by the change in air susceptibility a second set of experiments was performed using different mixtures of gases.

Gas Composition Set-up

The set-up was very similar to the heating experiment (see Figure 4.1 and Section 4.1.1). A spherical 1 % agar gel phantom (0.9 % NaCl, diameter 8 or 14 cm) was placed in the centre of an airtight polyvinyl chloride (PVC) cylinder with a diameter of 15 cm and variable lengths (16, 27 and 56 cm) with tube connections on both ends to flood the cylinders with different types of gas (gas 1: 100 % O_2, gas 2: 50 % N_2 + 50 % O_2, gas 3: 74 % N_2 + 21 % O_2 + 5 % CO_2 and gas 4: 100 % Helium, see also Table 4.1). The carbon dioxide and oxygen content inside the airtight plastic cylinder were measured using gas analysers—part of a physiological monitoring system—to ensure that the desired gas composition completely filled the cylinder (Biopac MP150, BIOPAC Systems Inc., CA, USA). The PVC cylinder axis was always aligned parallel to the main magnetic field, and the phantom was placed in the centre of the cylinder and the CP RF coil. Coronal MR magnitude and phase images were acquired continuously throughout the experiments with the same standard 2D spoiled gradient echo sequence as in Section 4.1.1, but a voxel

Composition / %	O_2	N_2	CO_2	He	Volume Susceptibility / ppm
Gas 1	100	0	0	0	1.77
Gas 2	50	50	0	0	0.88
Gas 3	21	74	5	0	0.37
Helium	0	0	0	100	-0.001
Air at 23°C	21	78	0.04	0	0.36
Air at 69°C	21	78	0.04	0	0.27

Table 4.1: *Calculated volume susceptibilities of the gases used in the various experiments for an ambient air pressure of 1015 hPa, room temperature of 22°C and relative humidity of 50 % (Davis, 1998). The magnetic susceptibility of the different gas mixtures is dominated by the paramagnetic oxygen.*

size of $3 \times 3 \times 3$ mm^3 (repetition time = 200 ms; echo time = 20 ms; bandwidth = 100 Hz/pixel; flip angle = 25°; matrix size: 64×64).

4.2 Magnetic Field Simulation

Air/gas volume susceptibilities as a function of pressure, temperature, relative humidity, carbon dioxide, oxygen and nitrogen content were determined using the formulae given by Davis (Davis, 1998). The experimental conditions on the different days of the experiments were as follows: ambient air pressure from 1010 hPa to 1021 hPa, room temperature from 21°C to 23°C and relative humidity from 48 % to 53 %, all determined using standard equipment. The calculated volume susceptibilities for the different equilibrium air/gas conditions are displayed in Table 4.1. The calculated gas volume susceptibilities for the different conditions were then put into 3D models of the set-up. The 3D experimental configuration models comprised the spherical agar phantoms inside the sealed PVC cylinders of variable length, together with a space outside the cylindrical volume. The susceptibilities of the 1 % agar phantom, the PVC cylinders and the air outside the cylindrical box were kept constant for all the simulations using the volume susceptibilities of -9.06 ppm, -9.75 ppm and 0.36 ppm, respectively (‘‘2.6.6 Magnetic properties of materials’’ 2005; Schenck, 1996).

The field shifts of these 3D models with a matrix size of $512 \times 512 \times 512$ and the appropriate volume susceptibilities were calculated using the efficient forward simulation described by Marques and Bowtell (Marques and Bowtell, 2005; Schäfer et al., 2009). This forward simulation approximates the magnetic field distribution due to a susceptibility distribution using a Fourier transform approach and was implemented in C++ on a quad-core PC using the ODIN libraries (Jochimsen and

Von Mengershausen, 2004). The computed magnetic field distributions for the different equilibrium air/gas conditions were then subtracted in the same way as the MR phase reference and the rest of the phase images to obtain relative magnetic field shift maps $\Delta B/B_0$ and relative frequency shift maps $\Delta f/f_0$, which could then be compared with the relative frequency shift maps $\Delta f/f_0$ obtained with the MR phase images. Since B_0 and f_0 are related by $f_0 = \frac{\gamma}{2\pi}B_0$ (γ - proton gyromagnetic ratio, see Section 2.1), the relative magnetic field shift maps $\Delta B/B_0$ and the relative frequency shift maps $\Delta f/f_0$ are equal.

4.3 Results

4.3.1 Hot Air Experimental Results

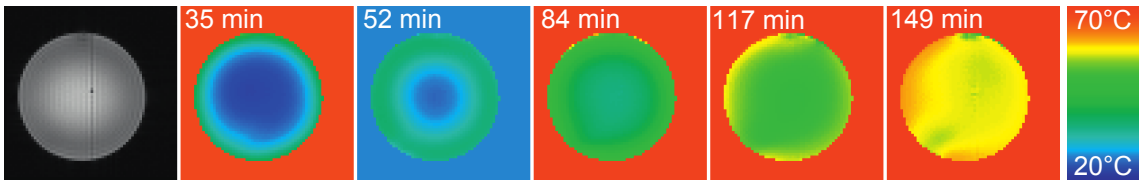

Figure 4.2: *Magnitude image and successive MR phase temperature maps (times on each figure) during the hot air heating experiment. The background colour indicates the air temperature (see also Figure 4.3).*

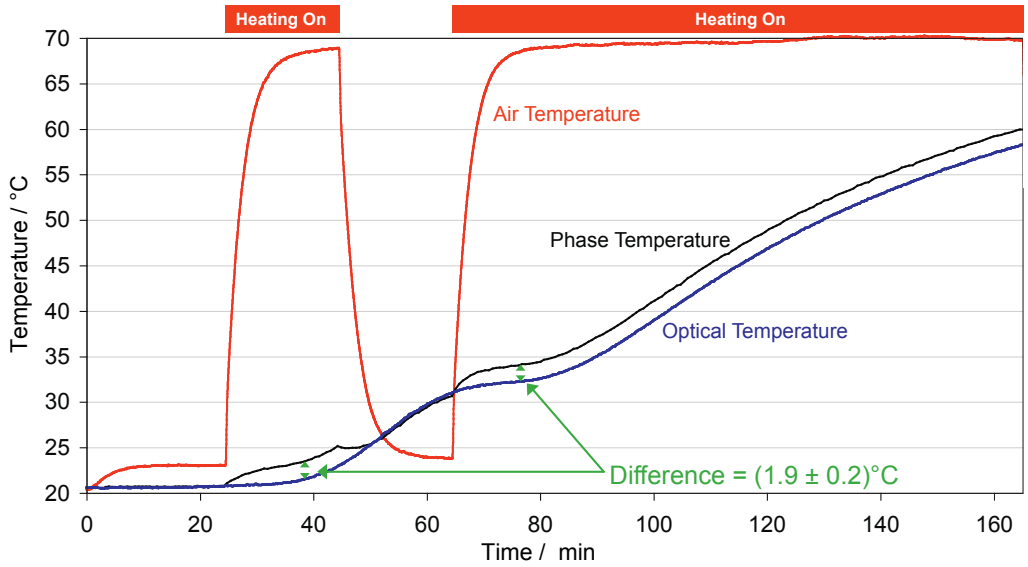

Figure 4.3: *Time course of temperature derived from phase measurements and from fibre-optic thermometer measurements during the hot air experiment. As the surrounding air temperature (red line) increases, the MR phase temperature (black line) deviates from the fibre-optic temperature (blue line). As the air temperature returns to its initial temperature, the MR phase and fibre-optic temperature again converge.*

Figure 4.2 shows a GRE magnitude image of the phantom and several temperature maps during the experiment. Figure 4.3 displays the results of the hot air heating experiment for a single voxel in the centre of the phantom at the fibre-optic thermometer location. At the beginning of the experiment, the hair dryer blew air (with a temperature of 23°C and a volume susceptibility of (0.36 ± 0.01) ppm) through the piping into the cylinder holding the phantom inside the scanner. The air outside the box remained at room temperature during the entire experiment. After about 25 min, the heating of the hair dryer was turned on, and after 20 min (at time 45 min), the maximum air temperature of 69°C was reached inside the box resulting in an hot air volume susceptibility of (0.27 ± 0.01) ppm. This air temperature increase also caused a slow heating of the spherical phantom.

However, as the temperature inside the cylinder increased, the MR phase temperature started to deviate from the fibre-optic temperature simultaneously with the surrounding air temperature increase, reaching a maximum deviation of (1.9 ± 0.2) K (see Fig. 4.3). After 20 min of blowing hot air through the box around the phantom, the heating was turned off, and air at room temperature was blown through the set-up. The air surrounding the phantom quickly returned to a temperature of 23°C. As the air temperature returned to its initial temperature of 23°C, the MR phase temperature and the fibre-optic temperature again converged. The temperature increase measured with both methods while room temperature air was in the cylinder is caused by heat diffusing from the outer part of the phantom into the centre of the phantom (where the fibre-optic thermometer and voxel of interest were placed). At the 65th minute, the heating of the hair dryer was turned on again, and about 20 min later, the air temperature around the phantom again reached 69°C. As previously, the deviation between the MR phase and fibre-optic temperature reached (1.9 ± 0.2) K. This difference remained constant until the end of the experiment.

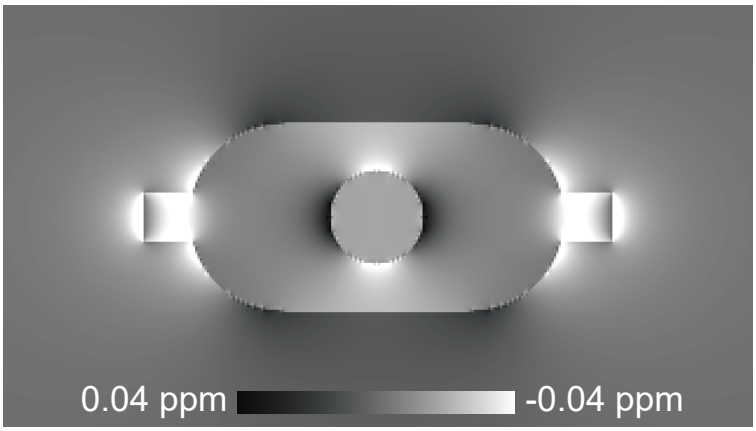

Figure 4.4: *Simulated field shift of the hot air experiment when the air inside the box reached 69°C with a volume susceptibility of 0.27 ppm. The magnetic field inside the spherical phantom in the centre of the set-up shifted by (-0.0181 ± 0.0007) ppm, which translates to a MR phase temperature change of (1.81 ± 0.07) K (cf. the measurement in Fig. 4.3). The volume susceptibility of air at 23°C was approximately 0.36 ppm (see also Table 4.1).*

In Fig. 4.4, the simulated relative magnetic field shift map $\Delta B/B_0$ for the hot air experiment is displayed. The field inside the phantom (sphere in the centre) is almost homogeneous and displays a shift of (-0.0181 ± 0.0007) ppm when the air temperature changes from 23 to 69°C. This field shift would yield a measured MR temperature shift (if no correction method is applied) of (1.81 ± 0.07) K.

4.3.2 Gas Composition Results

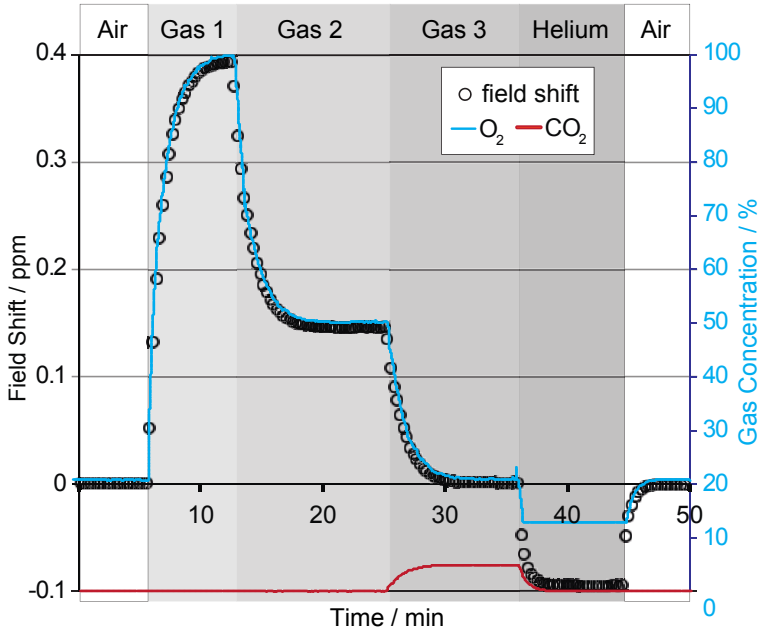

Figure 4.5: *Relative magnetic field shift (black circles) measured with MR phase over an 8 voxel ROI in the middle of the 8 cm phantom, which was centred within the 56 cm length PVC cylinder. The blue and red lines are the measured O_2 and CO_2 concentrations inside the cylinder, respectively. The measured relative magnetic field shift follows closely the oxygen concentration, except when helium gas surrounded the phantom, which is due to an error of the gas analyser of the physiological monitoring system. For the gas susceptibilities and composition see Table 4.1. The field shift map for 100 % O_2 is shown in Figure 4.6.*

Composition / %	O_2	N_2	CO_2
Gas 1	100	0	0
Gas 2	50	50	0
Gas 3	21	74	5

Table 4.2: *Gas composition of the 3 gases used in Figure 4.5. For the gas susceptibilies see Table 4.1.*

Figure 4.5 shows the result of one of the gas composition experiments with the 8 cm diameter phantom inside the 56 cm long sealed PVC cylinder. The black circles are the MR field shift for an 8 voxel region of interest (ROI) in the centre of the phantom overlaid on the gas concentration readings of O_2 (blue line) and CO_2 (red line) around the phantom. In the baseline condition at the beginning and the end of the experiment, the cylinder contained ambient air. Starting after about 5 minutes, the gases in Table 4.2 and 100 % Helium were continuously injected into the sealed PVC cylinder for about 10 min each. The different gaseous mixtures caused relative magnetic field shifts ranging from -0.1 to 0.4 ppm, as measured using MR phase. The measured field shift closely follows the modulations of O_2 concentration, except when the cylinder was filled with 100 % Helium.[4]

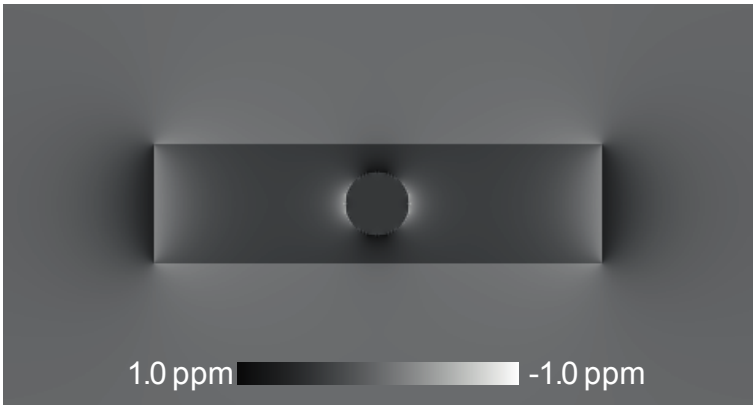

Figure 4.6: *Calculated field shift map for the 8 cm phantom inside the 56 cm length cylinder of 15 cm diameter. The map shows the field shift when air in the cylinder is replaced by 100 % O_2. The volume susceptibilities used for the simulation are given in Table 4.1.*

Figure 4.6 shows the simulated magnetic field shift map for gas 1 (100 % O_2) for the 8 cm diameter phantom inside the 56 cm cylinder (diameter 15 cm). The results of the measurement are presented in Fig. 4.5. Again, as in Fig. 4.4, the field shift inside is almost homogeneous but with a much higher value of (0.429 ± 0.007) ppm.

Figure 4.7 and Table 4.3 demonstrate the strong dependence of the effect on the experimental configuration and its linear dependence on susceptibility change. The three set-ups with the same phantom (diameter 14 cm), but different cylinder lengths (56 cm — dashes, 27 cm — solid black, 16 cm — solid grey) cause significantly different relative magnetic field shifts when the cylinder is filled with O_2. The lines are the results obtained with the Fourier field simulation (Marques and Bowtell, 2005). The circles are the measured field shifts in the centre of the phantom for the different gases (errors are much smaller than the displayed data points). The field shift measured for the longest O_2 filled cylinder with the large phantom is (0.404 ± 0.004) ppm, compared with the simulated value of (0.429 ± 0.007) ppm. A list of field shift values for the O_2 filled cylinders is found in Table 4.3.

[4]The error in O_2 concentration for 100 % Helium is due to an error in the gas analyser system.

phantom diameter / cm		8		14	
		Meas.	Simu.	Meas.	Simu.
cylinder length / cm	16	0.091	0.097	0.101	0.096
	27	0.276	0.301	0.287	0.301
	56	0.392	0.430	0.404	0.429

Table 4.3: *Relative magnetic field shifts inside the phantom when air in the cylinder surrounding the phantom (χ_{air} = 0.27 ppm) was replaced by pure O_2 (χ_{air} = 1.77 ppm, see Table 4.1). The MR phase temperature change is obtained by multiplying the field shift by -100.*

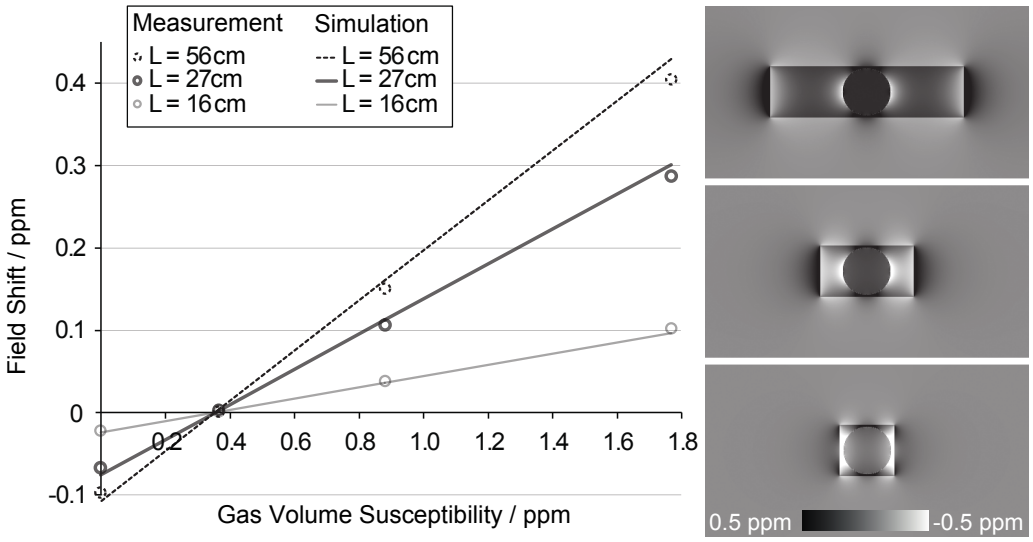

Figure 4.7: *Dependence of relative field shift on experimental configuration and susceptibility change. The lines display the results of the field shift simulation, while the circles are the measured MR field shifts for a ROI in the centre of the phantom (14 cm phantom diameter). The length of the enclosing cylinder was varied (56 cm — dashes, 27 cm — solid black, 16 cm — solid grey), and the gas volume susceptibility was modulated using the different gases in Table 4.1. Field shifts increase with the length of the cylinder and the volume susceptibility change. On the right-hand side, the relative field shift simulation when air was replaced by 100 % O_2 is displayed, for each set-up.*

4.4 Discussion

The experiments and simulations have shown that changes in the surrounding gaseous medium can alter the magnetic field inside an object and that MR phase imaging is sensitive enough to detect these changes. The considerable impact on PRF MR thermometry was demonstrated and quantified for simple experimental set-ups. First, the influence of changes in air temperature was measured and simulated. When the surrounding air was heated from 23 to 69°C, the MR phase temperature and the fibre-optic temperature differed by (1.9 ± 0.2) K (see Fig. 4.3). This difference disappeared as the surrounding air temperature returned to 23°C. Since the air flow

was on continuously for both cold and hot air, this discrepancy cannot be explained by movement of the phantom when switching from cold to hot air. Furthermore, the deviation between the measured MR temperature and the temperature sensor appeared simultaneously with the air temperature increase and similarly, disappeared simultaneously when the air cooled down. The deviation also closely matched the simulation, which yielded a field shift that translated to (1.81 ± 0.07) K deviation when a volume susceptibility change from 0.36 to 0.27 ppm was assumed for the surrounding air volume (cf. Fig. 4.4) (Marques and Bowtell, 2005). In addition, the measured temperature difference remained constant until the end of the experiment. When the hot air induced temperature shift was subtracted from the MR phase temperature, the mean difference between the fibre-optic thermometer and the MR phase temperature was (-0.1 ± 0.1) K between the 100th and 150th minute of the experiment. Thus, PRF thermometry remains accurate if this temperature error is considered, or if the reference image is acquired after the surrounding susceptibility change has occurred.

Although the phantom has a non-uniform temperature distribution when heated, the measured magnetic field shift is independent of phantom temperature, most likely due to the small temperature dependence of the water magnetic susceptibility (Schenck, 1996). The field shift is predominantly determined by the outside susceptibility change and the experimental configuration. For this experimental set-up, and assuming a homogeneous air temperature, the magnetic field shift inside the phantom induced by change of air temperature is almost uniform, to better than 4 %. Even for an inhomogeneous air temperature distribution, the field shift inside the phantom is fairly homogeneous. Simulations of a worst case scenario, assuming an air temperature gradient of 20 K, show that an error in the measured temperature of only 0.3 K is expected.

The volume susceptibility change of the air is mainly due to its expansion with increasing temperature (at constant pressure, $\sim 1/T$ dependence) as well as the fact that oxygen paramagnetism obeys the Curie law ($\sim 1/T$ dependence) and therefore has an approximate $1/T^2$ dependence (Davis, 1998). The effect of air temperature change on MR thermometry is subtle and, in most cases, will not lead to deviations of more than a few Kelvin. Moreover, as the effect is non-local and caused by external susceptibility changes, it can be readily corrected with many of the strategies used in MR thermometry, like the reference-less approaches or fat referenced approaches (de Senneville et al., 2010; Salomir et al., 2012; Sprinkhuizen et al., 2010a; Streicher et al., 2014). By contrast, a change in the gaseous composition of air can result in a much greater susceptibility change.

The volume susceptibility of air is primarily determined by the paramagnetic O_2 molecular content (Schenck, 1996). This has also been observed in echo-planar imaging where oxygen concentration changes in air can lead to image distortions (Raj et al., 2000).[5] Figure 4.5 demonstrates that the measured relative field shift closely

[5] As described in Section 2.2.3 these distortions are mostly in the phase-encoding direction.

follows the oxygen concentration over the course of the experiment. Only for gas 4 (100 % Helium), does the oxygen concentration not follow the field shift. This discrepancy is likely to be related to the calibration of the gas analyser of the physiological monitoring system, which was performed at a high O_2 concentration, leading to inaccurate O_2 readings at low concentrations.

Because the susceptibility of air is mainly determined by O_2, and the field shift scales linearly with susceptibility change (cf. Fig. 4.7), the largest field shift occurs when the surrounding cylinder is completely filled with oxygen. In this case, the surrounding volume susceptibility changed from 0.36 ppm (air) to 1.77 ppm (100 % O_2), causing an experimentally determined field shift of (0.392 ± 0.003) ppm, which is close to the value of (0.429 ± 0.007) ppm obtained by the field simulation. The discrepancy of 0.037 ppm between the measured and simulated field shifts might be explained by the high sensitivity of the effect to the exact experimental configuration. Figure 4.7 demonstrates the dependence on the experimental configuration more clearly. As the cylinder length is changed, the maximum field shift in the centre of the phantom (again for 100 % O_2) varies from (0.102 ± 0.002) to (0.404 ± 0.006) ppm for the short and long cylinder, respectively. These field shifts would translate to MR temperature errors of (10.2 ± 0.2) and (40.4 ± 0.6) K. If the susceptibility change of the surrounding medium is inhomogeneous or the experimental configuration is non trivial, the field shifts will generally also be inhomogeneous over the imaged volume. Therefore, simple correction methods might not be sufficient (e.g. with just a few reference points). In contrast, more elaborate methods such as the reference-less approaches should be able to correct the induced error (Rieke et al., 2004; Salomir et al., 2012). The main implication of these results for in vivo applications is the need for careful calibration methods, especially in interventional settings, when oxygen is often added to the breathing gas. The results are also relevant to small-bore systems, where animals are often heated to maintain their physiological state and supplied with various gases for experimental purposes (Hedlund et al., 2000). An easy solution would be to measure the reference images after the surrounding susceptibility change has occurred.

4.5 Conclusion

MR thermometry is influenced by susceptibility changes of surrounding air. It was demonstrated that changes in oxygen concentration have the strongest influence on the magnetic field distribution and therefore on uncalibrated MR thermometry. The temperature errors can be as large as 40 K. Air susceptibility also varies with air temperature, but this effect is much smaller. For the used set-up, the error reached 2 K when the surrounding air was heated to 69°C (temperature change of 46 K). For an air temperature change of 10 K, the resulting error can still be as large as 0.75 K, depending on the experimental set-up. The strong dependence on the experimental configuration was also demonstrated. The size of the effect quadrupled going from

the shortest to the longest gas-filled cylinder around the phantom. It is also worth noting that this set-up could also be used to measure the susceptibility of gases or liquids.

Chapter 5

Spin-echo MR Thermometry

At the beginning of this thesis work it became clear that at high field referenced MR thermometry is a good way to do accurate temperature mapping across the whole imaging volume (Rieke and Butts-Pauly, 2008b). Water is used for temperature sensitivity and a reference substance with a different thermal PRF change coefficient for magnetic field perturbation sensitivity (Ishihara et al., 1995).[1] While searching for an appropriate MR thermometry sequence and an appropriate reference substance, Dr. Dimo Ivanov at the Max Planck Institute for Human Cognitive and Brain Sciences discovered a neat and efficient frequency-selective spin-echo method (Ivanov et al., 2010).[2] The Ivanov method is relatively insensitive to B_1 inhomogeneities, has low SAR and allows fast acquisitions using EPI. Similar to the novel technique of Ivanov is the gradient reversal technique which was used for the in-vivo measurements (Park et al., 1987; Volk et al., 1987). In this chapter which is partially based on the publication 'Fast Accurate MR thermometry Using Phase Referenced Asymmetric Spin-Echo EPI at High Field' a novel high field approach for referenced MR thermometry using both frequency-selective SE techniques is presented (Streicher et al., 2014).[3] The novel technique was tested in three MR temperature experiments and additionally evaluated in extensive Bloch simulations and MR scans.

5.1 Methods & Materials

The referenced MR thermometry approach is based on the alternate acquisition of two separate images of two different frequency bands. One frequency is set to water

[1] Interestingly, Ishihara et al. in 1995, who acquired the first MR phase temperature maps, already mentioned the necessity of a reference substance like fat.

[2] Dimo Ivanov, Andreas Schäfer, Markus N. Streicher, Robin M. Heidemann, Robert Trampel, Robert Turner. A Simple Low-SAR Technique for Chemical-Shift Selection with High-Field Spin-Echo Imaging. Magn Reson Med 2010;64(2):319-326.

[3] Complete author list: Markus N. Streicher, Andreas Schäfer, Dimo Ivanov, Dirk K. Müller, Alexis Amadon, Enrico Reimer, Laurentius Huber, Bibek Dhital, Debra Rivera, Carsten Kögler, Robert Trampel, André Pampel, Robert Turner.

frequency and the other frequency is set to the reference substance frequency.[4] In the next section the frequency-selectivity of the approach is discussed in more detail.

5.1.1 The Phase-sensitive Frequency-selective SE Sequence

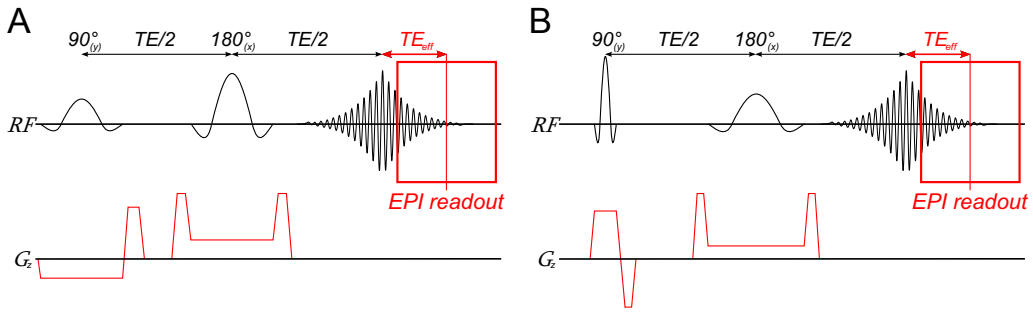

Figure 5.1: *(A) Gradient reversal asymmetric SE (ASE) technique. Frequency-selectivity is achieved by different slice-select gradient polarities for excitation and refocusing. (B) ASE Ivanov technique (Ivanov et al., 2010). The different slice-selective gradient amplitudes make the sequence frequency-selective. Phase-sensitivity is achieved by moving the EPI readout back in time. The time between the spin-echo and the k-space centre of the EPI readout is called* TE_{eff}.

Sketches of the sequences are displayed in Figure 5.1. To achieve frequency-selectivity, both techniques require that the excited and refocused slices of the unwanted species/frequency do not overlap in space, so that any transverse magnetisation of the unwanted species remains unrefocused, and is eliminated by the gradients of the refocusing pulse (see also Fig. 5.3). This lack of spatial overlap can be easily achieved by changing the duration or bandwidth-time product of the RF pulses.

The main difference between the gradient reversal technique and the Ivanov technique is the choice of gradient polarities for excitation and refocusing. While the Ivanov approach applies slice-select gradients of the same polarity but different amplitude for excitation and refocusing, the gradient reversal method uses gradients of differing polarity, but typically the same amplitude, for excitation and refocusing.

A standard Siemens SE EPI sequence was modified to be frequency-selective by changing the duration of the RF-pulse and in case of the gradient reversal technique by changing the gradient polarity of the excitation pulse. To provide phase sensitivity, the centre of the EPI readout ($k_{Read} = 0$ and $k_{PE} = 0$) was shifted in time, to be reached later than the spin-echo (Fig. 5.1), thus imparting T_2^* weighting to the signal. The time between the spin-echo and the k-space centre of the readout is called TE_{eff}. The scanner frequency was then alternately set to the water frequency and the reference substance frequency. Additionally, the SE EPI sequence was modified

[4]This referenced MR thermometry technique requires that the water and reference substance frequencies be far enough apart.

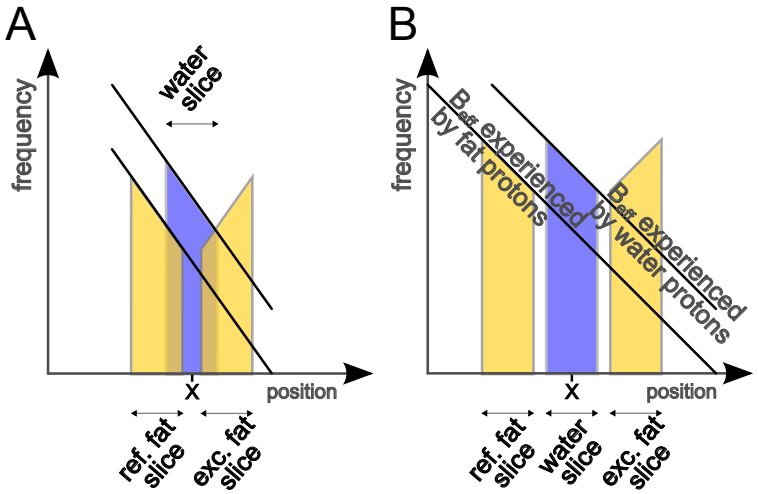

Figure 5.2: *Position of the water (blue) and fat (yellow) slice along the slice-select gradient for the gradient reversal technique when water is imaged. The position of the excited and refocused water (position X) and fat slices are shown after the refocusing RF-pulse when water is imaged. (A) For simple frequency-selectivity it is sufficient that the excited and refocused fat slice do not overlap and thus produce no refocused fat signal. This can simply be done by increasing the duration of the RF-pulses. However, the excited and refocused fat slices may (as in Figure A) in general overlap in space with the desired water slice. Therefore the fat magnetisation at the position of the imaged slice is partially saturated and inverted. Fast sequential water and fat imaging would therefore give a high SNR water image and a low SNR fat image. (B) Because the fat reference image is acquired at exactly the position of the water slice, there must be no overlap between the imaged slices and the excited and refocused slices of the unwanted species to achieve a high SNR in the water and the fat image. This can be achieved by further increasing the duration of the RF-pulses and therefore reducing the gradient amplitude for a given slice thickness (see also Figure 5.3 and Section 2.4.2 for the theory of the gradient reversal and the Ivanov method).*

to acquire water and reference substance images alternately, at the same position in space by changing the scanner frequency and with an adaptable time delay between the water and reference substance acquisition. For the Ivanov technique the delay between the water and reference substance (in this case DMSO) acquisition was on the order of seconds (see Section 5.2.1). For the in-vivo experiment (Section 5.2.3) the gradient reversal method was applied in order to minimize the time delay between water and reference substance acquisition to 50 ms. It is desirable to minimize the time between the water and the reference substance acquisition in order to correct also for fast magnetic field perturbations like heart beat, movement or breathing. Scalp and skull marrow fat were used as a reference for the in-vivo experiment.

To acquire water and fat slices at the same position and in rapid succession using the gradient reversal method (see Figures 5.1A and 5.2) imposes more stringent conditions on the frequency-selectivity than for water or fat selection alone. Normally, for proper suppression it is enough that the excited and refocused slices of the

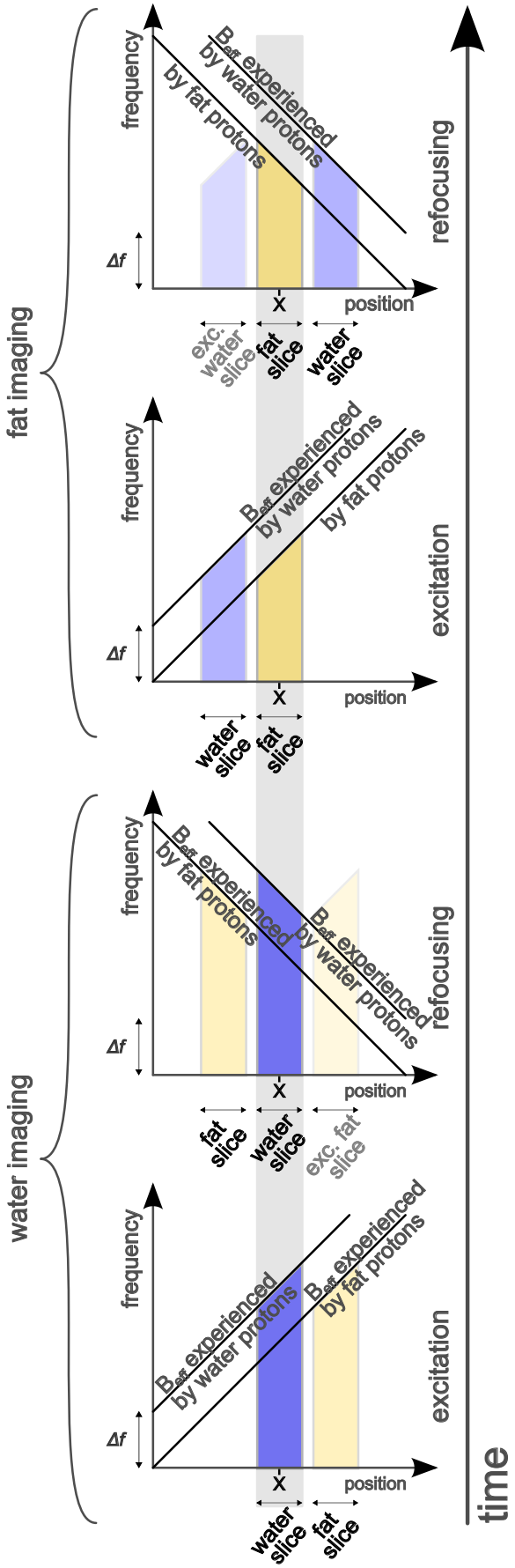

Figure 5.3: *The figure illustrates the slice positions of the excited and refocused fat and water slices for the in-vivo gradient reversal ASE sequence (see Section 5.2.3 on the in-vivo MR thermometry experiment). During slice-selective excitation and refocusing, the two chemical species of interest, water and fat, are displaced in the slice direction depending on gradient amplitude, gradient polarity and chemical shift of the species ($f_{H_2O} - f_{fat} \approx 1000$ Hz at 7 T). For referenced in-vivo temperature measurements the excitation and refocusing slice position of the unwanted chemical species are displaced so far from the imaging position (position X) that this species can be immediately imaged afterwards (i.e. the slices of the wanted and unwanted chemical species do not overlap). Thus, there is no loss in signal of the reference substance due to saturation of the spin magnetisation caused by imaging the water at the same location.*

unwanted species do not overlap. Here the refocusing pulse merely inverts the slice of the unwanted species that has not been previously excited, leaving no focused transverse magnetisation to be imaged.[5] However, the excited and refocused slices of the unwanted chemical species may in general overlap in space with the slice of the desired chemical species as displayed in Figure 5.2. Consequently, the unwanted species is partially saturated or inverted at the position of the slice to be imaged, even though it does not contribute to the image. Rapid sequential water and fat slice acquisition at the same spatial position would, therefore, give a high SNR water image, but a low SNR fat image, because the fat signal would not yet have recovered from its saturation (assuming a long TR between acquisition pairs). To achieve a high SNR in both the water and the reference images, there must be no overlap between the water image slice and either the excitation or the refocusing slice of the unwanted chemical species (e.g. fat, when water is imaged). For the gradient reversal technique an increase of the RF pulse duration increases the separation between the excited and refocused slice of the unwanted chemical species (see Fig. 5.2 and Fig. 5.3).

5.1.2 DMSO as a Reference Substance

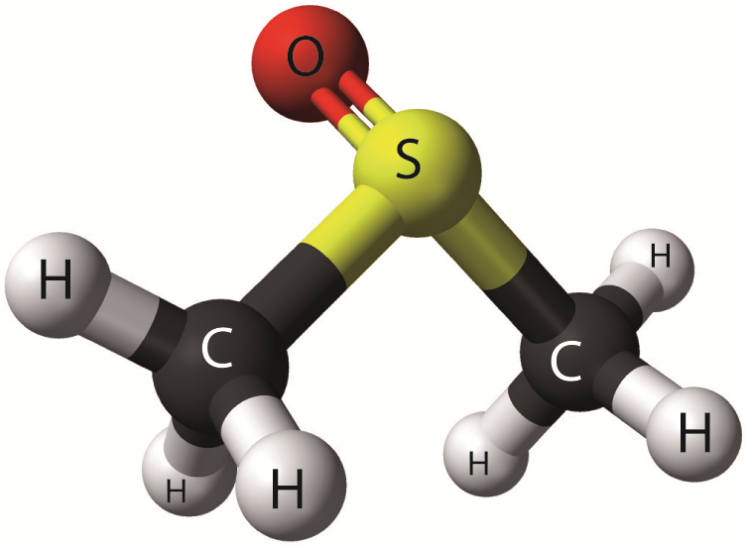

Figure 5.4: *Dimethyl sulfoxide (DMSO) has the formula $(CH_3)_2SO$. It is a colorless liquid that dissolves both polar and nonpolar compounds and is in any ratio miscible with water. DMSO penetrates the skin readily and any substances dissolved in DMSO can easily be absorbed, therefore appropriate gloves are very important. Common nitrile gloves are not sufficient. The physical properties are: density 1.1 g/cm^3, melting point: 19°C, boiling point: 189°C (from Wikipedia: Stereo structural formula of dimethyl sulfoxide, accessed 28 Mar. 2016).*

DMSO was used as an internal reference for the phantom experiments (sections 5.2.1 and 5.2.2) due to its miscibility with water, low toxicity and its single

[5]The spoiled excited and inverted slice is nicely depicted in Figure 5.15.

NMR ^{1}H peak (see Fig.: 5.5). The structure of DMSO is depicted in Figure 5.4. The six hydrogen protons of DMSO have a single resonance peak shifted at room

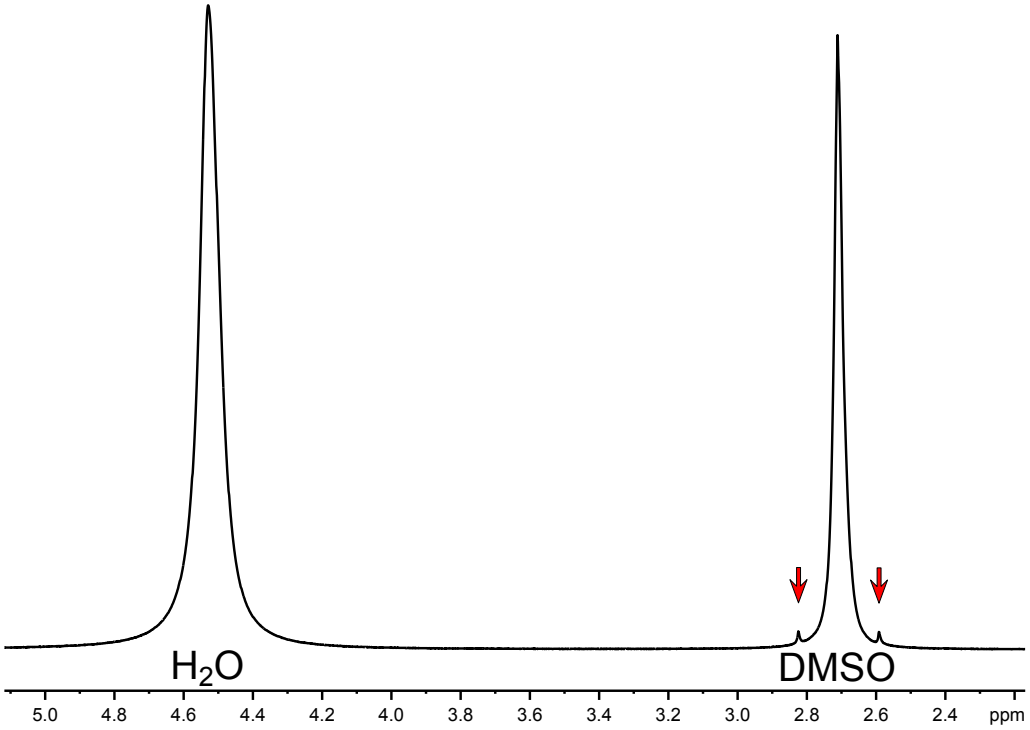

Figure 5.5: *^{1}H NMR spectrum of the 64 % H_2O and 34 % DMSO (plus 1 % agar and 1 % NaCl) sample at 37°C acquired on a temperature-calibrated 600 MHz spectrometer (Bruker BioSpin, Germany). The water peak is at 4.53 ppm and the DMSO peak is at 2.71 ppm. The small symmetric peaks (red arrows) around the DMSO peak are ^{13}C satellites (Fujiwara et al., 1972).*

temperature by approximately -2 ppm relative to water protons, resulting in a frequency shift of -600 Hz at 7 Tesla (Mizuno et al., 2000).[6] This frequency difference is smaller than the water-fat PRF difference ($f_{H_2O} - f_{fat} \approx 1000$ Hz and $f_{H_2O} - f_{DMSO} \approx 600$ Hz at 7 T), which puts stronger constraints on the frequency-selectivity of the suppression technique (see Section 5.1.1 and 5) (Sprinkhuizen and Bakker, 2012). However, this drawback is made up for by the miscibility of water and DMSO, and the long T_2 and T_2^* values of water ($T_2 = 82$ ms and $T_2^* = 75$ ms) and DMSO ($T_2 = 274$ ms and $T_2^* = 140$ ms) in the mixture (64 % H_2O, 34 % DMSO, 1 % agar and 1 % NaCl), which were much larger than the values attainable for water and fat mixtures.

T_2 and T_2^* values of H_2O and DMSO in the mixture were measured using the phase sensitive frequency-selective SE technique described in this thesis and in detail in Section 5.1.1. T_2 and T_2^* values were estimated using an exponential fit to the frequency-selective magnitude images of H_2O and DMSO when TE and TE_{eff} were varied separately.

[6] Also visible are the ^{13}C satellites of the ^{1}H DMSO peak. About 1 % of the Carbon atoms are ^{13}C isotopes with spin 1/2. Hydrogen atoms J couple with the adjacent ^{13}C atoms and result in a wide ^{1}H doublet (Fujiwara et al., 1972).

The relative thermal PRF coefficient of water with respect to DMSO was experimentally determined to be -0.0098 ppm/K (very similar to the thermal PRF coefficient of pure water) for a H_2O mole fraction $x\,(H_2O) = 0.89$ using a temperature-calibrated 600 MHz spectrometer (Bruker BioSpin, Germany).[7] The relative thermal PRF coefficient was determined for the phantom mixture used in this study, since it depends on the DMSO concentration. For H_2O mole fractions $x\,(H_2O)$ from 0.89 to 0.96, a linear dependence of the relative thermal PRF coefficient: $\alpha_{relative}\,(x) = (-0.007314 \cdot x - 0.003294)$ ppm/K was measured.

5.1.3 Temperature change calculation

Magnitude and phase images were reconstructed for each channel separately. Syngo - the Siemens scanner software - does not allow to reconstruct magnitude and phase images for all the coil elements and several hundred repetitions separately. Therefore, *odinreco* which is part of the extensive and very useful ODIN libraries was used to reconstruct all the magnitude and phase images of each coil element separately (Jochimsen and Von Mengershausen, 2004).[8] Temperature maps were then computed by software implemented in C++ using ODIN libraries, performing the following computations. The magnitude and phase images were combined into complex images, and the interleaved water and reference time-series were split up. The measured MR phase of each voxel and channel is a sum of many contributions, such as the spatially varying phase of the transmit or receive coils, eddy currents and for the presented sequences on the spin-echo phase φ_{SE} and $\varphi_{TE_{eff}}$, the phase accumulated during the effective echo time TE_{eff} due to changes in B_0 and temperature (see also Section 2.3.4) (Katscher et al., 2009; Liu et al., 2013; Van de Moortele et al., 2005). For the calculation of the temperature change, it is assumed that only $\varphi_{TE_{eff}}$ changes with the Larmor frequency and therefore with temperature. Complex channel-specific reference scans were acquired at the beginning of the time-series. To remove the spatially varying receive phase from each receive channel, and later to allow an optimal combination of the respective data, the channel-specific phase reference data was voxelwise subtracted from the MR phase time-series of each of the 8 individual receive channels.[9] This was performed separately for the water and reference substance, to obtain the phase change over time of each voxel measured by each coil element for water and fat (Bernstein et al., 1994; Robinson et al., 2011). The channel-specific phase difference time-series were then combined using magnitude-squared weighting to form a single water and reference time-series (Reeder et al., 2004). Uncorrected MR temperature maps were

[7]Technical support by the Institute of Analytical Chemistry, University of Leipzig, is gratefully acknowledged.

[8]The GRAPPA reconstruction has the advantage of generating separate images for each coil element (Griswold et al., 2002).

[9]In this way the weighting coefficients for coil combination do not have to stay constant (Bankson et al., 2005).

then obtained according to the PRF phase shift method using the water phase time-series (see Section 2.3.4 and Rieke and Butts-Pauly, 2008b).

Referenced MR Temperature

To obtain corrected water temperature maps using a fat or dimethyl sulfoxide (DMSO) reference, the following additional operations were required. Because the Larmor frequency of the reference substance is offset from that of water, images of the reference substance needed to be spatially shifted, so that the water and reference substance images were properly co-registered.[10] The reference substance image was thus moved in the read direction by $\Delta x = \Delta f \cdot t_{single}$ where Δx is in pixels, and Δf is the frequency offset of the reference substance with respect to the water resonant frequency and t_{single} is the readout duration for a single line (see Section 2.2.3 on the imaging bandwidth). The reference substance image was also moved by $\Delta y = \Delta f \cdot t_{complete}$ pixels in the phase encoding direction, where $t_{complete}$ is the duration of the complete EPI readout (Jezzard and Balaban, 1995).

To reduce the noise contributions in the phantom reference-substance time-series, the DMSO time-series was smoothed using a Gaussian kernel of 4 voxels (full width at half maximum) for each slice and repetition. This smoothing procedure could not be applied to the in-vivo measurements, since here the fat reference does not spatially overlap with the temperature sensitive water image of the brain. In the healthy brain, a fat signal is seen only in the scalp and skull marrow; brain tissue lipids are not observed in standard MRI due to their short T_2 (Buxton, 2009). Instead of smoothing, the MR phase change of the fat reference times-series was fitted by a 2D linear function for each time-step and slice. The 2D fit was done to obtain an estimate of the field changes, aimed to correct, at every voxel inside the brain. The phase change of these adjusted reference substance time-series were then converted to apparent temperature change time-series in the same way as the water phase change described above. These reference-substance apparent temperature time-series were then subtracted from the water temperature time-series, to finally obtain the reference-corrected water temperature maps.

5.1.4 Bloch Simulation

To investigate the frequency-selectivity and phase shifting effects of both SE techniques (see Fig. 5.1) as a function of flip angle and off-resonance frequency, Bloch simulations were performed. The simulation was based on a matrix exponential solution to the Bloch equations described in Section 2.7 (Allard and Helgstrand, 1997; Helgstrand et al., 2000). The simulation algorithm was implemented in Matlab (MathWorks, USA). The simulations involved 4096 isochromats distributed along the z-direction of a 10 mm slab. This resolution was high enough to determine all

[10] It would have also been possible to set the receive frequency of the scanner to the water or reference substance as it is done for excitation and refocusing.

the features of interest, and a higher resolution did not change the results of the simulation. The gradient and RF waveforms were exported from the MR IDEA sequence development environment (Siemens Healthcare, Germany) with a temporal resolution of 5 μs. Except for the crusher gradients sandwiching the refocusing pulse, all sequence objects were simulated exactly as used on the scanner. The crusher gradients were increased to mimic their true efficiency and to avoid simulation errors (Jochimsen et al., 2006). The net magnetisation at the time of the spin-echo was calculated by complex summation across the complete simulation width for frequency offsets ranging from -1000 Hz to 1000 Hz and excitation flip angle from 5° to 180°.

For both frequency-selective SE techniques, the Bloch simulations show that the MR phase of the refocused spin magnetisation is a function of frequency offset and flip angle (Fig. 5.16 B and D and Fig. 5.17). However, the calculation of the temperature change assumes a constant MR phase of the spin-echo. Since the temperature change is determined by a frequency change, this frequency-dependent MR phase shift can lead to a systematic error in the measured temperature change. This error depends on the rate of change of the spin-echo MR phase with frequency offset. A longer effective echo time TE_{eff} reduces the relative error, because the phase shift produced by the change of temperature is then proportionately larger. The method can thus be made less sensitive to the additional sequence-induced phase shift $\Delta\varphi_{SE}$ by maximizing the phase change $\Delta\varphi_{Temp}$ associated with the temperature-induced frequency change. The phantom studies used a TE_{eff} = 19 ms, which made them rather less sensitive to this sequence-induced phase shift than the in-vivo study, which used a TE_{eff} = 12.6 ms.

5.2 Experiments

All imaging experiments were performed on a 7 T whole body scanner (Siemens Healthcare, Germany) with an 8-channel head-array RF coil (RAPID Biomedical, Germany). The modified actual flip angle technique was used to ensure that the achieved flip angle for the excitation pulse was no greater than 120° in the slices imaged (Amadon and Boulant, 2008; Nehrke, 2009; Yarnykh, 2007). In addition, the modified actual flip angle technique was used to measure B_0 inhomogeneity to ensure chemical selectivity of the SE sequences. The in-vivo study was approved by the local ethics committee and all subjects gave informed consent.

5.2.1 RF-heating Coil Experiment

Set-up

To provide RF heating to the phantom, a custom-built shielded circular surface coil (10 cm diameter) was placed on top of the phantom, parallel to the coronal imaging slices and inside the 8-channel imaging RF coil. This caused RF shadowing,

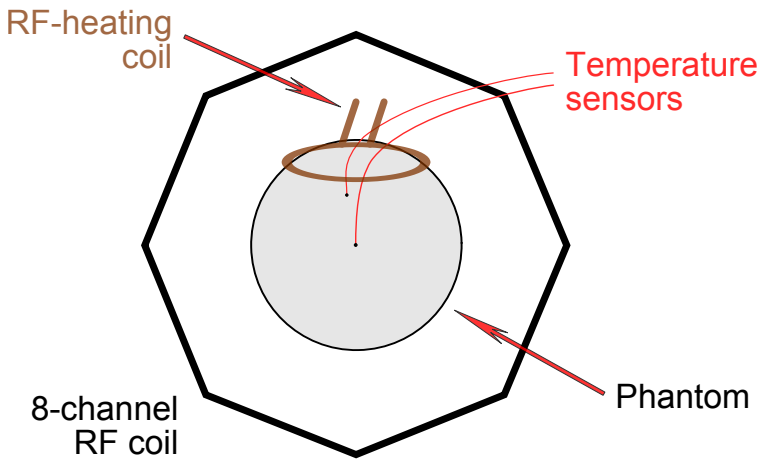

Figure 5.6: *RF-heating coil set-up. The DMSO/water phantom was placed in the centre of the 8-channel head-array RF coil with the 125 MHz heating coil placed on top of the phantom. Two temperature sensor were inserted from above at different positions.*

resulting in a low signal in some parts of the phantom close to the heating coil.[11] The heating coil was matched to 50 Ohm with a capacitive matching network and tuned to 125 MHz. The value of 125 MHz was chosen in order to heat the phantom while mapping the temperature with the head-array coil at 297.2 MHz (PRF at 7 T). However, due to remaining image noise caused by the 125 MHz coil, the heating amplifier was triggered, by the imaging sequence and only every second TR was used for heating. The images acquired during the heating TR period were not considered for evaluation.

A spherical phantom (diameter 15 cm), containing a homogeneous mixture of 34 % DMSO, 64 % water, 1 % agar and 1 % NaCl was used for measurements (in mass percent). The heating coil was connected to a 10 W RF amplifier (M68721, Mitsubishi, Japan). To heat, approximately 8 W of triggered power were applied for 2 hours (on average 4 W). In addition, the temperature in the phantom was monitored at two locations (sensor 1 approximately 5 cm and sensor 2 approximately 7 cm away from the heating coil) with fluoroptic temperature sensors (Luxtron Lumasense, USA). Imaging was performed using the modified Ivanov technique (see Section 2.4.2 and Ivanov et al., 2010). This modified ASE sequence is presented in Figure 5.1B. To achieve good separation of the water and DMSO proton signal, the duration of the excitation RF-pulse was set to 1.8 ms and the refocusing RF-pulse duration to 8.9 ms. These RF-pulse durations resulted in an excitation slice-select gradient of 22.6 mT/m and a refocusing gradient of 4.6 mT/m for a slice thickness of 1.5 mm. The nominal bandwidth-time product of the RF-pulses used for all the sequences was 2.6. The spin-echo occurred at $TE_{SE} = 25$ ms and the EPI k-space centre was acquired after 44 ms, resulting in an effective echo time TE_{eff} for phase evolution of $TE_{eff} = 19$ ms. Four slices were acquired in total, one axial and one

[11] For this reason regions with an SNR of below 5 were masked out, and excluded from further evaluation.

coronal slice positioned at the tip of each of the temperature probes. Regions of interest (ROI) with 19 to 22 voxel were defined around the sensor tips. For each slice, the DMSO image was acquired 2 seconds after the water image at the exact same position. The other imaging parameters were TR = 4 s, bandwidth (bw) = 752 Hz/Px, resolution 128×128, voxel size 1.5×1.5×1.5 mm^3, GRAPPA factor 4.

Results

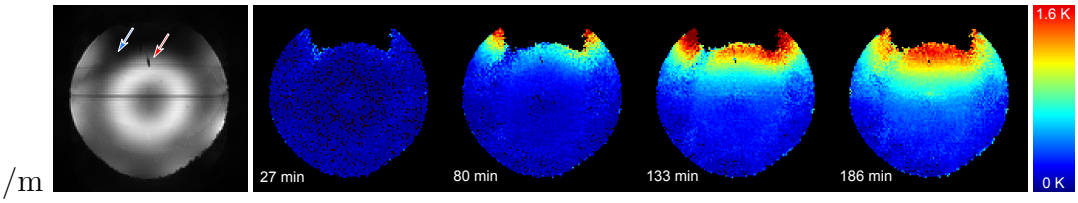

Figure 5.7: *An axial water magnitude image and successive temperature maps (acquisition times below each figure). The heating coil was placed on top of the phantom, causing some RF-shadowing, which was masked out in the temperature maps. The blue arrow points at a low SNR area in the DMSO images, which lead to possibly erroneous temperature estimates in this area. The red arrow points to the tip of temperature sensor 1 (the signal void, since the sensor displaces water). The two horizontal saturation bands through sensor 1 and the centre of the phantom are due to the acquisition of two orthogonal coronal slices. The displayed temperature maps were acquired during RF-heating with the exception of the last image.*

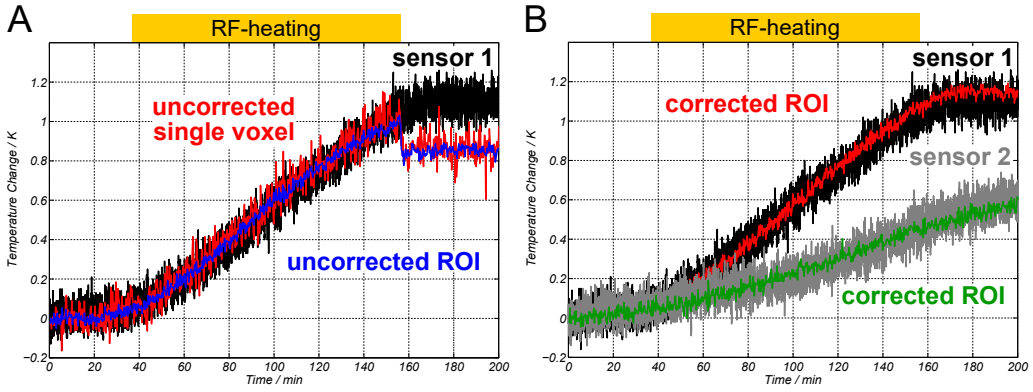

Figure 5.8: *(A) Sensor 1 unsmoothed time course (black) with a temporal resolution of 1 second. On top a single voxel uncorrected time course (red) and the uncorrected time course of the ROI (blue) in the axial slice surrounding sensor 1. (B) Corrected time courses of ROIs around sensor 1 (red) and sensor 2 (green). The plotted ROI around sensor 2 was in the coronal slice.*

RF-heating with the 125 MHz coil for 2 hours increased the temperature of the water/DMSO phantom by approximately 1.8 K close to the heating coil, and below 0.1 K on the opposite side of the phantom. Figure 5.7 shows an axial water magnitude image of the phantom and four MR temperature maps during heating.

The temperature increases at the sites of the sensors were (1.1 ± 0.1) K (sensor 1) and (0.6 ± 0.1) K (sensor 2). The time courses of the uncorrected temperature change in voxels surrounding the temperature sensors follow the sensor time courses closely, until shortly after the heating coil was turned off. A sudden step in all of the uncorrected temperature change time courses caused a deviation of the sensor and uncorrected temperature change time courses by approximately 0.2 K. After correction of the water temperature change time course with the smoothed DMSO time courses, the single voxel time courses surrounding the temperature sensor followed the sensor's time course throughout the experiment. Physically plausible time courses were measured for all the other voxels in the phantom. Both ROIs in the axial and coronal slice close to fibre optic sensor 1 yield a corrected temperature increase of (1.2 ± 0.1) K (sensor 1: (1.1 ± 0.1) K). The ROIs around fibre optic sensor 2 measured an increase of (0.6 ± 0.1) K (exactly as the temperature measured by sensor 2). The standard deviation across the approximately 20-voxel ROIs was 0.09 K. The standard deviation of the difference between the sensor and the MR temperature measurement (ROI) was 0.05 K with the largest deviation being 0.2 K. The flip angle at sensor 1 was approximately 100° and 70° at sensor 2. This results in a possible overestimation of the temperature by 1.3 % and 0.4 % or 0.014 K and 0.003 K for the ROIs around sensor 1 and sensor 2, respectively, due to the phase-altering effect of the SE sequences. This effect is further discussed in Section 5.2.4.

Frequency-selectivity of the Ivanov method was tested using the SE sequence as described above (Section 5.2.1) without the EPI readout, $TE_{eff} = 0$ and a spherical water phantom[12] with an enclosed spherical DMSO phantom inside.[13] Two separate water and DMSO images were acquired by setting the scanner frequency to water and DMSO, respectively. Figure 5.9 shows the magnitude images of the phantom with physicaly separate DMSO and water compartments. The Ivanov technique shows excellent suppression of either the water signal or the DMSO signal, depending on the resonance frequency used.

5.2.2 RF-heating without Heating Coil Experiment

Set-up

The same spherical phantom (diameter 15 cm) as in the RF-coil heating experiment (Section 5.2.1), containing a homogeneous mixture of 1 % agar, 1 % NaCl, 34 % DMSO and 64 % water was used for the measurement. Imaging was performed using the modified ASE gradient reversal technique shown in Figure 5.1A (Park et al., 1987; Volk et al., 1987). The phantom heating MR sequence was altered to run 10 TRs of normal SE imaging scans followed by 20 repetitions of pure RF heating

[12]Water phantom composition: 98 % water, 1 % agar and 1 % NaCl.

[13]The pure DMSO was enclosed in a plastic sphere. No gelling agent was needed due to the high viscosity of DMSO at room temperature.

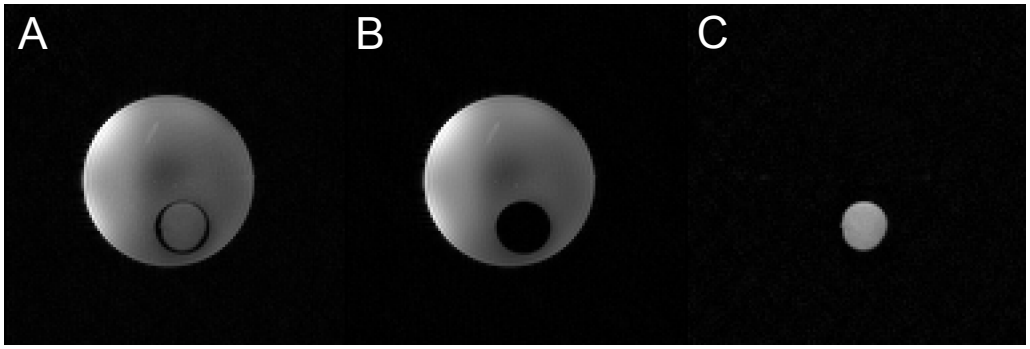

Figure 5.9: *Phantom with separate water and DMSO compartments imaged using the SE Ivanov method. (A) Water and DMSO image combined. (B) Ivanov technique SE image with the frequency set to the water resonance frequency and suppressing DMSO. (C) Frequency is set to the DMSO resonance frequency, suppressing water. The unwanted species is reliably suppressed with the signal magnitude at noise level.*

pulses, i.e. switching off the image acquisition. This way the sequence delivered an average power of 23 W to the coil. To achieve good separation of the water and DMSO proton signal using the standard vendor-provided RF pulses, the duration of the excitation and refocusing RF pulses was set to 4 ms. These RF pulse durations resulted in an excitation slice-select gradient of -10 mT/m and a refocusing gradient of 10 mT/m for a slice thickness of 1.5 mm.[14] The spin-echo occurred at $TE_{SE} = 21$ ms and the EPI k-space centre was acquired after 40 ms, resulting in an effective echo time TE_{eff} for phase evolution of $TE_{eff} = 19$ ms (also see Figure 5.1). The other imaging parameters were TR = 4 s, bandwidth (bw) = 752 Hz/Px, resolution 128×128, nominal voxel size 1.5×1.5×1.5 mm^3, GRAPPA factor 4, total acquisition time 133 min. In addition, the temperature in the phantom was monitored at two locations (sensor 1 approximately 2.5 cm below the centre of the phantom and sensor 2 approximately 3 cm to the right of the centre) with fluoroptic temperature sensors (Luxtron Lumasense, USA). Three axial slices were acquired. Two were positioned at the tip of each of the temperature probes. Regions of interest (ROI) with 28 and 11 voxel were defined around the sensor tips. For each slice, the DMSO image was acquired 2 seconds after the water image at the exact same position.

Results

The 2 hour high SAR sequence increased the temperature of the water/DMSO phantom by approximately 6 K in the centre and 3 K at the edge. Figure 5.11A shows a time-series for the axial slice through sensor 1. The uncorrected and corrected time courses of a representative voxel at sensor 1 and the sensor's time course are displayed. For the uncorrected time course there is a steady artifactual drift to higher temperature change values as compared with the temperature measurement of sensor 1. After correction of the water temperature change time course with

[14]The nominal bandwidth-time product of the RF pulses used for all the sequences was 2.6.

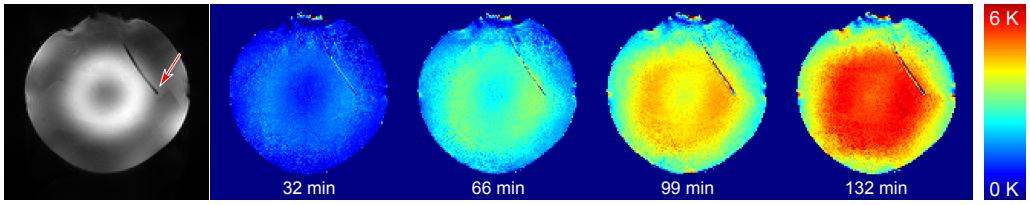

Figure 5.10: *High SAR sequence phantom heating experiment. An axial phantom water magnitude image and successive temperature maps (acquisition times below each figure). The red arrow points to the tip of temperature sensor 2 (the signal void). The sensor cable lies within the imaging slice for several centimetres resulting in MR temperature errors along its path. The displayed temperature maps were acquired interleaved to the RF heating pulses.*

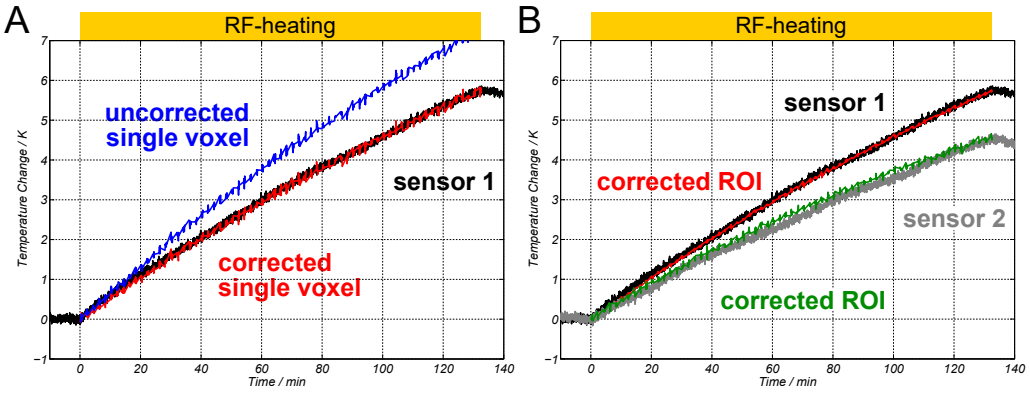

Figure 5.11: *High SAR sequence phantom heating experiment time courses. (A) Sensor 1 unsmoothed temperature time course (black) with a temporal resolution of 1 second. On top a single voxel uncorrected time course (blue) and the corrected time course (red) of a voxel close to sensor 1. (B) The corrected MR thermometry time courses of ROIs around sensor 1 (black) and sensor 2 (grey) are shown as red and green graphs, respectively.*

the smoothed DMSO time course, the single voxel time courses surrounding the temperature sensor followed the sensor's time course throughout the experiment. A similar drift of the MR temperature time course was also seen around sensor 2. After correction, physically plausible time courses were measured for all the voxels in the phantom. Figure 5.11B shows the corrected temperature time courses for ROIs around both sensors. The corrected MR measured temperature increase at the sites of the sensors was (5.7 ± 0.2) K (sensor 1) and (4.6 ± 0.2) K (sensor 2) compared to the temperature sensor reading of (5.7 ± 0.1) K (sensor 1) and (4.5 ± 0.1) K (sensor 2). Figure 5.10 shows an axial water magnitude image of the phantom and four MR temperature maps during heating at the position of sensor 2. The flip angle at sensor 1 was approximately 80° and 48° at sensor 2. This could lead to a possible underestimation of the temperature by 0.5 % and 0.1 % or 0.03 K and 0.005 K for the ROIs around sensor 1 and sensor 2, respectively. This possible underestimation is again due to the phase-altering effect of the SE sequences which is further discussed in Section 5.2.4.

5.2.3 In-vivo MR Thermometry

Set-up

One to six coronal water slices, and the same number of fat slices, were acquired across the occipital lobe in 5 healthy subjects. The separate water and fat images at the same position were acquired by alternately switching the RF-pulses to the water and fat frequency in immediate succession. The delay between the water and fat acquisition was only 50 ms. Most measurements were acquired with a TR of 2000 ms. To enable a frequency spectrum analysis of all the physiological fluctuation components, a time-series with a TR of 250 ms was acquired, covering only one position in space, which included both water and fat slices. It was found that the shortest excitation and refocusing RF-pulse duration for which the fat signal reached its maximum amplitude was approximately 4 ms (see the Paragraph below on page 114 on the frequency-selectivity of the fast GR approach). For this pulse duration, the fat was mostly left unsaturated by the water acquisition at the imaging position. To improve robustness to B_0 inhomogeneities, the RF-pulse durations were set to 6.4 ms, ensuring that the fat remained unsaturated even with B_0 inhomogeneities. For a pulse duration of 6.4 ms, the slice-select gradients, for the 1.5 mm thick slices acquired, were -6.4 mT/m and 6.4 mT/m for the excitation and refocusing gradients, respectively (Volk et al., 1987). The other imaging parameters were: TE_{SE} = 21 ms, k-space centred at 33.6 ms → effective echo time TE_{eff} = 12.6 ms, bw = 1502 Hz/Px, resolution 128×128, nominal voxel size 1.5×1.5×1.5 mm^3, GRAPPA factor 4, left-right phase encoding direction.

Results

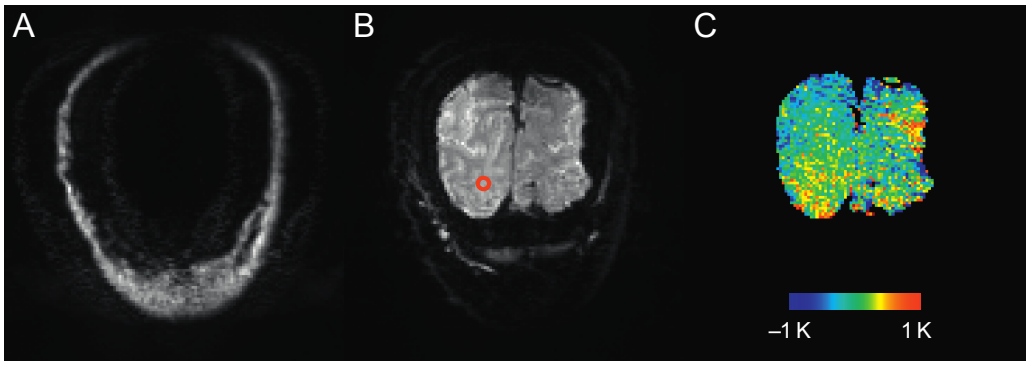

Figure 5.12: *In-vivo temperature stability measurement using the GR ASE technique (Fig. 5.1A) with RF pulse durations of 6.4 ms. (A) Fat and (B) water images of a representative slice with a TR of 2 s and (C) the unsmoothed referenced temperature change map for the last repetition after 10 min. The red circle in (B) marks the position of the nine voxel ROI used for Figure 5.13A and B. Due to the left–right phase encoding direction, distortions are seen in the left–right direction.*

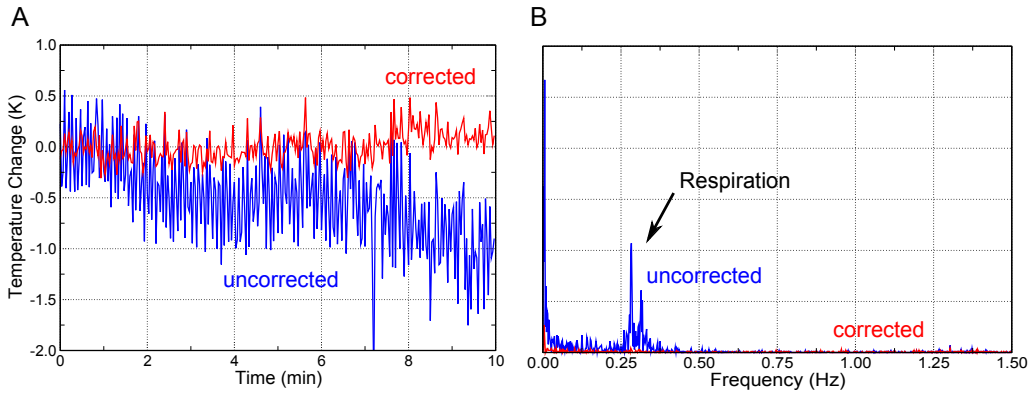

Figure 5.13: *(A) Observed corrected (red) and uncorrected (blue) temperature time courses of the nine voxel ROI depicted in Figure 5.12 with a TR of 2 s. The fluctuation amplitude is reduced, and the drift over time is corrected. (B) Power spectrum of the uncorrected (blue) and reference corrected (red) temperature time courses for the same ROI, but for a TR of 250 ms. Drift and low frequency fluctuations up to about 0.5 Hz are strongly and almost completely suppressed. Including respiration-induced field shifts at around 0.3 Hz. Higher order fluctuations are also generally lower with some frequency components suppressed at 1.3 Hz, probably due to heartbeat.*

Figure 5.12 shows the fat A and water B image of a representative coronal slice across the occipital lobe, with a TR of 2 seconds. The water and fat, respectively, are fully suppressed, despite some minor ghosting in the fat image A. Figure 5.12C is the referenced temperature change map after 10 minutes. Compared to the unreferenced average temperature change of (-1.1 ± 0.5) K, the corrected temperature map referenced by the fat images shows practically no temperature change (average (-0.1 ± 0.3) K), as expected (Collins et al., 2004a). The time course of a 9 voxel ROI in Figure 5.13A shows that not only the drift over time is corrected, but the contributions from higher frequency fluctuations are also reduced. This is more clearly shown in Figure 5.13B, which is a plot of the power spectrum for a corrected and uncorrected temperature time course. This was obtained for the same slice and ROI position, but from an acquisition with a TR of 250 ms.

The reduction of TR from 2000 ms to 250 ms leads to an average drop in SNR by a factor of 3 in the water image. The fat image SNR is only slightly reduced due to its shorter T_1 in comparison to water (Ren et al., 2008; Sprinkhuizen and Bakker, 2012). Even though the SNR of the water image dropped significantly, it is still apparent that several frequency components in the range from 0 to 0.5 Hz are substantially reduced, such as the large respiratory peaks around 0.3 Hz, and peaks between 1 and 1.5 Hz probably due to cardiac pulsation (Petridou et al., 2009). The extremely short TR of only 250 ms was used in order to demonstrate that the high frequency components (e.g. breathing) can be corrected. For higher precision longer values of TR are advisable.

In general, the fat correction improved the temperature measurements for all time-series, reducing fast fluctuations and long term drift. For the inferior part of

the brain the correction worked better, probably due to the larger amount of fat in close proximity to the brain. In the superior part of the most anterior slices, the fat correction did not always improve the temperature measurement, due to the low fat signal within the slice. This affected 5 out of a total of 72 slices. The single voxel standard deviation decreased from (0.5 ± 0.2) K, for the uncorrected time courses, to (0.3 ± 0.2) K for the fat corrected time courses for all the brain voxels measured. Long term drift across the whole brain was corrected from up to 1.2 K to (0.1 ± 0.2) K for all the measurements.

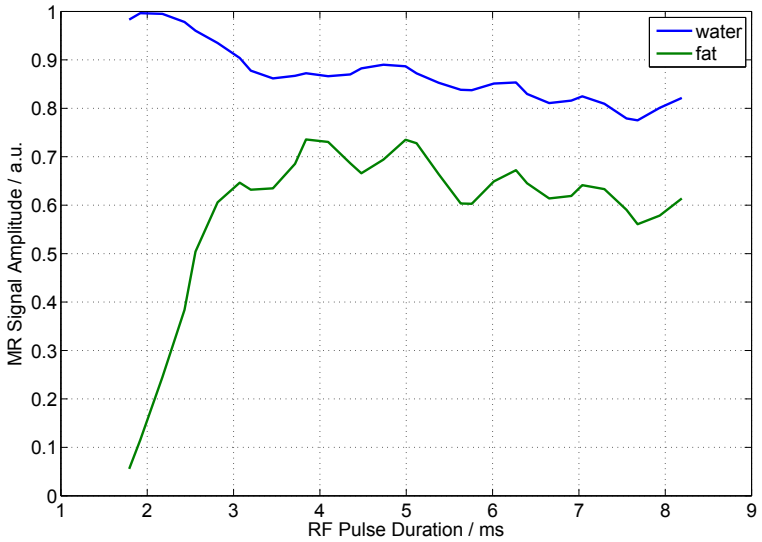

Figure 5.14: *Signal amplitudes of the GR SE technique for water and fat in immediate succession at the same position in space. The water signal amplitude slightly decreases as the RF pulse duration increases due to an necessary increase in echo time TE_{SE}, which was always kept minimal. As the RF pulse duration increases the fat slice at the position of the water slice becomes less and less saturated and inverted. Therefore the fat signal amplitude strongly increases until the whole slice is unsaturated. This occurs for an RF pulse duration of approximately 4 to 5 ms. For longer pulse durations the fat signal also slightly decreases due to the increasing echo time. The oscillations in the fat and in the water signal amplitude are probably due to constructive and destructive interactions of some remaining transverse magnetisation.*

To test and verify the prediction by theory (Section 5.1.1) and Bloch simulations (Section 5.2.4 and Figures 5.2 and 5.15) that the fat slice at the imaging position can be left unsaturated by the preceding water slice acquisition an additional experiment was done. A cylindrical phantom with a water and a fat (sunflower oil) phase was used. The excitation and refocusing RF pulse durations were equal, but varied in duration from 1792 μs to 8192 μs in 31 steps for the gradient reversal SE sequence described above and the minimal delay between the water and the fat acquisition. For each acquisition the minimal possible spin-echo echo time TE_{SE} was used and a

$TE_{eff} = 0$.[15] The other imaging parameters were set as above (Section 5.2.3 Set-up) with a repetition time TR = 2000 ms.

Figure 5.14 shows the MR signal amplitude of water and fat for varying RF pulse durations. The water slice was acquired first and immediately afterwards the fat slice. Plotted are the GR spin-echo MR signal magnitudes of water and fat for these two acquisitions.[16] The water spin-echo amplitude decreases with RF pulse duration since the echo time TE_{SE} also increases with RF pulse duration. The fat signal has maxima around 4 ms and 5 ms RF pulse duration, meaning that the fat slice acquisition was unaltered by the previous water slice acquisition. The fat signal also drops off for longer RF pulse durations due to the longer echo time. For the in-vivo GR experiment described before (Section 5.2.3) a RF pulse duration of 6.4 ms was chosen, due to the local maximum of the fat signal for this duration and to ensure that fat remained unsaturated even with B_0 inhomogeneities.

5.2.4 Bloch Simulation Results

Figure 5.15 shows the result of a single gradient reversal simulation for a -1000 Hz frequency offset with respect to the chemical species and an excitation flip angle of 90°. This simulates the case when the frequency is set to water and the effect on the fat is of interest, like in the case of the in-vivo experiment (Section 5.2.3). As desired there is no net transverse magnetisation at the time of the SE for the off-resonant species (e.g. fat), while the on-resonant species (e.g. water) would give the full signal at the centre position (in Figure 2.17). Changing the scanner frequency then by -1000 Hz makes the GR SE sequence frequency-selective to fat and an immediately afterwards acquired slice at position 0 mm would generate a high fat signal.

The simulation described was then done for a range of flip angles and offset frequencies. Figures 5.16 and 5.17 display the Bloch simulation results of the two frequency-selective SE techniques investigated in this work. The magnitude and phase of the transverse magnetisation is plotted at the time of the spin-echo. As expected, the signal magnitude has a maximum for an excitation flip angle of 90° (assuming a refocusing flip angle of twice the excitation flip angle) and drops off for higher and lower flip angle. Additionally, both the gradient reversal technique and the Ivanov technique cause the signal magnitude to decrease with offset frequency, and only the on-resonant species is imaged.

The bandwidths used for the in-vivo measurement and the phantom heating experiments in generating an effective transverse magnetisation were set to different values. For the in-vivo measurements the imaging bandwidth was made considerably narrower than the 1000 Hz frequency water/fat frequency difference, due to the additional constraint of leaving the fat slice unsaturated at the imaging position (see

[15] For the shortest RF pulses the resulting echo time was $TE_{SE} = 23$ ms.

[16] Only the signal amplitude of the unsuppressed species is plotted, since already for a RF pulse duration of 1.792 ms the excited and refocused slice of the unwanted species are displaced by more than 2 mm and therefore no signal generated.

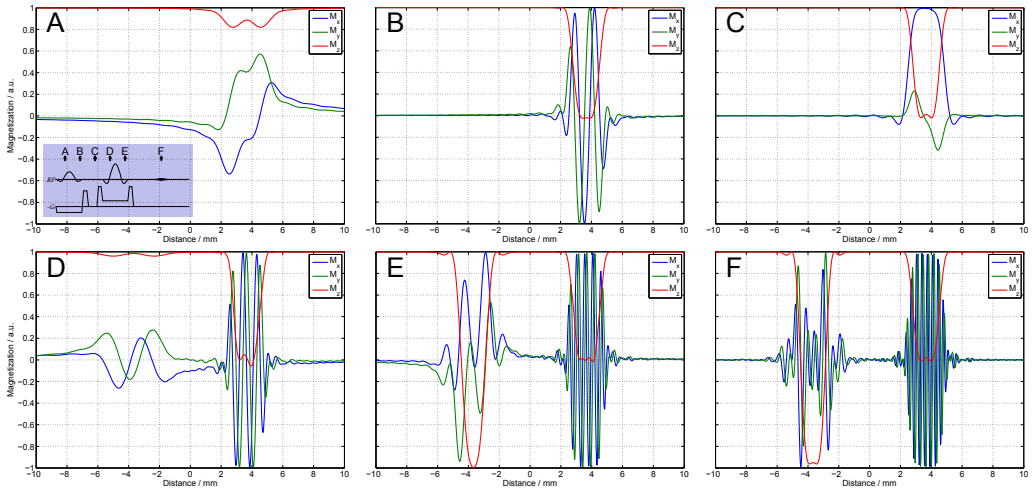

Figure 5.15: *Simulated -1000 Hz off-resonant GR SE slice excitation time series for the sequence parameters used in the in-vivo SE thermometry experiment (Section 5.2.3, nominal slice thickness 1.5 mm). Compare also with Figure 2.17 and Figure 5.2. The times of the separate images are displayed in the blue box in (A). Displayed is the x-, y-, z-magnetisation along the direction of the slice select gradient in blue, green and red, respectively (as always z is along the B_0 direction and x and y are in the transverse plane). The simulation starts in equilibrium, when all the magnetisation is in the z-direction. (B) The excitation RF-pulse is almost finished. Therefore the z-magnetisation is close to zero at the position of the slice. The slice position is shifted to the right due to the -1000 Hz frequency offset. The magnetisation in the transverse plane is dephased. (C) The dephased transverse magnetisation is rephased by the gradient following the excitation RF-pulse and almost completely oriented in the positive x-direction. The phase of the transverse magnetisation is slightly different than for the on-resonant excitation, visible on M_y which is not symmetric to the horizontal axis (cf. Fig. 2.17 C). (D) The crusher gradient before the refocusing pulse dephased the transverse magnetisation and the RF-pulse just started to manipulate the magnetisation at a position now shifted to the left due to the frequency offset and the opposite gradient polarity. (E) Almost at the end of the refocusing pulse. (F) After the crusher gradients, there is practically no coherent transverse magnetisation, i.e. the transverse magnetisation is strongly dephased and therefore no signal is detectable. Between the position of the excitation slice and the position of the refocusing slice is enough unsaturated magnetisation ($M_z \approx 1$ and $M_x \approx M_y \approx 0$) for a high SNR slice-selective SE acquisition.*

Figure 5.15). The RF pulse durations were set to 6.4 ms, resulting in a frequency bandwidth of only about ±300 Hz (see Figure 5.16). In the phantom heating experiments (Section 5.2.1 and 5.2.2) complete suppression for the off-resonant species was achieved at 500 Hz and 550 Hz for the Gradient Reversal (pulse durations: $\tau_{1,2} = 4$ ms) and the Ivanov technique (pulse durations: $\tau_1 = 1.8$ ms, $\tau_2 = 8.9$ ms), respectively.[17] Both techniques are very similar with regard to suppression of the

[17]This broader imaging bandwidth was possible for the water/DMSO mixture, since the B_0 inhomogeneities in the spherical phantom were small.

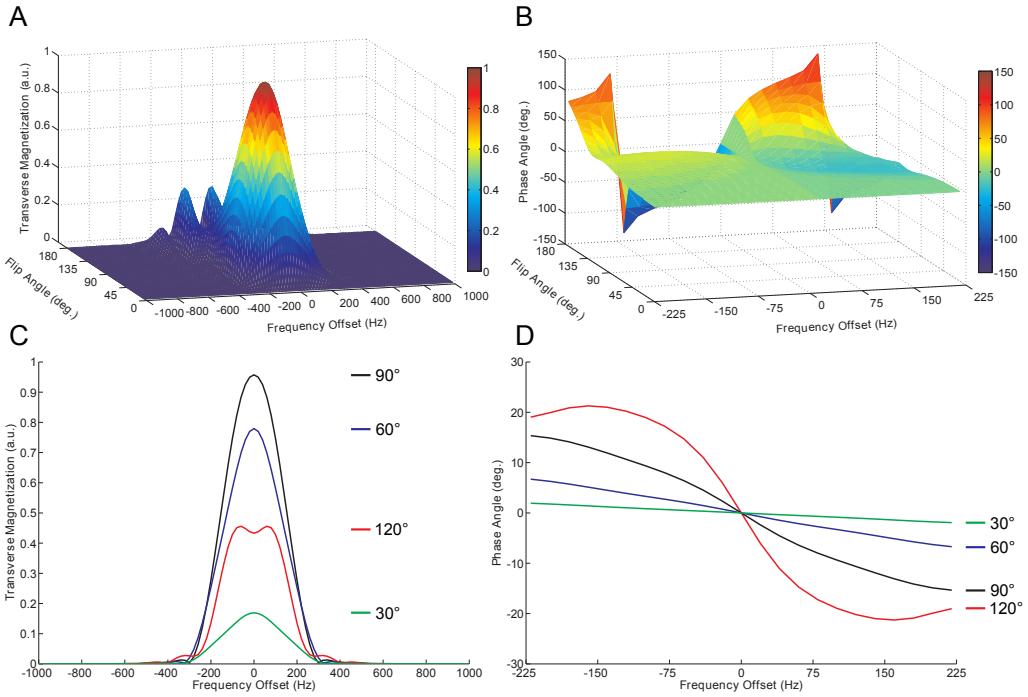

Figure 5.16: *Bloch simulation results for the gradient reversal technique used in-vivo, with an equal excitation and refocusing pulse duration of 6.4 ms. (A) The magnitude of the spin-echo as a function of frequency offset (x-axis) and excitation flip angle (y-axis), with a refocusing flip angle twice as large as the excitation flip angle. For excitation flip angle below 135°, all signal below -400 Hz offset and above 400 Hz offset is completely suppressed. (B) For higher flip angle, the spin-echo signal is also suppressed, but the phase of the spin-echo is varying more strongly. See Table 5.1 for quantitative numbers on the gradient reversal spin-echo phase inhomogeneity. (C) The magnitude of the spin-echo as a function of frequency offset (x-axis) for selected excitation flip angle. The signal outside of the imaging band is clearly suppressed. (D) The phase of the spin-echo for the selected excitation flip angle (as in C). As the flip angle increases the spin-echo phase varies more strongly, resulting in a potentially larger MR temperature bias.*

species outside the imaging bandwidth.[18] The simulation showed a net transverse magnetisation outside the imaging bandwidth of well below 1 % of the achievable maximum. As regards suppression of unwanted magnetisation, both frequency-selective SE techniques are insensitive to B_1 inhomogeneities. For all simulated excitation flip angle ranging from 5° to 180°. The off-resonant species was below 0.1 % of the maximal achieved signal for the on-resonant species.

Unfortunately, the applicability of this wide B_1 range is reduced because of an unwanted sequence-induced phase shift, which can be seen in Figure 5.16B and D and Figure 5.17. Ideally and normally expected, the phase of the spin-echo should be constant, in particular independent of flip angle and frequency offset. However it

[18]The imaging or frequency-selective bandwidth is only determined by the bandwidth-time product of the pulses and the $\Delta\tau = \tau_2 \pm \tau_1$, '+' for the GR and '-' for the IV technique.

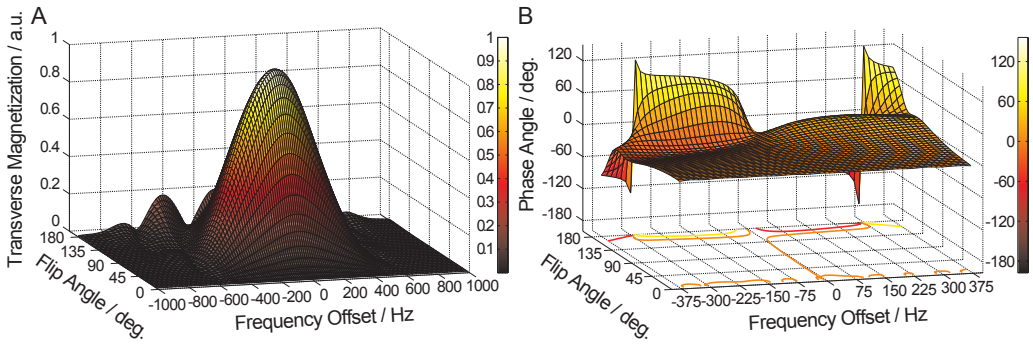

Figure 5.17: *Bloch simulation results for the SE technique by Ivanov. The excitation duration is set to 1.8 ms and the refocusing RF-pulse duration to 8.9 ms. (A) The magnitude of the spin-echo as a function of frequency offset (x-axis) and excitation flip angle (y-axis), with a refocusing flip angle twice as large as the excitation flip angle. For excitation flip angle below 135°, all signal below -500 Hz offset and above 500 Hz is completely suppressed. (B) For higher flip angle, the spin-echo signal is also suppressed, but the phase of the spin-echo is varying more strongly. See Table 5.2 for quantitative numbers on the Ivanov method spin-echo phase inhomogeneity.*

is obvious that the phase of the magnetisation depends on flip angle and frequency offset across the imaging band. Since the temperature change is determined by a frequency change, this frequency-dependent MR phase shift can lead to a systematic error in the measured temperature change. This error depends on the rate of change of the spin-echo MR phase with frequency offset. The slope of the spin-echo phase versus frequency change increases and becomes more inhomogeneous with increasing flip angle.

A summary of some sequence-induced gradient reversal spin-echo phase change values for the in-vivo and phantom measurement is shown in Table 5.1 with an average and a worst-case-error estimate. A summary of SE sequence induced phase change of the Ivanov technique used in the RF-coil phantom heating experiment is shown in Table 5.2. Here, the in-vivo measurement shows a larger sequence-induced spin-echo phase shift with frequency, and therefore a larger temperature bias. This is due to the smaller imaging bandwidth and shorter TE_{eff} with an average temperature bias of -1.8 % at a 90° excitation flip angle and respectively for the GR phantom measurement of -0.9 %. The temperature bias of the Ivanov technique at an flip angle of 90° is 0.7 %. In general, the non-constant spin-echo phase results in an overestimation of the temperature change for the Ivanov technique, while for the gradient reversal technique an underestimation occurs.

5.3 Discussion

Two frequency selective SE imaging techniques, the gradient reversal technique and the Ivanov technique, were applied to referenced MR phase thermometry (Ivanov et al., 2010; Park et al., 1987; Volk et al., 1987). The disadvantage of the lower signal

		GR Phantom measurement TE_{eff} = 19 ms, τ = 4 ms				GR In-vivo measurement TE_{eff} = 12.6 ms, τ = 6.4 ms			
		average		peak		average		peak	
		$\Delta\varphi_{SE}/\Delta f$ (°/Hz)	Error (%)	$\Delta\varphi_{SE}/\Delta f$ (°/Hz)	Error (%)	$\Delta\varphi_{SE}/\Delta f$ (°/Hz)	Error (%)	$\Delta\varphi_{SE}/\Delta f$ (°/Hz)	Error (%)
Excitation Flip Angle	45°	-0.01	-0.2	-0.01	-0.2	-0.02	-0.4	-0.02	-0.4
	60°	-0.02	-0.3	-0.02	-0.4	-0.03	-0.7	-0.04	-0.8
	90°	-0.06	-0.9	-0.08	-1.1	-0.08	-1.8	-0.12	-2.6
	120°	-0.12	-1.7	-0.2	-2.9	-0.13	-2.8	-0.30	-6.7
	135°	-0.09	-1.4	-0.16	-2.3	-0.10	-2.2	-0.27	-6.0

Table 5.1: *The change of the gradient reversal spin-echo sequence MR phase with frequency $\Delta\varphi_{SE}/\Delta f$ was determined by Bloch simulations for the actual scanning parameters. See Figures 5.16B and D for the simulation of the in-vivo GR sequence. The 'average' spin-echo phase slope was determined across the imaging band, with the 'peak' value being the strongest change in spin-echo phase versus frequency across the imaging band. Using the spin-echo phase slope and the effective echo time TE_{eff} the relative temperature error was calculated. The simulation results are for the phantom measurement with RF-pulse durations of τ = 4 ms and TE_{eff} = 19 ms. The simulation for the in-vivo measurement was done with RF-pulse durations of τ = 6.4 ms and TE_{eff} = 12.6 ms. For the phantom RF heating experiment, the shorter pulses (larger imaging bandwidth) reduce the error by ≈ 30 % and the longer TE_{eff} by another 34 %. The gradient reversal technique underestimates the temperature change.*

		IV Phantom measurement TE_{eff} = 19 ms, τ_1 = 1.8 ms, τ_2 = 8.9 ms			
		average		peak	
		$\Delta\varphi_{SE}/\Delta f$ (°/Hz)	Error (%)	$\Delta\varphi_{SE}/\Delta f$ (°/Hz)	Error (%)
Excitation Flip Angle	45°	0.01	0.1	0.01	0.2
	60°	0.02	0.2	0.02	0.3
	90°	0.05	0.7	0.06	0.9
	120°	0.09	1.3	0.18	2.6
	135°	0.10	1.5	0.27	3.9

Table 5.2: *The change of the Ivanov method spin-echo sequence MR phase with frequency $\Delta\varphi_{SE}/\Delta f$ was determined by Bloch simulations for the actual scanning parameters (see Figures 5.17). The 'average' spin-echo phase slope was determined across the imaging band, with the 'peak' value being the strongest change in spin-echo phase versus frequency across the imaging band. See also Table 5.1 for a comparison with the MR phase biases of the gradient reversal technique. The Ivanov technique results in an overestimation of the temperature change.*

magnitude of the spin-echo in comparison to a gradient echo with similar effective echo time TE_{eff} is partially compensated by the shift of the EPI readout with respect to the spin-echo which allows shorter TE_{SE} than for a normal SE sequence. It was shown using experiments (Section 5.2) and simulations (Section 5.2.4) that for both

methods the frequency selectivity is high and only a selected frequency band is imaged. The remaining magnetisation outside the imaging bandwidth is well below the noise level and does not contribute to image formation (Fig. 5.9, Fig. 5.16A and C, Fig. 5.17).

5.3.1 Spin-Echo Phase

Simulations (Section 5.2.4) revealed that the MR phase of the spin-echo is not constant, but varies with flip angle and more importantly with frequency. This is problematic, since the MR phase change accumulated during the time between the spin-echo and the centre of the readout (the effective echo time TE_{eff}) is used to estimate the temperature change. This additional variable small phase shift, induced by the sequence itself, can bias the temperature estimates. The phase offset varies with flip angle, resonance frequency, RF pulse shape and gradient amplitude.[19] The Ivanov technique generally slightly overestimates the temperature change, while the gradient reversal technique generally underestimates the temperature change, due to the typically positive or negative slope of the spin-echo phase with frequency and increased flip angle.

The introduced relative temperature error scales inversely with the effective echo time TE_{eff}, so that no universal rule can be given regarding the maximal flip angle consistent with acceptable temperature error. The phantom studies used a TE_{eff} of 19 ms, which made them rather less sensitive to this sequence-induced phase shift than the in-vivo study, which used a TE_{eff} = 12.6 ms (see Tables 5.1 and 5.2). In the discussed measurements, with flip angles below 100°, the error is estimated to be less than 1.1 % for the Ivanov technique (heating coil measurement) and -2.2 % for the gradient reversal technique using RF pulse durations of 6.4 ms (in-vivo measurement) and less than -0.9 % using RF pulse durations of 4 ms (high SAR heating measurement).[20] The temperature change of 1.8 K and 6 K in the phantom RF-heating experiments were too low for the temperature error to have a measurable effect. Further increasing the effective echo time would decrease the relative bias. Possible solutions to eliminate the error completely would be to acquire images with two different effective echo times, or to acquire B_0 and B_1 maps and correct the sequence-induced phase shift with the spin-echo phase shift simulation, depending on B_0 and B_1 at each point (Shmatukha et al., 2007). A third possibility is, to invert the slice-select gradient polarity every second image acquisition and fit a smooth curve to the measured temperature. For reference substance and water mixtures, it is important to note that B_0 changes affect the water and reference substance spin-echo phase equally, since they are at the same point in the spin-echo phase plane (Figures 5.16B and D and 5.17B) and therefore do not cause a bias.

[19] Especially the rephasing gradient of the RF excitation pulse.

[20] This error estimates are based on the sequence parameters used here.

5.3.2 Referenced Asymmetric SE MR Thermometry

The phantom heating experiments had a referenced MR temperature single voxel standard deviation of approximately 0.1 K. The referenced MR thermometry technique was able to reliably correct a sudden jump in phase which occurred when the external 125 MHz amplifier was turned off (Section 5.2.1) and a steady phase drift over time (Section 5.2.2). Using DMSO as a reference substance proved to be a good alternative to fat emulsions although the relative temperature coefficient of water with respect to DMSO is slightly dependent on concentration. For the small DMSO concentration range that was measured in the NMR spectrometer, the relative temperature coefficient was linearly dependent on concentration. If other concentrations are of interest, the relative temperature coefficient can easily be determined by a calibration measurement. The advantages of using DMSO as a reference substance are the miscibility with water, single ^{1}H frequency peak, high proton density and low toxicity. The miscibility with water resulted in considerably longer T_2 and T_2^* times of water and DMSO than for a water/fat emulsion.

The temperature stability measurements obtained in-vivo (Section 5.2.3) demonstrated that it is helpful to minimize the time for image acquisition and the time interval between water and reference substance acquisition. Using EPI and the gradient reversal SE technique, a water slice and a co-located fat slice can be acquired in less than 100 ms without loss in signal, enabling the correction of fast B_0 fluctuations, as caused by breathing and heartbeat (Fig. 5.13). Using the described method the correction is relatively straight forward and accurate. Reference-free approaches can in principle also correct for these fluctuations, if acquired fast enough and require regions of known temperature (Kuroda et al., 2006; Salomir et al., 2012). While reference-corrected MR thermometry methods work best on homogeneous mixtures of water and reference substances, the approach to fit the fat phase changes by a 2D linear function in space has been surprisingly successful. Higher order polynomials made the fit less stable and did not give better results. Still more elaborate fitting methods similar to the technique by Salomir et al. might further improve the fit (Salomir et al., 2012).

Both ASE MR thermometry techniques can in principle be applied to any part of the body. However, since both SE techniques are frequency-selective, they rely on good B_0 field homogeneity and on relative low B_0 fluctuations. For proper suppression and imaging these fluctuations should be below a quarter of the frequency difference of water and the reference substance (3.3 ppm for water-fat and 2 ppm for water-DMSO). Both ASE thermometry techniques are able to correct long term drifts. For field fluctuations on the order of seconds or less the gradient reversal technique is better suited, since here slice overlap of the wanted and unwanted chemical species can be more easily avoided (with RF pulse durations of 6.4 ms and slice-select gradient amplitudes of -6.4 mT/m and 6.4 mT/m for excitation and refocusing, respectively). To achieve this using the Ivanov technique and the same pulse type,

one of the RF pulses would have to be at least 13 ms long with a gradient amplitude of approximately 3 mT/m, which would further increase the acquisition time and make the slice-selection less reliable. Because of the desirability of short RF pulses, both methods are more easily applied at high field.[21] Going to even higher fields than 7 Tesla enables further shortening of the RF pulses and allows a shorter echo time, decreasing the delay between the water and fat acquisition and therefore leading to a better correction of fast field fluctuations. The approaches presented here could enable in-vivo SAR monitoring due to their high speed and, more importantly, considerably reduced sensitivity to physiologically related fluctuations (Oh et al., 2014). With no assumptions required regarding the temperature distribution in the tissue, these approaches can provide a single voxel standard deviation of 0.3 K.

5.3.3 Further Points to Discuss

Fat Spectrum

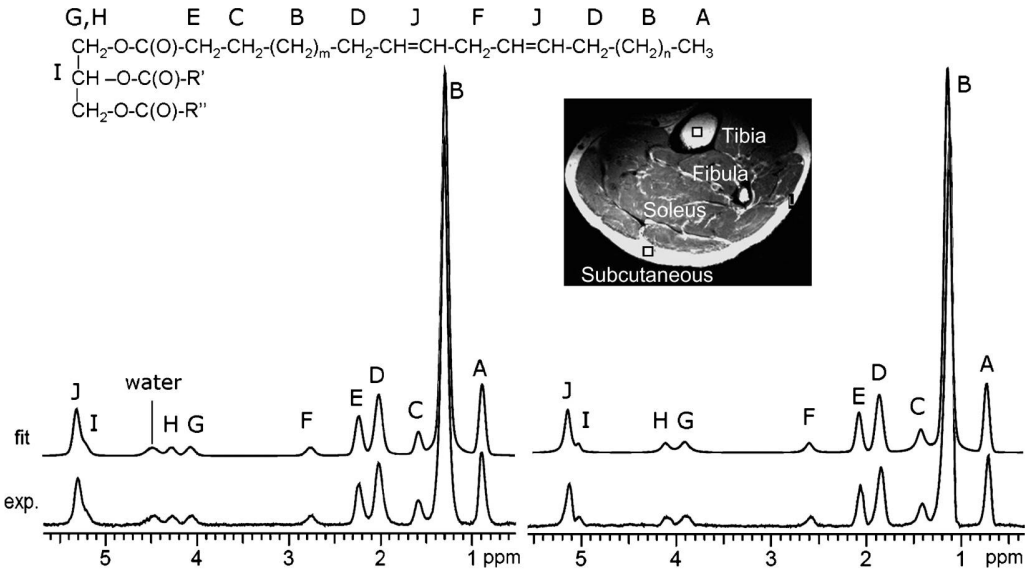

Figure 5.18: *^{1}H NMR spectra of subcutaneous fat (left) and tibial bone marrow (right) from a 26 year-old healthy male at 7 Tesla. Ten resonances can be resolved (A–J). The bottom trace shows the acquired spectrum, and the upper trace shows the fitted spectrum. A water signal is seen in the spectrum of subcutaneous fat but not bone marrow. A T_2-weighted image shows the position of the voxel in the subcutaneous fat tissue and tibial bone marrow (5 × 5 × 5 mm^3) from which the spectra were acquired (Ren et al., 2008). All peaks have T_2 times larger than 30 ms and are therefore visible in conventional MRI. Image of Ren et al. 2008.*

Since the proposed technique is frequency-selective a further point to discuss is

[21] Short RF pulses are desirable in the in-vivo case to shorten the time between water and fat reference acquisition. However, shorter pulses also have higher SAR which is normally not desirable (Ivanov et al., 2010).

	Chemical Group	Chemical Shift		Relative Signal Intensity in %	
		in ppm	rel. H_2O in Hz	Marrow	Subcutaneous
A	-CH3	0.90	1069	8.7	8.3
B	-(CH2)n-	1.30	950	62.4	62.7
C	-CH2-CH2-COO	1.59	864	7.0	7.2
D	-CH2-CH=CH-CH2-	2.03	734	9.5	9.6
E	-CH2-COO	2.25	668	6.7	6.6
F	=CH-CH2-CH=	2.77	514	1.6	1.5
J	-CH=CH-	5.31	-241	4.2	4.2

Table 5.3: *Saturation corrected relative signal amplitudes of the fat spectra (Ren et al., 2008). See also Figure 5.18.*

the fat NMR spectrum that includes multiple peaks.[22] A subcutaneous and a bone marrow fat spectrum is shown in Figure 5.18 and the relative signal amplitude of the different chemical groups is given in Table 5.3. The Figure and the Table data are taken from Ren et al., 2008. Most fat peaks are more than 2 ppm or 600 Hz shifted relative to the water peak (seen in Figure 5.18 on the left at 4.5 ppm). Therefore the GR SE sequence used in the in-vivo experiment would still be able to suppress these fat signals, since the imaging bandwith was ± 300 Hz. However, the peaks closer to water might get partially saturated by the water acquisition and therefore contribute a bit less to the fat signal. There is only the methine proton (-CH=CH-) peak that makes up 4 % of the spectrum that is only shifted by approximately -240 Hz relative to water. This peak can cause a small error in the MR water phase measurement (Rieke and Butts-Pauly, 2008a)

N/2 Ghosting Reference Line Acquisition

For every repetition right after the excitation pulse a 3-line reference scan is done. For the 3-line reference scan the central line of k-space is acquired three times in an EPI like manner. This is done in order to correct N/2 ghosting which is caused by slightly mismatched k-space lines for the different readout directions (see Section 2.2.3 on EPI and Schmitt et al., 1998). The N/2 ghosting correction then aligns the echoes of the different readout directions. This correction possibly alters the resulting phase of the reconstructed image and therefore the unreferenced MR temperature since the signal of the 3-line reference scan is a combination of the excited water and the simultaneously excited reference substance slice. Therefore, the N/2 ghosting

[22] Up to now it was assumed that the complete fat signal was shifted by 3.35 ppm relative to water (Ivanov et al., 2010).

correction might partially compensate the unreferenced MR temperature change.[23] However, since the 3-line reference scans of consecutive water and reference substance repetitions are very similar, this correction will affect the water and reference substance phase similarly and therefore the reference-corrected MR temperature is still correct.[24] For unreferenced MR thermometry this is a possible reason for temperature drift.

[23]The excitation RF pulse excites a water and a reference substance slice. Consequently, the 3-line reference scan signal is a combination of all the excited species. The described SE techniques are only frequency-selective after the refocusing RF-pulse.

[24]The 3-line reference scan is not exactly the same for the water and reference substance acquisition (even without a change in temperature and magnetic field) since the imaged and the later suppressed slice are not at the same position.

Chapter 6

Summary & Conclusion

There are obvious reasons for the push to higher fields in MRI. These include not just higher signal-to-noise ratio and MR phase sensitivity, but also higher contrast and specificity for contrasts like functional MRI and arterial spin labelling.[1] Proportional to the magnetic field increases the RF frequency used to manipulate the magnetisation. The deposition of RF energy in tissue increases more strongly with frequency and therefore the related risk of a dangerous increase in tissue temperature. The physics of complex tissue permittivity and its dependence on frequency leading to deposition of RF energy are explained in detail in Section 2.5. SAR safety limits are usually based on numerical electromagnetic simulations of a representative cohort of human models neglecting perfusion. Furthermore, multi-channel parallel transmit systems are capable of improving image homogeneity or even reducing SAR, however, further complicate the situation of power deposition (Graesslin et al., 2015). Only recently in-vivo measurements have been done that try to compare simulations with the temperature increase in the tissue (Oh et al., 2014; Simonis et al., 2017; Simonis et al., 2016).

The main purpose of this thesis was to develop improved methods for in-vivo temperature measurements and coil characterisation to utilise the full potential of MRI at 7 T and higher fields by ensuring RF safety. Besides that, MR thermometry is highly relevant to monitor thermal ablation, using, for example, focused ultrasound for ablation (Napoli et al., 2013). Phase-based MR thermometry is the most common method to measure relative temperature in aqueous tissue and was used in this work. However, phase-based MR thermometry is hampered by magnetic field drift, tissue movement, susceptibility variations and changes in tissue conductivity, i.e. anything that alters the measured MR phase. Current MR thermometry research mainly focuses on how to correct these influences.

The effect that surrounding air could have on MR thermometry was detected doing phantom heating experiments using hot air. Subtle differences between the actual

[1] In functional MRI (fMRI) signal contrast increases more than linear, in blood-oxygen-level dependent (BOLD) fMRI spatial specificity with respect to neural activity improves and arterial spin labelling techniques profit from a longer T_1 of blood (Gardener et al., 2009; Ivanov et al., 2017; Turner et al., 1993; Uludağ et al., 2009; Yacoub et al., 2003).

and measured MR temperatures were observed. This was the reason to study and explain this effect in detail in Chapter 4. It was shown that air susceptibility changes of surrounding air can alter the magnetic field inside the object and may easily affect the PRF MR thermometry results by several degrees if left uncorrected. This was demonstrated by magnetic field simulations and measurements of 10 different geometries and six different surrounding gas susceptibilities (Streicher et al., 2012).

One way of correcting phase altering effects in MR thermometry is by using a reference substance. In Section 5.1.2 an excellent means to do referenced MR thermometry in phantoms is presented. After some research and testing, dimethyl sulfoxide (DMSO) was chosen as a reference substance due to its low toxicity, miscibility with water, single proton peak and high proton density. The relative PRF shift of DMSO vs. water protons was determined. With this information and the microscopically homogeneous mixture of DMSO and water, practically all causes of error in PRF MR thermometry can be corrected. The relaxation times of the homogeneous mixture of DMSO and water at 7 Tesla are $T_2 = 82$ ms / 274 ms and $T_2^* = 75$ ms / 140 ms for water and DMSO, respectively. This is more than an order of magnitude higher than for water and fat mixtures, giving the opportunity to do highly accurate MR phase thermometry with no assumption of the underlying field disturbances.

The reference correction of MR phase is based on the premise that the DMSO and water signal can be imaged separately.[2]

The requirement of having a reliable separation of substances based on their resonance frequencies was met by a novel spin-echo MR thermometry technique. In experiments and extensive Bloch simulations, the spin-echo approach based on the gradient-reversal and Ivanov method was thoroughly tested and the results presented in Chapter 5 (Gomori et al., 1988; Ivanov et al., 2010; Park et al., 1987; Volk et al., 1987). It was found that the novel method reliably selects the on-resonant species and strongly suppresses the off-resonant species. The SE method is insensitive to B_1 inhomogeneities, but relies on a fairly good B_0 homogeneity, since only the desired frequency band is imaged. It was also found that the frequency-selective spin-echo technique slightly alters the MR phase when the frequency or the flip-angle changes. This dependence of SE MR phase on frequency may lead to a small systematic error in the temperature measurement. These errors were quantified, and possible correction schemes were provided (Sections 5.2.4 and 5.3.1).

One correction method is based on the knowledge of B_0 and B_1^+. An overview of several common B_1^+ mapping methods and an analysis of these, including Monte-Carlos simulations, is given in Chapter 3. On the basis of this evaluation, B_0 and B_1^+ mapping in this thesis work was done with an adaption of the actual flip angle imaging technique (Yarnykh, 2007). The B_1^+ dynamic range of the AFI sequence was almost doubled to 180° by incorporating the MR phase into the computation of

[2] A spectroscopic approach based on a multi-echo sequence in which the signals are algorithmically separated would also be sufficient.

the actual flip angle (Section 3.2). Otherwise flip angles above 90°-100° are folded in and give erroneous results, which can be hard to detect.[3] This extension of the dynamic range is especially useful at high field since B_1 inhomogeneity increases with frequency.

The novel SE technique was also employed for in-vivo fat-referenced MR thermometry. When the imaged frequency band is slightly narrower than required for water/fat selection and suppression this technique allows the acquisition of unsaturated water and fat images in rapid succession at the same position in space. The acquisition of a water and fat slice in less than 100 ms allows the correction of rapid field fluctuations in the brain, while still ensuring the correction of long term drift. Fast magnetic field fluctuations are, for example, caused by breathing and heartbeat. This is accomplished with no assumptions required regarding the temperature distribution in the tissue (Streicher et al., 2014).

Referenceless MR thermometry approaches with an EPI readout are in principle also capable of correcting fast field fluctuations, however, rely on some assumption of the temperature distribution. To the best of my knowledge, a similarly fast acquisition of water and reference substance MR images could only be done with spectral-spatial pulses.[4] Spectral-spatial pulses could allow even slightly faster imaging than the excitation and refocusing pulse of the SE allows. Although spectral-spatial pulses have been used in MR thermometry, there is no information given on its phase-altering behaviour with changes in frequency, as it is evaluated in this work for the SE approach (Grissom et al., 2009). Some preliminary simulations suggest similar challenges as for the SE technique presented here.

One experiment worth performing in the future would be to measure RF heating in-vivo in the human head. This could be realized by applying the presented SE thermometry method for 10 s with maximal SAR and then do 20 s of intermission with only some MR measurements. Each 10 s high SAR period would only cause a small heating of probably less than 0.01°C, which is more than an order of magnitude smaller than the accuracy reached with the referenced SE technique in-vivo. However, by running the 10 s heating, 20 s intermission sequence for one hour and applying the general linear model or multi-voxel pattern analysis, as in fMRI to it, it might be possible to detect temperature changes due to RF heating of the head (Friston et al., 1994). Moreover and most importantly, there would be no risk of harming the volunteer. As the MR thermometry methods improve, the number of averages could be reduced.

In conclusion, the work presented in this thesis will assist the development of a real-time in-vivo temperature monitoring system for ensuring patient RF safety at high field.

[3] This approach can also be applied to the double angle (Sec. 3.1) and the pre-saturation method (Sec. 3.3), again extending the dynamic range to 180°.

[4] This statement probably only holds for conventional MRI. New methods based on compressed sensing might accelerate the acquisition even more (Cao et al., 2015).

Bibliography

''2.3.6 Specific heat capacities''. In: *Tables of Physical & Chemical Constants*. 16th ed. Kaye & Laby Online, 2005.

''2.6.6 Magnetic properties of materials''. In: *Tables of Physical & Chemical Constants*. 16th ed. Kaye & Laby Online, 2005.

''3.9.2 Conductivities''. In: *Tables of Physical & Chemical Constants*. 16th ed. Kaye & Laby Online, 2005.

Ackerman JJH, DG Gadian, GK Radda, and GG Wong. ''Observation of 1H NMR signals with receiver coils tuned for other nuclides''. In: *Journal of Magnetic Resonance* 42.3 (1981), pp. 498–500.

Allard P and M Helgstrand. ''A method for simulation of NOESY, ROESY, and off-resonance ROESY spectra''. In: *Journal of Magnetic Resonance* 29.129 (1997), pp. 19–29.

Amadon A and N Boulant. ''Simultaneous measurement of B0- and B1-maps with modified Actual Flip Angle Imaging sequence''. In: *ISMRM*. Vol. 200. 2007. 2008, p. 1248.

Andersen A. ''On the Rician distribution of noisy MRI data''. In: *Magnetic resonance in medicine* 36 (1996), pp. 331–332.

Bakker H and J Skinner. ''Vibrational spectroscopy as a probe of structure and dynamics in liquid water Cited by me''. In: *Chemical reviews* (2009), pp. 1498–1517.

Balanis CA. *Advanced Engineering Electromagnetics*. John Wiley & Sons, 1989, p. 1008.

Bankson JA, RJ Stafford, and JD Hazle. ''Partially parallel imaging with phase-sensitive data: Increased temporal resolution for magnetic resonance temperature imaging.'' In: *Magnetic Resonance in Medicine* 53.3 (2005), pp. 658–65.

Baron P, R Deckers, M De Greef, LG Merckel, CJG Bakker, JG Bouwman, RLAW Bleys, MAAJ Van Den Bosch, and LW Bartels. ''Correction of proton resonance frequency shift MR-thermometry errors caused by heat-induced magnetic susceptibility changes during high intensity focused ultrasound ablations in tissues containing fat''. In: *Magnetic Resonance in Medicine* 72.6 (2014), pp. 1580–1589.

Baron P, M Ries, R Deckers, M de Greef, J Tanttu, K Max, MA Viergever, CTW Moonen, and LW Bartels. ''In Vivo T2-Based MR Thermometry in Adipose Tissue Layers for High-Intensity Focused Ultrasound Near-Field Monitoring''. In: *Magnetic Resonance in Medicine* 72 (2014), pp. 1057–1064.

Baron P, R Deckers, FM Knuttel, and LW Bartels. ''T1 and T2 temperature dependence of female human breast adipose tissue at 1.5 T: Groundwork for monitoring thermal therapies in the breast''. In: *NMR in Biomedicine* 28.11 (2015), pp. 1463–1470.

Belton PS, RR Jackson, and KJ Packer. ''Pulsed NMR Studies in striated muscle. I. Transverse nuclear spin relaxation times and freezing effects''. In: *Biochimica et Biophysica Acta* 286.1 (1972), pp. 16–25.

Bernstein MA, KF King, and XJ Zhou. *Handbook of MRI pulse sequences*. 2004, p. 1017.

Bernstein MA, M Grgic, TJ Brosnan, and NJ Pelc. ''Reconstructions of phase contrast, phased array multicoil data''. In: *Magnetic Resonance in Medicine* 32.3 (1994), pp. 330–4.

Birkl C, C Langkammer, J Haybaeck, C Ernst, R Stollberger, F Fazekas, and S Ropele. ''Temperature Dependency of T1 Relaxation Time in Unfixed and Fixed Human Brain Tissue''. In: *Biomed Tech* 58.Table 1 (2013), pp. 4–5.

Bley TA, O Wieben, CJ Francois, JH Brittain, and SB Reeder. ''Fat and water magnetic resonance imaging''. In: *Journal of Magnetic Resonance Imaging* 31.1 (2010), pp. 4–18.

Bloch F. ''Nuclear induction''. In: *Physical review* 70.7-8 (1946), pp. 460–474.

Bloch F and A Siegert. ''Magnetic resonance for nonrotating fields''. In: *Physical Review* 57 (1940), pp. 522–527.

Bloch F, WW Hansen, and M Packard. ''The Nuclear Induction Experiment''. In: *Physical Review* 70.7-8 (1946), pp. 474–485.

Bloembergen N, EM Purcell, and RV Pound. ''Relaxation Effects in Nuclear Magnetic Resonance Absorption''. In: *Physical Review* 73.7 (1948), p. 679.

Borman PTS, C Bos, T de Boorder, BW Raaymakers, CTW Moonen, and SPM Crijns. ''Towards real-time thermometry using simultaneous multislice MRI''. In: *Physics in Medicine and Biology* 61.17 (2016), N461–N477.

Bottomley PA and ER Andrew. ''RF magnetic field penetration, phase shift and power dissipation in biological tissue: implications for NMR imaging''. In: *Physics in medicine and biology* 23.4 (1978), pp. 630–43.

Bottomley PA, TH Foster, RE Argersinger, and LM Pfeifer. ''A review of normal tissue hydrogen NMR relaxation times and relaxation mechanisms from 1–100 MHz: dependence on tissue type, NMR frequency, temperature, species, excision, and age''. In: *Medical Physics* 11.4 (1984), p. 425.

Bottomley PA, RW Redington, WA Edelstein, and JF Schenck. ''Estimating radiofrequency power deposition in body NMR imaging''. In: *Magnetic Resonance in Medicine* 2.4 (1985), pp. 336–49.

Boulant N, M Bottlaender, L Uhrig, E Giacomini, M Luong, A Amadon, A Massire, B Larrat, and A Vignaud. ''FID navigator-based MR thermometry method to monitor small temperature changes in the brain of ventilated animals''. In: *NMR in Biomedicine* 28.1 (2015), pp. 101–107.

Brown TR, BM Kincaid, and K Ugurbil. ''NMR chemical shift imaging in three dimensions.'' In: *Proceedings of the National Academy of Sciences of the United States of America* 79.11 (1982), pp. 3523–6.

Brunner DO and KP Pruessmann. ''B1(+) interferometry for the calibration of RF transmitter arrays.'' In: *Magnetic resonance in medicine* 61.6 (2009), pp. 1480–8.

Brunner DO, N De Zanche, J Fröhlich, J Paska, and KP Pruessmann. ''Travelling-wave nuclear magnetic resonance.'' In: *Nature* 457.7232 (2009), pp. 994–8.

Buchner R, GT Hefter, and PM May. ''Dielectric relaxation of aqueous NaCl solutions''. In: *The Journal of Physical Chemistry A* 103.1 (1999).

Budinger TF and MD Bird. ''MRI and MRS of the human brain at magnetic fields of 14T to 20T: Technical feasibility, safety, and neuroscience horizons''. In: *NeuroImage* In Press (2017).

Buxton RB. *Introduction to Functional Magnetic Resonance Imaging Principles and Techniques*. Vol. 2. Cambridge University Press, 2009.

Bydder GM and IR Young. ''MR imaging: clinical use of the inversion recovery sequence.'' In: *Journal of computer assisted tomography* 9.4 (1985), pp. 659–675.

Bydder GM, JM Pennock, RE Steiner, S Khenia, JA Payne, and IR Young. ''The short TI inversion recovery sequence-An approach to MR imaging of the abdomen''. In: *Magnetic Resonance Imaging* 3.3 (1985), pp. 251–254.

Cady EB, PC D'Souza, J Penrice, and A Lorek. ''The estimation of local brain temperature by in vivo 1H magnetic resonance spectroscopy''. In: *Magnetic Resonance in Medicine* 33.6 (1995), pp. 862–7.

Cao Z, X Yan, and WA Grissom. ''Array-compressed parallel transmit pulse design''. In: *Magnetic Resonance in Medicine* 76.4 (2016), pp. 1158–1169.

Cao Z, S Oh, R Otazo, CT Sica, MA Griswold, and CM Collins. ''Complex-Difference Constrained Compressed Sensing Reconstruction for Accelerated PRF Thermometry with Application to MRI Induced RF Heating''. In: *Magnetic Resonance in Medicine* 73.4 (2015), pp. 1420–1431.

Cavanagh J, WJ Fairbrother, AG Palmer, III, and NJ Skelton. *Protein NMR Spectroscopy: Principles and Practice*. Vol. 28. Academic Press, 1995, p. 587.

Chen CN, VJ Sank, SM Cohen, and DI Hoult. ‘‘The field dependence of NMR imaging. I. Laboratory assessment of signal-to-noise ratio and power deposition.’’ In: *Magnetic resonance in medicine* 3.5 (1986), pp. 722–9.

Chilla GS, CH Tan, C Xu, and CL Poh. ‘‘Diffusion weighted magnetic resonance imaging and its recent trend-a survey.’’ In: *Quantitative imaging in medicine and surgery* 5.3 (2015), pp. 407–22.

Chung S, D Kim, E Breton, and L Axel. ‘‘Rapid B1+ mapping using a preconditioning RF pulse with TurboFLASH readout.’’ In: *Magnetic Resonance in Medicine* 64.2 (2010), pp. 439–46.

Clarke RN, AP Gregory, D Cannell, M Patrick, S Wylie, I Youngs, and G Hill. *A Guide to characterisation of dielectric materials at RF and microwave frequencies.* 2003.

Cole KS. ‘‘Electric phase angle of cell membranes’’. In: *The Journal of General Physiology* (1932), pp. 641–649.

Cole KS and RH Cole. ‘‘Dispersion and Absorption in Dielectrics I. Alternating Current Characteristics’’. In: *The Journal of Chemical Physics* 9.4 (1941), p. 341.

Collins CM. ‘‘Radiofrequency Field Calculations for High Field MRI’’. In: *Ultra High Field Magnetic Resonance Imaging*. Springer US, 2006. Chap. 8, pp. 209–248.

Collins CM and MB Smith. ‘‘Signal-to-noise ratio and absorbed power as functions of main magnetic field strength, and definition of ”90°” RF pulse for the head in the birdcage coil.’’ In: *Magnetic resonance in medicine* 45.4 (2001), pp. 684–91.

Collins CM and Z Wang. ‘‘Calculation of radiofrequency electromagnetic fields and their effects in MRI of human subjects.’’ In: *Magnetic resonance in medicine* 65.5 (2011), pp. 1470–82.

Collins CM, MB Smith, and R Turner. ‘‘Model of local temperature changes in brain upon functional activation.’’ In: *Journal of applied physiology (Bethesda, Md. : 1985)* 97.6 (2004), pp. 2051–5.

Collins CM, W Liu, J Wang, R Gruetter, JT Vaughan, K Uğurbil, and MB Smith. ‘‘Temperature and SAR calculations for a human head within volume and surface coils at 64 and 300 MHz.’’ In: *Journal of Magnetic Resonance Imaging* 19.5 (2004), pp. 650–6.

Coman D, HK Trubel, RE Rycyna, and F Hyder. ‘‘Brain temperature and pH measured by (1)H chemical shift imaging of a thulium agent.’’ In: *NMR in biomedicine* 22.2 (2009), pp. 229–39.

Corbett RJ, aR Laptook, G Tollefsbol, and B Kim. ‘‘Validation of a noninvasive method to measure brain temperature in vivo using 1H NMR spectroscopy’’. In: *Journal of neurochemistry* 64.3 (1995), pp. 1224–30.

Crawley aP, ML Wood, and RM Henkelman. ‘‘Elimination of transverse coherences in FLASH MRI.’’ In: *Magnetic Resonance in Medicine* 8.3 (1988), pp. 248–60.

Cross PC, J Burnham, and PA Leighton. ‘‘The Raman Spectrum and Structure of Water’’. In: *Journal of the American Chemical Society* 59.6 (1937), pp. 1134–1147.

Cunningham CH, JM Pauly, and KS Nayak. ‘‘Saturated double-angle method for rapid B1+ mapping.’’ In: *Magnetic Resonance in Medicine* 55.6 (2006), pp. 1326–33.

Dadakova T, J Gellermann, O Voigt, JG Korvink, JM Pavlina, J Hennig, and M Bock. ‘‘Fast PRF-based MR thermometry using double-echo EPI: in vivo comparison in a clinical hyperthermia setting’’. In: *Magnetic Resonance Materials in Physics, Biology and Medicine* 28.4 (2014), pp. 305–314.

Davidson DW and RH Cole. ‘‘Dielectric Relaxation in Glycerol, Propylene Glycol, and n-Propanol’’. In: *The Journal of Chemical Physics* 19.12 (1951), p. 1484.

Davis RS. ‘‘Equation for the volume magnetic susceptibility of moist air’’. In: *Metrologia* 35 (1998), p. 49.

De Poorter J. ‘‘Noninvasive MRI thermometry with the proton resonance frequency method: study of susceptibility effects’’. In: *Magnetic resonance in medicine* 34 (1995), pp. 359–367.

De Poorter J, C De Wagter, Y De Deene, C Thomsen, F Stahlberg, and E Achten. ‘‘Noninvasive MRI thermometry with the proton resonance frequency (PRF) method: in vivo results in human muscle.’’ In: *Magnetic Resonance in Medicine* 33.1 (1995), pp. 74–81.

de Senneville BD, S Roujol, CTW Moonen, and M Ries. ‘‘Motion correction in MR thermometry of abdominal organs: a comparison of the referenceless vs. the multibaseline approach.’’ In: *Magnetic Resonance in Medicine* 64.5 (2010), pp. 1373–81.

Debye P. *Polar molecules*. The Chemical Catalog Company, inc., 1929.

Del Grande F, F Santini, DA Herzka, MR Aro, CW Dean, GE Gold, and JA Carrino. ‘‘Fat-Suppression Techniques for 3-T MR Imaging of the Musculoskeletal System’’. EN. In: *Radiographics* 34.1 (2014), pp. 217–233.

Dhital B, C Labadie, F Stallmach, HE Möller, and R Turner. ‘‘Temperature dependence of water diffusion pools in brain white matter’’. In: *NeuroImage* 127 (2015), pp. 135–143.

Dixon WT. ‘‘Simple Proton Spectroscopic lmaging’’. In: *Radiology* 153.1 (1984), pp. 189–194.

Ernst R and W Anderson. ‘‘Application of Fourier Transform Spectroscopy to Magnetic Resonance’’. In: *The Review of Scientific Instruments* 37.1 (1966), p. 93.

Fautz HP, MW Vogel, P Gross, AB Kerr, and Y Zhu. ‘‘B1 mapping of coil arrays for parallel transmission’’. In: *ISMRM*. Vol. 16. 1. 2008, p. 1247.

Fautz HP, R Gumbrecht, P Gross, and F Schmitt. ''Extending the sensitivity range for transmit array B1 mapping using relative B1 maps''. In: *ISMRM*. Vol. 1422. 2008. 2012, p. 6307.

Feynman RP, FL Vernon, and RW Hellwarth. ''Geometrical Representation of the Schrodinger Equation for Solving Maser Problems''. In: *Journal of Applied Physics* 28.1 (1957), pp. 49–52.

Fiedler TM, ME Ladd, and AK Bitz. ''SAR Simulations & Safety''. In: *NeuroImage* (2017).

Foerster BU, D Tomasi, and EC Caparelli. ''Magnetic field shift due to mechanical vibration in functional magnetic resonance imaging.'' In: *Magnetic Resonance in Medicine* 54.5 (2005), pp. 1261–7.

Frahm J, A Haase, and D Matthaei. ''Rapid NMR imaging of dynamic processes using the FLASH technique.'' In: *Magnetic Resonance in Medicine* 3.2 (1986), pp. 321–7.

Frahm J, KD Merboldt, W Hanicke, and A Haase. ''Stimulated echo imaging''. In: *Journal of Magnetic Resonance* 64.1 (1985), pp. 81–93.

Friston KJ, P Jezzard, and R Turner. ''Analysis of Functional MRI Time-Series''. In: *Human Brain Mapping* 1.2 (1994), pp. 153–171.

Fujiwara S, Y Arata, H Ozawa, and M Kunugi. ''NMR Satellites as a Probe for Chemical Investigations''. In: *Pure and Applied Chemistry* 32.1-4 (1972), pp. 117–121.

Gabriel C, S Gabriel, and E Corthout. ''The dielectric properties of biological tissues: I. Literature survey.'' In: *Physics in medicine and biology* 41.11 (1996), pp. 2231–49.

Gabriel S, RW Lau, and C Gabriel. ''The dielectric properties of biological tissues: II. Measurements in the frequency range 10 Hz to 20 GHz''. In: *Physics in Medicine and Biology* 41.11 (1996), pp. 2251–2269.

Gabriel S, RW Lau, and C Gabriel. ''The dielectric properties of biological tissues: III. Parametric models for the dielectric spectrum of tissues.'' In: *Physics in medicine and biology* 41.11 (1996), p. 2251.

Gardener AG, PA Gowland, and ST Francis. ''Implementation of quantitative perfusion imaging using pulsed arterial spin labeling at ultra-high field.'' In: *Magnetic Resonance in Medicine* 61.4 (2009), pp. 874–82.

Gensler D, F Fidler, P Ehses, M Warmuth, T Reiter, M Düring, O Ritter, ME Ladd, HH Quick, PM Jakob, WR Bauer, and P Nordbeck. ''MR safety: Fast T1 thermometry of the RF-induced heating of medical devices''. In: *Magnetic Resonance in Medicine* 68.5 (2012), pp. 1593–1599.

Gerlach W and O Stern. ''Der experimentelle Nachweis der Richtungsquantelung im Magnetfeld''. In: *Zeitschrift für Physik* 9.1 (1922), pp. 349–352.

Gillies RJ, N Raghunand, ML García-Martín, and RA Gatenby. ''pH imaging: A review of pH measurement methods and applications in cancers''. In: *IEEE Engineering in Medicine and Biology Magazine* 23.5 (2004), pp. 57–64.

Gomori JM, GA Holland, RI Grossman, WB Gefter, and RE Lenkinski. ''Fat suppression by section-select gradient reversal on spin-echo MR imaging. Work in progress''. In: *Radiology* 168 (1988), pp. 493–495.

Graesslin I, P Vernickel, P Börnert, K Nehrke, G Mens, P Harvey, and U Katscher. ''Comprehensive RF safety concept for parallel transmission MR''. In: *Magnetic Resonance in Medicine* 74.1. Graesslin, I. et al. Comprehensive RF safety concept for parallel transmission MR. Magn. Reson. Med. 74, 589–598 (2015).2 (2015), pp. 589–598.

Gregory AP, RN Clarke, and MG Cox. ''Traceable measurement of dielectric reference liquids over the temperature interval 10–50 °C using coaxial-line methods''. In: *Measurement Science and Technology* 20.7 (2009), p. 075106.

Grissom WA, V Rieke, AB Holbrook, Y Medan, M Lustig, J Santos, MV McConnell, and K Butts-Pauly. ''Hybrid referenceless and multibaseline subtraction MR thermometry for monitoring thermal therapies in moving organs''. In: *Medical Physics* 37.9 (2010), p. 5014.

Grissom WA, AB Kerr, AB Holbrook, JM Pauly, and K Butts-Pauly. ''Maximum linear-phase spectral-spatial radiofrequency pulses for fat-suppressed proton resonance frequency-shift MR Thermometry''. In: *Magnetic Resonance in Medicine* 62.5 (2009), pp. 1242–50.

Grissom WA, M Lustig, AB Holbrook, V Rieke, JM Pauly, and K Butts-Pauly. ''Reweighted L1 referenceless PRF shift thermometry''. In: *Magnetic resonance in Med* 64.4 (2010), pp. 1068–77.

Griswold MA, PM Jakob, RM Heidemann, M Nittka, V Jellus, J Wang, B Kiefer, and A Haase. ''Generalized Autocalibrating Partially Parallel Acquisitions (GRAPPA)''. In: *Magnetic Resonance in Medicine* 47.6 (2002), pp. 1202–1210.

Gudbjartsson H and S Patz. ''The Rician distribution of noisy MRI data''. In: *Magnetic Resonance in Medicine* (1995), pp. 332–333.

Haacke EM, RW Brown, MR Thompson, and R Venkatesan. *Magnetic Resonance Imaging: Physical Principles and Sequence Design*. New York: John Wiley & Sons, 1999.

Haase A, J Frahm, W Hanicke, and D Matthaei. ''1H NMR chemical shift selective (CHESS) imaging''. In: *Physics in medicine and biology* 30.4 (1985), p. 341.

Haase A, J Frahm, D Matthaei, W Hänicke, and KD Merboldt. ''FLASH Imaging. Rapid NMR Imaging Using Low Flip-Angle Pulses''. In: *Journal of Magnetic Resonance* 67.2 (1986), pp. 258–266.

Hahn EL. ''Spin echoes''. In: *Physical Review* 80.4 (1950), p. 580.

Hall LD and SL Talagala. ''Mapping of pH and temperature distribution using chemical-shift-resolved tomography''. In: *Journal of Magnetic Resonance* 65.3 (1985), pp. 501–505.

Hanson LG. ''Is Quantum Mechanics Necessary for Understanding Magnetic Resonance?'' In: *Concepts in Magnetic Resonance Part A* 32A.5 (2008), pp. 329–340.

Harvey A and J Prausnitz. ''Dielectric constants of fluid mixtures over a wide range of temperature and density''. In: *Journal of solution chemistry* 16.10 (1987), pp. 857–869.

Hashim AI, X Zhang, JW Wojtkowiakk, and RJ Gillies. ''Imaging pH and Metastasis''. In: *NMR in Biomedicine* 24.6 (2011), pp. 582–591.

Hayt W and J Buck. *Engineering Electromagnetics*. McGraw-Hill Companies, 2011.

Hedlund LW, GP Cofer, SJ Owen, and G Allan Johnson. ''MR-compatible ventilator for small animals: computer-controlled ventilation for proton and noble gas imaging.'' In: *Magnetic resonance imaging* 18.6 (2000), pp. 753–9.

Helgstrand M, T Härd, and P Allard. ''Simulations of NMR pulse sequences during equilibrium and non-equilibrium chemical exchange.'' In: *Journal of biomolecular NMR* 18.1 (2000), pp. 49–63.

Hennig J. ''Echoes—how to generate, recognize, use or avoid them in MR-imaging sequences. Part I: Fundamental and not so fundamental properties of spin echoes''. In: *Concepts in Magnetic Resonance* 3.3 (1991), pp. 125–143.

Hindley J, WM Gedroyc, L Regan, E Stewart, C Tempany, K Hynnen, N Macdanold, Y Inbar, Y Itzchak, J Rabinovici, K Kim, Jf Geschwind, G Hesley, B Gostout, T Ehrenstein, S Hengst, M Sklair-levy, A Shushan, and F Jolesz. ''MRI Guidance of Focused Ultrasound Therapy of Uterine Fibroids: Early Results''. In: *American Journal of Roentgenology* 183.6 (2004), pp. 1713–9.

Hindman J. ''Proton resonance shift of water in the gas and liquid states''. In: *The Journal of Chemical Physics* 44.12 (1966), pp. 4582–4592.

Holz M, SR Heil, and A Sacco. ''Temperature-dependent self-diffusion coefficients of water and six selected molecular liquids for calibration in accurate 1H NMR PFG measurements''. In: *Physical Chemistry Chemical Physics* 2.20 (2000), pp. 4740–4742.

Holzhausen K. *Untersuchung der T1- , T2 – und T2* - Relaxation im Phantom und in-vivo*. 2011.

Homann H. *SAR Prediction and SAR Management for Parallel Transmit MRI*. KIT Scientific Publishing, 2011.

Hoult DI and B Bhakar. ''NMR Signal Reception: Virtual Photons and Coherent Spontaneous Emission''. In: *Concepts in Magnetic Resonance* 9.5 (1997), pp. 277–297.

Hoult DI and D Phil. ‘‘Sensitivity and power deposition in a high-field imaging experiment.’’ In: *Journal of Magnetic Resonance Imaging* 12.1 (2000), pp. 46–67.

Hoy AR and PR Bunker. ‘‘A Precise Solution of the Rotation Bending Schrödinger Equation for a Triatomic Molecule with Application to the Water Molecule’’. In: *Journal of Molecular Spectroscopy* 74.1 (1979), pp. 1–8.

Hynynen K, N McDannold, RV Mulkern, and FA Jolesz. ‘‘Temperature monitoring in fat with MRI’’. In: *Magnetic Resonance in Medicine* 43.6 (2000), pp. 901–904.

Insko E and L Bolinger. ‘‘Mapping of the radiofrequency field’’. In: *Journal of magnetic resonance. Series A* 103 (1993), pp. 82–85.

International Electrotechnical Commission. *Medical electrical equipment - Part 2-33: Particular requirements for the safety of magnetic resonance equipment for medical diagnosis*. 2008.

Ishihara Y, A Calderon, H Watanabe, K Okamoto, Y Suzuki, and K Kuroda. ‘‘A precise and fast temperature mapping using water proton chemical shift’’. In: *Magnetic resonance in medicine* 34.6 (1995), pp. 814–823.

Ivanov D, A Schäfer, MN Streicher, RM Heidemann, R Trampel, and R Turner. ‘‘A simple low-SAR technique for chemical-shift selection with high-field spin-echo imaging.’’ In: *Magnetic Resonance in Medicine* 64.2 (2010), pp. 319–26.

Ivanov D, A Gardumi, RA Haast, J Pfeuffer, BA Poser, and K Uludağ. ‘‘Comparison of 3 T and 7 T ASL techniques for concurrent functional perfusion and BOLD studies’’. In: *NeuroImage* 156 (2017), pp. 363–376.

Jackson JD. *Classical Electrodynamics*. Wiley, 1998.

Jezzard P and RS Balaban. ‘‘Correction for geometric distortion in echo planar images from B0 field variations’’. In: *Magnetic Resonance in Medicine* 34.1 (1995), pp. 65–73.

Jochimsen TH and M Von Mengershausen. ‘‘ODIN-object-oriented development interface for NMR.’’ In: *Journal of Magnetic Resonance* 170.1 (2004), pp. 67–78.

Jochimsen TH, A Schäfer, R Bammer, and ME Moseley. ‘‘Efficient simulation of magnetic resonance imaging with Bloch-Torrey equations using intra-voxel magnetization gradients.’’ In: *Journal of Magnetic Resonance* 180.1 (2006), pp. 29–38.

Jones DK, TR Knösche, and R Turner. ‘‘White matter integrity, fiber count, and other fallacies: The do’s and don’ts of diffusion MRI’’. In: *NeuroImage* 73 (2013), pp. 239–254.

Kaatze U. ‘‘The dielectric properties of water in its different states of interaction’’. In: *Journal of solution chemistry* 26.11 (1997), pp. 1049–1112.

Kaatze U, R Pottel, and M Schaefer. ‘‘Dielectric spectrum of dimethyl sulfoxide/water mixtures as a function of composition’’. In: *The Journal of Physical Chemistry* 93.14 (1989), pp. 5623–5627.

Kardoulaki EM, RRA Syms, and IR Young. ‘‘MRI for Noninvasive Thermometry’’. In: *eMagRes* 5 (2016), pp. 1203–1218.

Katscher U and P Börnert. ‘‘Parallel RF transmission in MRI’’. In: *NMR in Biomedicine* 19.3 (2006), pp. 393–400.

Katscher U, T Voigt, C Findeklee, P Vernickel, K Nehrke, and O Dössel. ‘‘Determination of electric conductivity and local SAR via B1 mapping.’’ In: *IEEE transactions on medical imaging* 28.9 (2009), pp. 1365–74.

Kaye EA, S Josan, A Lu, J Rosenberg, BL Daniel, and KB Pauly. ‘‘Consistency of signal intensity and T2* in frozen ex vivo heart muscle, kidney, and liver tissue’’. In: *Journal of Magnetic Resonance Imaging* 31.3 (2010), pp. 719–724.

Khalighi MM, BK Rutt, and AB Kerr. ‘‘Adiabatic RF pulse design for Bloch Siegert B1+ mapping’’. In: *Magnetic Resonance in Medicine* 70 (2013), pp. 829–835.

— ‘‘RF pulse optimization for Bloch-Siegert B +1 mapping.’’ In: *Magnetic Resonance in Medicine*. Vol. 68. 3. 2011, pp. 2842–2842.

Kickhefel A, C Rosenberg, CR Weiss, H Rempp, J Roland, F Schick, and N Hosten. ‘‘Clinical Evaluation of MR Temperature Monitoring of Laser-Induced Thermotherapy in Human Liver Using the Proton-Resonance-Frequency Method and Predictive Models of Cell Death’’. In: *Journal of Magnetic Resonance Imaging* 33 (2011), pp. 704–712.

Kickhefel A, C Weiss, J Roland, P Gross, F Schick, and R Salomir. ‘‘Correction of susceptibility-induced GRE phase shift for accurate PRFS thermometry proximal to cryoablation iceball’’. In: *Magnetic Resonance Materials in Physics, Biology and Medicine* 25.1 (2012), pp. 23–31.

Klose U. ‘‘Mapping of the radio frequency magnetic field with a MR snapshot FLASH technique’’. In: *Medical physics* 19.4 (1992), pp. 1099–104.

Krahmer F and R Ward. ‘‘Stable and robust sampling strategies for compressive imaging’’. In: *IEEE Transactions on Image Processing* 23.2 (2014), pp. 612–622.

Kremer F and A Schönhals. *Broadband Dielectric Spectroscopy*. Springer Berlin Heidelberg, 2003.

Kuroda K. ‘‘Non-invasive MR thermography using the water proton chemical shift’’. In: *International Journal of Hyperthermia* 21.6 (2005), pp. 547–60.

— ‘‘Temperature Monitoring Using Chemical Shift’’. In: *eMagRes* 5 (2007), pp. 1121–1130.

Kuroda K, Naoyuki Takei, RV Mulkern, K Oshio, T Nakai, T Okada, A Matsumura, K Yanaka, K Hynynen, and FA Jolesz. ‘‘Feasibility of Internally Referenced

Brain Temperature Imaging with a Metabolite Signal''. In: *Magnetic Resonance in Medical Sciences* 2.1 (2003), pp. 17–22.

Kuroda K, D Kokuryo, E Kumamoto, K Suzuki, Y Matsuoka, and B Keserci. ''Optimization of self-reference thermometry using complex field estimation.'' In: *Magnetic Resonance in Medicine* 56.4 (2006), pp. 835–43.

Kuroda K, T Iwabuchi, M Obara, M Honda, K Saito, and Y Imai. ''Temperature Dependence of Relaxation Times in Proton Components of Fatty Acids''. In: *Magnetic Resonance in Medical Sciences* 10.3 (2011), pp. 177–183.

Kuroda K, K Oshio, aH Chung, K Hynynen, and FA Jolesz. ''Temperature mapping using the water proton chemical shift: a chemical shift selective phase mapping method.'' In: *Magnetic Resonance in Medicine* 38.5 (1997), pp. 845–51.

Labadie C, S Hetzer, J Schulz, T Mildner, M Aubert-fr, and HE Möller. ''Center-Out Echo-Planar Spectroscopic Imaging with Correction of Gradient-Echo Phase and Time Shifts''. In: *Magnetic Resonance in Medicine* 70.1 (2013), pp. 16–24.

Lauterbur PC. ''Image formation by induced local interactions: examples employing nuclear magnetic resonance''. In: *Nature* 242 (1973), pp. 190–191.

Le Bihan D, J Delannoy, R Levin, and L Levin. ''Temperature mapping with MR imaging of molecular diffusion: application to hyperthermia.'' In: *Radiology* 171.3 (1989), pp. 853–857.

Levitt MH. *Spin Dynamics: Basics of Nuclear Magnetic Resonance*. Wiley, 2001.

Lewa CJ and JD de Certaines. ''Body Temperature Mapping by Magnetic Resonance Imaging''. In: *Spectroscopy Letters* 27.10 (1994), pp. 1369–1419.

Liu J, X Zhang, PF Van de Moortele, S Schmitter, and B He. ''Determining electrical properties based on B(1) fields measured in an MR scanner using a multi-channel transmit/receive coil: a general approach.'' In: *Physics in medicine and biology* 58.13 (2013), pp. 4395–408.

Lu Z, E Manias, DD Macdonald, and M Lanagan. ''Dielectric relaxation in dimethyl sulfoxide/water mixtures studied by microwave dielectric relaxation spectroscopy.'' In: *The journal of physical chemistry. A* 113.44 (2009), pp. 12207–14.

Lutz N, A Kuesel, and W Hull. ''A 1H-NMR Method for Determining Temperature in Cell Culture Perfusion Systems''. In: *Magnetic resonance in medicine* 29.1 (1993), pp. 113–118.

Magin RL, RP Liburdy, and B Persson. *Biological Effects and Safety Aspects of Nuclear Magnetic Resonance Imaging and Spectroscopy*. New York: New York Academy of Sciences, 1992, pp. 1–402.

Maier F, A Krafft, J Yung, RJ Stafford, AM Elliott, R Dillmann, W Semmler, and M Bock. ''Velocity navigator for motion compensated thermometry''. In: *Magnetic Resonance Materials in Physics, Biology and Medicine* 25.1 (2012), pp. 15–22.

Malik SJ, GD Kenny, and JV Hajnal. ''Slice profile correction for transmit sensitivity mapping using actual flip angle imaging''. In: *Magnetic Resonance in Medicine* 65.5 (2011), pp. 1393–1399.

Mansfield P. ''Multi-planar image formation using NMR spin echoes''. In: *Journal of Physics C: Solid State Physics* 10 (1977), pp. 55–58.

Marques JP and R Bowtell. ''Application of a Fourier-based method for rapid calculation of field inhomogeneity due to spatial variation of magnetic susceptibility''. In: *Concepts in Magnetic Resonance Part B: Magnetic Resonance Engineering* 25B.1 (2005), pp. 65–78.

McCall RP. *Physics of the Human Body*. Johns Hopkins University Press, 2010.

McDannold N. ''Quantitative MRI-based temperature mapping based on the proton resonant frequency shift: review of validation studies''. In: *International Journal of Hyperthermia* 21.6 (2005), pp. 533–546.

McDannold N, A Barnes, F Rybicki, K Oshio, Nk Chen, K Hynynen, and RV Mulkern. ''Temperature mapping considerations in the breast with line scan echo planar spectroscopic imaging''. In: *Magnetic Resonance in Medicine* 58 (2007), pp. 1117–1123.

McDannold N, C Tempany, F Jolesz, and K Hynynen. ''Evaluation of referenceless thermometry in MRI-guided focused ultrasound surgery of uterine fibroids''. In: *Journal of Magnetic Resonance Imaging* 28.4 (2008), pp. 1026–32.

Mcnaught AD and A Wilkinson. *IUPAC. Compendium of Chemical Terminology, 2nd ed. (the "Gold Book")*. Oxford: Blackwell Scientific Publications, 1997.

Meier B, S Greiser, J Haase, T Herrmannsdörfer, F Wolff-Fabris, and J Wosnitza. ''NMR signal averaging in 62 T pulsed fields''. In: *Journal of Magnetic Resonance* 210.1 (2011), pp. 1–6.

Metropolis N and A Rosenbluth. ''Equation of state calculations by fast computing machines''. In: *The Journal of Chemical Physics* 21.6 (1953), pp. 1087–1092.

Meyer CH, JM Pauly, A Macovski, and DG Nishimura. ''Simultaneous spatial and spectral selective excitation''. In: *Magnetic Resonance in Medicine* 15.2 (1990), pp. 287–304.

Mizuno K, S Imafuji, T Ochi, T Ohta, and S Maeda. ''Hydration of the CH Groups in Dimethyl Sulfoxide Probed by NMR and IR''. In: *The Journal of Physical Chemistry B* 104.47 (2000), pp. 11001–11005.

Morrell GR. ''A phase-sensitive method of flip angle mapping''. In: *Magnetic Resonance in Medicine* 60.4 (2008), pp. 889–894.

Müller DK, A Pampel, and HE Möller. ''Corrigendum to "Matrix-algebra-based calculations of the time evolution of the binary spin-bath model for magnetization transfer" [J. Magn. Reson. 230 (2013) 88–97]''. In: *Journal of Magnetic Resonance* 261 (2015), p. 221.

Müller DK, A Pampel, and HE Möller. ‘‘Matrix-algebra-based calculations of the time evolution of the binary spin-bath model for magnetization transfer.’’ In: *Journal of Magnetic Resonance* 230 (2013), pp. 88–97.

Napoli A, M Anzidei, F Ciolina, E Marotta, B Cavallo Marincola, G Brachetti, L Di Mare, G Cartocci, F Boni, V Noce, L Bertaccini, and C Catalano. ‘‘MR-guided high-intensity focused ultrasound: Current status of an emerging technology’’. In: *CardioVascular and Interventional Radiology* 36.5 (2013), pp. 1190–1203.

Nehrke K. ‘‘On the steady-state properties of actual flip angle imaging (AFI).’’ In: *Magnetic Resonance in Medicine* 61.1 (2009), pp. 84–92.

Nelson TR and SM Tung. ‘‘Temperature dependence of proton relaxation times in vitro’’. In: *Magnetic Resonance Imaging* 5.3 (1987), pp. 189–199.

Nemethy G and HA Scheraga. ‘‘Structure of Water and Hydrophobic Bonding in Proteins. I. A Model for the Thermodynamic Properties of Liquid Waters’’. In: *The Journal of Chemical Physics* 36.12 (1962), p. 3382.

Nörtemann K, J Hilland, and U Kaatze. ‘‘Dielectric properties of aqueous NaCl solutions at microwave frequencies’’. In: *The Journal of Physical Chemistry A* 101.37 (1997), pp. 6864–6869.

Odéen H, S Almquist, J de Bever, DA Christensen, and DL Parker. ‘‘MR thermometry for focused ultrasound monitoring utilizing model predictive filtering and ultrasound beam modeling’’. In: *Journal of therapeutic ultrasound* 4 (2016), p. 23.

Oh S, YC Ryu, G Carluccio, CT Sica, and CM Collins. ‘‘Measurement of SAR-induced temperature increase in a phantom and in vivo with comparison to numerical simulation’’. In: *Magnetic Resonance in Medicine* 71.5 (2014), pp. 1923–1931.

Pandeya GD, MJW Greuter, B Schmidt, T Flohr, and M Oudkerk. ‘‘Assessment of thermal sensitivity of CT during heating of liver: An ex vivo study’’. In: *British Journal of Radiology* 85.1017 (2012), pp. 661–665.

Park HW, DJ Kim, and ZH Cho. ‘‘Gradient Reversal Technique and Its Applications to Chemical-Shift-Related NMR Imaging’’. In: *Magnetic Resonance in Medicine* 4.6 (1987), pp. 526–536.

Parker DL. ‘‘Applications of NMR Imaging in Hyperthermia: An Evaluation of the Potential for Localized Tissue Heating and Noninvasive Temperature Monitoring’’. In: *IEEE Transactions on Biomedical Engineering* BME-31.1 (1984), pp. 161–167.

Parker D, V Smith, P Sheldon, L Crooks, and L Fussell. ‘‘Temperature distribution measurements in two-dimensional NMR imaging’’. In: *Medical physics* 10.3 (1983), pp. 321–325.

Patzig F. ‘‘The Spatial Precision of Echo-Planar Imaging: Investigations based on Analytical Point Spread Functions’’. PhD thesis. University Leipzig, 2016.

Pauling L. *The Nature of the Chemical Bond and the Structure of Molecules and Crystals: An Introduction to Modern Structural Chemistry*. Cornell University Press, 1960, p. 644.

Pauly JM, P Le Roux, and D Nishimura. ''Parameter relations for the Shinnar-Le Roux selective excitation pulse design algorithm''. In: *Medical Imaging, IEEE* (1991).

Peters NHGM, LW Bartels, SM Sprinkhuizen, KL Vincken, and CJG Bakker. ''Do respiration and cardiac motion induce magnetic field fluctuations in the breast and are there implications for MR thermometry?'' In: *Journal of Magnetic Resonance Imaging* 29.3 (2009), pp. 731–5.

Peters RD and RM Henkelman. ''Proton-resonance frequency shift MR thermometry is affected by changes in the electrical conductivity of tissue''. In: *Magnetic Resonance in Medicine* 43.1 (2000), pp. 62–71.

Petridou N, A Schäfer, PA Gowland, and R Bowtell. ''Phase vs. magnitude information in functional magnetic resonance imaging time series: toward understanding the noise.'' In: *Magnetic Resonance Imaging* 27.8 (2009), pp. 1046–57.

Pichardo S, M Köhler, J Lee, and K Hynnyen. ''In vivo optimisation study for multi-baseline MR-based thermometry in the context of hyperthermia using MR-guided high intensity focused ultrasound for head and neck applications.'' In: *International journal of hyperthermia* 30.8 (2014), pp. 579–92.

Pohmann R and K Scheffler. ''A theoretical and experimental comparison of different techniques for B1 mapping at very high fields''. In: *NMR in Biomedicine* 26.3 (2013), pp. 265–275.

Pople JA. ''The Theory of Chemical Shifts in Nuclear Magnetic Resonance. I. Induced Current Densities''. In: *Proceedings of the Royal Society A: Mathematical, Physical and Engineering Sciences* 239.1219 (1957), pp. 541–549.

— ''The Theory of Chemical Shifts in Nuclear Magnetic Resonance. II. Interpretation of Proton Shifts''. In: *Proceedings of the Royal Society A: Mathematical, Physical and Engineering Sciences* 239.1219 (1957), pp. 550–556.

Pruessmann KP, M Weiger, MB Scheidegger, and P Boesiger. ''SENSE: sensitivity encoding for fast MRI''. In: *Magnetic Resonance in Medicine* 42.5 (1999), pp. 952–62.

Quesson B, JA de Zwart, and CTW Moonen. ''Magnetic resonance temperature imaging for guidance of thermotherapy.'' In: *Journal of Magnetic Resonance Imaging* 12.4 (2000), pp. 525–33.

Raistrick ID, DR Franceschetti, and JR Macdonald. ''Theory''. In: *Impedance Spectroscopy Theory, Experiment, and Applications*. Wiley-Interscience, 2005. Chap. 2, pp. 27–128.

Raj D, D Paley, A Anderson, RP Kennan, and J Gore. ''A model for susceptibility artefacts from respiration in functional echo-planar magnetic resonance imaging''. In: *Physics in medicine and biology* 45 (2000), p. 3809.

Ramsey NF. ''Resonance transitions induced by perturbations at two or more different frequencies''. In: *Physical Review* 100.4 (1955), pp. 1191–1194.

Rastogi A, AK Ghosh, and SJ Suresh. ''Hydrogen bond interactions between water molecules in bulk liquid, near electrode surfaces and around ions''. In: *Thermodynamics - Physical Chemistry of Aqueous Systems*. 2011. Chap. 13, pp. 1–14.

Reeder SB, Z Wen, H Yu, AR Pineda, GE Gold, M Markl, and NJ Pelc. ''Multicoil Dixon chemical species separation with an iterative least-squares estimation method.'' In: *Magnetic Resonance in Medicine* 51.1 (2004), pp. 35–45.

Ren J, I Dimitrov, AD Sherry, and CR Malloy. ''Composition of adipose tissue and marrow fat in humans by 1H NMR at 7 Tesla''. In: *Journal of Lipid Research* 49.9 (2008), pp. 2055–62.

Rieke V and K Butts-Pauly. ''Echo combination to reduce proton resonance frequency (PRF) thermometry errors from fat''. In: *Journal of Magnetic Resonance Imaging* 27.3 (2008), pp. 673–7.

— ''MR Thermometry''. In: *Journal of Magnetic Resonance Imaging* 27.2 (2008), pp. 376–390.

Rieke V, R Instrella, J Rosenberg, W Grissom, B Werner, E Martin, and KB Pauly. ''Comparison of Temperature Processing Methods for Monitoring Focused Ultrasound Ablation in the Brain''. In: *Journal of Magnetic Resonance Imaging* 1471 (2013), pp. 1462–1471.

Rieke V, AM Kinsey, AB Ross, WH Nau, CJ Diederich, G Sommer, and K Butts-Pauly. ''Referenceless MR thermometry for monitoring thermal ablation in the prostate.'' In: *IEEE transactions on medical imaging* 26.6 (2007), pp. 813–21.

Rieke V, KK Vigen, G Sommer, BL Daniel, JM Pauly, and K Butts-Pauly. ''Referenceless PRF shift thermometry''. In: *Magnetic Resonance in Medicine* 51.6 (2004), pp. 1223–31.

Robinson S, G Grabner, S Witoszynskyj, and S Trattnig. ''Combining phase images from multi-channel RF coils using 3D phase offset maps derived from a dual-echo scan''. In: *Magnetic Resonance in Medicine* 65.6 (2011), pp. 1638–48.

Robitaille PML. ''Ultra High Field Magnetic Resonance Imaging: A Historical Perspective''. In: *Ultra High Field Magnetic Resonance Imaging*. Springer US, 2006, pp. 1–17.

Robitaille PML, aM Abduljalil, A Kangarlu, X Zhang, Y Yu, R Burgess, S Bair, P Noa, L Yang, H Zhu, B Palmer, Z Jiang, DM Chakeres, and D Spigos. ''Human

magnetic resonance imaging at 8 T''. In: *NMR in biomedicine* 11.6 (1998), pp. 263–5.

Roemer PPB, WWA Edelstein, CE Hayes, SP Souza, and OM Mueller. ''The NMR phased array''. In: *Magnetic Resonance in Medicine* 16.2 (1990), pp. 192–225.

Saccomandi P, E Schena, and S Silvestri. ''Techniques for temperature monitoring during laser-induced thermotherapy: An overview''. In: *International Journal of Hyperthermia* 29.7 (2013), pp. 609–619.

Sacolick LI, F Wiesinger, I Hancu, and MW Vogel. ''B1 mapping by Bloch-Siegert shift.'' In: *Magnetic Resonance in Medicine* 63.5 (2010), pp. 1315–22.

Sacolick LI, L Sun, MW Vogel, WT Dixon, and I Hancu. ''Fast radiofrequency flip angle calibration by Bloch-Siegert shift.'' In: *Magnetic Resonance in Medicine* 66.5 (2011), pp. 1333–8.

Salomir R, M Viallon, A Kickhefel, J Roland, DR Morel, L Petrusca, V Auboiroux, T Goget, S Terraz, CD Becker, and P Gross. ''Reference-free PRFS MR-thermometry using near-harmonic 2-D reconstruction of the background phase''. In: *IEEE Transactions on Medical Imaging* 31.2 (2012), pp. 287–301.

Schäfer A, S Wharton, PA Gowland, and R Bowtell. ''Using magnetic field simulation to study susceptibility-related phase contrast in gradient echo MRI.'' In: *NeuroImage* 48.1 (2009), pp. 126–37.

Schenck JF. ''The role of magnetic susceptibility in magnetic resonance imaging: MRI magnetic compatibility of the first and second kinds.'' In: *Medical physics* 23.6 (1996), pp. 815–50.

Schick F, J Forster, J Machann, P Huppert, and CD Claussen. ''Highly selective water and fat imaging applying multislice sequences without sensitivity to B1 field inhomogeneities''. In: *Magnetic Resonance in Medicine* 38.2 (1997), pp. 269–274.

Schmitt F, MMK Stehling, and R Turner, eds. *Echo-Planar Imaging: Theory, Technique and Application*. Springer-Verlag GmbH, 1998, p. 662.

Schneider WG, HJ Bernstein, and JA Pople. ''Proton Magnetic Resonance Chemical Shift of Free (Gaseous) and Associated (Liquid) Hydride Molecules''. In: *Journal of Chemical Physics* 28.4 (1958), p. 601.

Seifert F, G Wübbeler, S Junge, B Ittermann, and H Rinneberg. ''Patient safety concept for multichannel transmit coils''. In: *Journal of Magnetic Resonance Imaging* 26.5 (2007), pp. 1315–21.

Shellock FG. ''Radiofrequency energy-induced heating during MR procedures: a review.'' In: *Journal of Magnetic Resonance Imaging* 12.1 (2000), pp. 30–6.

Shinnar M, S Eleff, H Subramanian, and JS Leigh. ''The synthesis of pulse sequences yielding arbitrary magnetization vectors''. In: *Magnetic Resonance in Medicine* 12.1 (1989), pp. 74–80.

Shmatukha AV, PR Harvey, and CJG Bakker. ‘‘Correction of proton resonance frequency shift temperature maps for magnetic field disturbances using fat signal.’’ In: *Journal of Magnetic Resonance Imaging* 25.3 (2007), pp. 579–87.

Simonis FFJ, AJE Raaijmakers, JJW Lagendijk, and CAT van den Berg. ‘‘Validating subject-specific RF and thermal simulations in the calf muscle using MR-based temperature measurements’’. In: *Magnetic Resonance in Medicine* 77.4 (2017), pp. 1691–1700.

Simonis FFJ, ET Petersen, JJW Lagendijk, and CAT Van Den Berg. ‘‘Feasibility of measuring thermoregulation during RF heating of the human calf muscle using MR based methods’’. In: *Magnetic Resonance in Medicine* 75.4 (2016), pp. 1743–1751.

Simpson JH and HY Carr. ‘‘Diffusion and Nuclear Spin Relaxation in Water’’. In: *Physical Review* 111.5 (1958), pp. 1201–1202.

Soher BJ, C Wyatt, SB Reeder, and JR MacFall. ‘‘Noninvasive temperature mapping with MRI using chemical shift water-fat separation.’’ In: *Magnetic Resonance in Medicine* 63.5 (2010), pp. 1238–46.

Speck O, J Stadler, and M Zaitsev. ‘‘High resolution single-shot EPI at 7T’’. In: *Magnetic Resonance Materials in Physics, Biology and Medicine* 21.1-2 (2008), pp. 73–86.

Sprinkhuizen SM and CJG Bakker. ‘‘Temperature dependence of the magnetic volume susceptibility of human breast fat tissue: an NMR study’’. In: *Magnetic Resonance Materials in Physics, Biology and Medicine* 25.1 (2012), pp. 33–39.

Sprinkhuizen SM, CJG Bakker, and LW Bartels. ‘‘Absolute MR thermometry using time-domain analysis of multi-gradient-echo magnitude images’’. In: *Magnetic Resonance in Medicine* 64.1 (2010), pp. 239–248.

Sprinkhuizen SM, MK Konings, MJ Van der Bom, MA Viergever, CJG Bakker, and LW Bartels. ‘‘Temperature-induced tissue susceptibility changes lead to significant temperature errors in PRFS-based MR thermometry during thermal interventions.’’ In: *Magnetic Resonance in Medicine* 64.5 (2010), pp. 1360–72.

Stehling MK, R Turner, and P Mansfield. ‘‘Echo-planar imaging: magnetic resonance imaging in a fraction of a second’’. In: *Science* 254.5028 (1991), pp. 43–50.

Stillinger FH. ‘‘Water revisited.’’ In: *Science* 209.4455 (1980), pp. 451–457.

Stollberger R and P Wach. ‘‘Imaging of the active B1 field in vivo’’. In: *Magnetic resonance in medicine* 35.2 (1996), pp. 246–251.

Streicher MN, A Schäfer, E Reimer, B Dhital, R Trampel, D Ivanov, and R Turner. ‘‘Effects of air susceptibility on proton resonance frequency MR thermometry.’’ In: *Magnetic Resonance Materials in Physics, Biology and Medicine* 25.1 (2012), pp. 41–47.

Streicher MN, A Schäfer, D Ivanov, DK Müller, A Amadon, E Reimer, L Huber, B Dhital, D Rivera, C Kögler, R Trampel, A Pampel, and R Turner. ''Fast accurate MR thermometry using phase referenced asymmetric spin-echo EPI at high field''. In: *Magnetic Resonance in Medicine* 71.2 (2014), pp. 524–533.

Tang L and TS Ibrahim. ''On the Radio-Frequency Power Requirements of Human MRI''. In: *PIERS Online* 3.6 (2007), pp. 886–889.

Taylor Ba, KP Hwang, JD Hazle, and RJ Stafford. ''Autoregressive moving average modeling for spectral parameter estimation from a multigradient echo chemical shift acquisition''. In: *Medical Physics* 36.3 (2009), p. 753.

Taylor Ba, KP Hwang, AM Elliott, A Shetty, JD Hazle, and RJ Stafford. ''Dynamic chemical shift imaging for image-guided thermal therapy: Analysis of feasibility and potential''. In: *Medical Physics* 35.2 (2008), p. 793.

Tempany C, NJ McDannold, K Hynynen, and FA Jolesz. ''Focused ultrasound surgery in oncology: overview and principles''. In: *Radiology* 259.1 (2011), p. 39.

Todd N, M Diakite, A Payne, and DL Parker. ''Hybrid Proton Resonance Frequency/T1 Technique for Simultaneous Temperature Monitoring in Adipose and Aqueous Tissues''. In: *Magnetic Resonance in Medicine* 69.1 (2013), pp. 62–70.

— ''In vivo evaluation of multi-echo hybrid PRF/T1 approach for temperature monitoring during breast MR-guided focused ultrasound surgery treatments''. In: *Magnetic Resonance in Medicine* 72.3 (2014), pp. 793–799.

Traficante DD. ''Relaxation Can T2 Be Longer Than T1?'' In: *Concepts in Magnetic Resonance* 3 (1991), pp. 171–177.

Turner R. ''Gradient coil design: A review of methods''. In: *Magnetic Resonance Imaging* 11.7 (1993), pp. 903–920.

Turner R and MN Streicher. ''Measuring temperature using MRI: a powerful and versatile technique''. In: *Magnetic Resonance Materials in Physics, Biology and Medicine* 25 (2012), pp. 11–13.

Turner R, D Le Bihan, J Maier, R Vavrek, L Hedges, J Pekar, and Others. ''Echo-planar imaging of intravoxel incoherent motion''. In: *Radiology* 177.2 (1990), p. 407.

Turner R, P Jezzard, H Wen, KK Kwong, D Le Bihan, T Zeffiro, and RS Balaban. ''Functional mapping of the human visual cortex at 4 and 1.5 tesla using deoxygenation contrast EPI.'' In: *Magnetic Resonance in Medicine* 29.2 (1993), pp. 277–9.

Uecker M, S Zhang, D Voit, A Karaus, KD Merboldt, and J Frahm. ''Real-time MRI at a resolution of 20 ms''. In: *NMR in Biomedicine* 23.8 (2010), pp. 986–994.

Uludağ K, B Müller-Bierl, and K Uğurbil. ''An integrative model for neuronal activity-induced signal changes for gradient and spin echo functional imaging.'' In: *NeuroImage* 48.1 (2009), pp. 150–65.

Van de Moortele PF, C Akgun, G Adriany, S Moeller, J Ritter, CM Collins, MB Smith, JT Vaughan, and K Uğurbil. ''B(1) destructive interferences and spatial phase patterns at 7 T with a head transceiver array coil.'' In: *Magnetic Resonance in Medicine* 54.6 (2005), pp. 1503–18.

van Gelderen P, JA de Zwart, P Starewicz, RS Hinks, and JH Duyn. ''Real-time shimming to compensate for respiration-induced B0 fluctuations''. In: *Magnetic Resonance in Medicine* 57.2 (2007), pp. 362–8.

van Lier A, ANT Kotte, BW Raaymakers, JJW Lagendijk, and CAT Van den Berg. ''Radiofrequency heating induced by 7T head MRI: thermal assessment using discrete vasculature or Pennes' bioheat equation.'' In: *Journal of Magnetic Resonance Imaging* 35.4 (2012), pp. 795–803.

Vaughan JT. ''Ultra High Field MRI: High Frequency Coils''. In: *Ultra High Field Magnetic Resonance Imaging*. Vol. c. Springer US, 2006. Chap. 6, pp. 127–161.

Vaughan JT, M Garwood, CM Collins, W Liu, L Delabarre, G Adriany, P Andersen, H Merkle, R Goebel, M Smith, and Others. ''7T vs. 4T: RF power, homogeneity, and signal-to-noise comparison in head images''. In: *Magnetic resonance in medicine* 46.1 (2001), pp. 24–30.

Vesanen PT, KCJ Zevenhoven, JO Nieminen, J Dabek, LT Parkkonen, and RJ Ilmoniemi. ''Temperature dependence of relaxation times and temperature mapping in ultra-low-field MRI.'' In: *Journal of Magnetic Resonance* 235 (2013), pp. 50–7.

Vigen KK, BL Daniel, JM Pauly, and K Butts. ''Triggered, Navigated, Multi-Baseline Method for Proton Resonance Frequency Temperature Mapping With Respiratory Motion''. In: *Magnetic Resonance in Medicine* 50.5 (2003), pp. 1003–1010.

Volk A, B Tiffon, J Mispelter, and JM Lhoste. ''Chemical shift-specific slice selection. A new method for chemical shift imaging at high magnetic field''. In: *Journal of magnetic resonance* 71.1 (1987), pp. 168–174.

Volz S, U Nöth, A Rotarska-Jagiela, and R Deichmann. ''A fast B1-mapping method for the correction and normalization of magnetization transfer ratio maps at 3 T''. In: *Neuroimage* 49.4 (2010), pp. 3015–3026.

Witoszynskyj S, A Rauscher, JR Reichenbach, and M Barth. ''Phase unwrapping of MR images using Phi UN--a fast and robust region growing algorithm.'' In: *Medical image analysis* 13.2 (2009), pp. 257–68.

Wyatt C, BJ Soher, K Arunachalam, and J Macfall. ''Comprehensive analysis of the Cramer-Rao bounds for magnetic resonance temperature change measurement in fat-water voxels using multi-echo imaging.'' In: *Magnetic Resonance Materials In Physics Biology And Medicine* (2011).

Yacoub E, TQ Duong, PF Van De Moortele, M Lindquist, G Adriany, SG Kim, K Uğurbil, and X Hu. ''Spin-echo fMRI in humans using high spatial resolutions

and high magnetic fields.'' In: *Magnetic Resonance in Medicine* 49.4 (2003), pp. 655–64.

Yarnykh VL. ''Actual Flip-Angle Imaging in the Pulsed Steady State: A Method for Rapid Three-Dimensional Mapping of the Transmitted Radiofrequency Field''. In: *Magnetic Resonance in Medicine* 57.1 (2007), pp. 192–200.

— ''Optimal radiofrequency and gradient spoiling for improved accuracy of T1 and B1 measurements using fast steady-state techniques.'' In: *Magnetic Resonance in Medicine* 63.6 (2010), pp. 1610–26.

Yoo TS, MJ Ackerman, WE Lorensen, W Schroeder, V Chalana, S Aylward, D Metaxas, and R Whitaker. ''Engineering and algorithm design for an image processing Api: a technical report on ITK--the Insight Toolkit.'' In: *Studies in health technology and informatics* 85 (2002), pp. 586–92.

Yuan J, CS Mei, LP Panych, NJ McDannold, and B Madore. ''Towards fast and accurate temperature mapping with proton resonance frequency-based MR thermometry''. In: *Quantitative imaging in medicine and surgery* 2.1 (2012), pp. 21–32.

Yung JP, D Fuentes, CJ MacLellan, F Maier, Y Liapis, JD Hazle, and RJ Stafford. ''Referenceless Magnetic Resonance Temperature Imaging using Gaussian Process Modeling''. In: *Medical Physics* (2017).

Zur Y, ML Wood, and LJ Neuringer. ''Spoiling of Transverse Magnetization in Steady-State Sequences''. In: *Magnetic Resonance in Medicine* 21.2 (1991), pp. 251–263.

Appendix

Acknowledgement

This accomplishment would not have been possible without the support of many people. Throughout my life I have been surrounded by many people, that inspired, promoted and helped me more than I could ever expect.

I express my deepest gratitude to my Doktorvater Robert Turner for his interest, time and support throughout. I am very thankful to Andreas Schäfer for his guidance, assistance and lots of time. A warm thank-you goes to Josef Käs for never hesitating to help. I also want to thank Christoph Leuze for his friendship from the beginning of our physics studies in Leipzig. Christoph drew my attention to the fine Neurophysics group and the exceptional environment at the Max Planck Institute and got me to apply for a PhD position. At the MPI, I had the opportunity to work in the amazing field of MRI, which in my opinion, is a perfect mix of impressive engineering, medicine and basic to advanced physics.

I want to thank many people at the Max Planck Institute and especially in the Neurophysics department: The whole NMR group, particularly Harald Möller, Andre Pampel, Christian Labadie, Dirk Müller - for their openness, interest, insight and willingness to help and collaborate. My roommates Eugenia, Bibek and Dimo for such a productive and cool time in and outside the office and for still keeping in touch. Enrico for being the most helpful IT-guy I ever met. Aline, Nicole and Christine, Domenica, Elisabeth, Heike and Astrid for doing such a good and affectionate job. Debra, Carsten K. and S., Cornelius, Steffen and Marcel for the good collaboration. The helium refilling team with Renzo, Robert and Andreas. My friends Dimo and Renzo for helping and checking the thesis.

I would like to thank my friends Miri and Doychin, my Coaches Roland, Jeffries, Garcia and Sven, my English teacher and friend Jeremy for so many things. Finally, I would like to thank my family in Oberschwaben, Las Vegas and Sachsen for always being there for me.

Articles during this PhD project

1. Ivanov, D., Schäfer, A., **Streicher, M.N.**, Heidemann, R.M., Trampel, R., Turner, R. (2010). A simple low-SAR technique for chemical-shift selection with high-field spin-echo imaging. *Magnetic Resonance in Medicine*, 64(2):319-326.

2. Turner, R., **Streicher, M.N.** (2012). Measuring temperature using MRI: A powerful and versatile technique. *Magnetic Resonance Materials in Physics, Biology and Medicine*, 25(1):11-13.

3. **Streicher, M.N.**, Schäfer, A., Reimer, E., Dhital, B., Trampel, R., Ivanov, D., Turner, R. (2012). Effects of air susceptibility on proton resonance frequency MR thermometry. *Magnetic Resonance Materials in Physics, Biology and Medicine*, 25(1):41-47.

4. Krieger S.N., **Streicher M.N.**, Trampel R., Turner R. (2012). Cerebral Blood Volume Changes During Brain Activation. *Journal of Cerebral Blood Flow and Metabolism*, 32(8):1618-1631.

5. **Streicher, M.N.**, Schäfer, A., Ivanov, D., Müller, D. K., Amadon, A., Reimer, E., Huber, L., Dhital, B., Rivera, D., Kögler, C., Trampel, R., Pampel, A., and Turner, R. (2014). Fast accurate MR thermometry using phase referenced asymmetric spin-echo EPI at high field. *Magnetic Resonance in Medicine*, 71(2):524-533.

6. Stüber, C., Morawski, M., Schäfer, A., Labadie, C., Wähnert, M., Leuze, C., **Streicher, M.N.**, Barapatre, N., Reimann, K., Geyer, S., Spemann, D., Turner, R. (2014). Myelin and iron concentration in the human brain: A quantitative study of MRI contrast. *NeuroImage*, 93(1):95-106

7. Huber, L., Ivanov, D., Krieger, S. N., **Streicher, M.N.**, Mildner, T., Poser, B.A., Möller, H. E., and Turner, R. (2014). Slab-selective, BOLD-corrected VASO at 7 tesla provides measures of cerebral blood volume reactivity with high signal-to-noise ratio. *Magnetic Resonance in Medicine*, 72(1):137-148.

8. Waehnert, M.D., Dinse, J., Weiss, M., **Streicher, M.N.**, Waehnert, P., Geyer, S., Turner, R., Bazin, P.L. (2014). Anatomically motivated modeling of cortical laminae. *NeuroImage*, 93(2):210-220.

Conference talks during this PhD project

1. **Streicher, M.N.**, Schäfer, A., Turner, R. (2009). Effects of air susceptibility on MR thermometry. *Proceedings of the 26th Annual Meeting of ESMRMB, Antalya, Turkey.*

2. **Streicher, M.N.**, Ivanov, D., Müller, D., Pampel, A., Schäfer, A., Turner, R. (2010). Chemically selective spin-echo EPI for fat saturation and MR Thermometry. *German-Chinese Workshop on High Field MRI, Magdeburg, Germany.*

3. **Streicher, M.N.**, Schäfer, A., Müller, D., Kögler, C., Reimer, E., Dhital, B., Trampel R., Rivera, D., Pampel, A., Ivanov, D., Turner, R. (2011). Frequency-selective asymmetric spin-echo EPI with parallel imaging for fast internally referenced MR thermometry. *Proceedings of the 19th Annual Meeting of ISMRM, Montreal, Canada.*

4. Huber, L., Ivanov, D., **Streicher, M.N.**, and Turner, R. (2012). Slab-selective, BOLD-corrected VASO (SS-VASO) in human brain at 7 T. *Proceedings of the ISMRM Brain Function Workshop, Whistler, Canada.*

Conference posters during this PhD project

1. **Streicher, M.N.**, Schäfer, A., Turner, R. (2008). MR Phase-Based Thermometry. *Poster presented at What's Special about 7T+?, Rome, Italy.*

2. Ivanov, D., Schäfer, A., **Streicher, M.N.**, Trampel, R., Turner, R. (2009). Fat suppression with low SAR for SE EPI fMRI at 7T. *Proceedings of the 17th Annual Meeting of ISMRM, Honolulu, HI, USA.*

3. Ivanov, D., **Streicher, M.N.**, Schäfer, A., Turner, R. (2010). Comparison of fat suppression methods for functional and diffusion studies using SE EPI at 7T. *1st Annual Scientific Symposium, Berlin, Germany.*

4. **Streicher, M.N.**, Schäfer, A., Ivanov, D., Turner, R. (2010). Air susceptibility effects on proton resonance frequency temperature mapping. *Proceedings of the 18th Annual Meeting of ISMRM, Stockholm, Sweden.*

5. **Streicher, M.N.**, Schäfer, A., Dhital, B., Müller, D., Heidemann, R. M., Pampel, A., Ivanov, D., Turner, R. (2010). Chemically Selective Asymmetric Spin-Echo EPI Phase Imaging for Internally Referenced MR Thermometry. *Proceedings of the 18th Annual Meeting of ISMRM, Stockholm, Sweden.*

6. Krieger, S., **Streicher, M.N.**, Trampel, R., Turner, R. (2011). Physiological and haemodynamical analysis of cerebral blood volume changes during brain

activation. *Proceedings of the 17th Annual Meeting of the OHBM, Quebec, Canada.*

7. Krieger, S., Trampel, R., **Streicher, M.N.**, Turner, R. (2012). Cerebral blood volume changes during brain activation. *Proceedings of the 20th Annual Meeting of ISMRM, Melbourne, Australia.*

8. **Streicher, M.N.**, Schäfer, A., Ivanov, D., Huber, L., Dhital, B., Rivera, D., Kögler, C., Trampel, R., Pampel, A., Turner, R. (2012). Fast accurate MR thermometry using phase referenced asymmetric spin-echo EPI at high field. *Proceedings of the 20th Annual Meeting of ISMRM, Melbourne, Australia.*

9. Ivanov, D., Huber, L., Kabisch, S., **Streicher, M.N.**, Schloegl, H., Henseler, I., Roggenhofer, E., Heinke, W., Turner, R. (2012). Mapping of CMRO2 changes in visual cortex during a visual motion paradigm at 7 T. *Proceedings of the 20th Annual Meeting of ISMRM, Melbourne, Australia.*

10. Wähnert, M., Weiss, M., **Streicher, M.N.**., Bazin, P.-L., Geyer, S., Turner, R. (2012). Do cortical layers conform to the Laplace equation?. *Proceedings of the 18th Annual Meeting of the OHBM, Beijing, China.*

11. Rivera, D., Siegert, T., Kögler, C., Schäfer, A., **Streicher, M.N.**, Turner, R. (2013). Transmit array with novel shield & fabrication technique for reducing losses at UHF. *Proceedings of the 21th Annual Meeting of ISMRM, Salt Lake City, UT, USA.*

12. Wähnert, M., Dinse, J., Weiss, M., **Streicher, M.N.**, Wähnert, P., Geyer, S., Turner, R., Bazin, P.-L. (2013). Realistic modeling of cortical laminae. *Proceedings of the 19th Annual Meeting of the OHBM, Seattle, WA, USA.*